New Development of Theoretical and Computational Methods for Probing Strong-Field Multiphoton Processes

By

Sang-Kil Son

M.S. in Physical Chemistry, KAIST, 1999
B.S. in Chemistry, KAIST, 1997

Submitted to the Department of Chemistry and the
Faculty of the Graduate School of the University of Kansas
in partial fulfillment of the requirements for the degree of

Doctor of Philosophy

Committee members

Shih-I Chu, Chair

Thomas E. Cravens

Siyuan Han

Peter M. Hierl

Weizhang Huang

Krzysztof Kuczera

Date defended: November 10, 2009

The Dissertation Committee for Sang-Kil Son certifies
that this is the approved version of the following dissertation:

New Development of Theoretical and Computational Methods for Probing Strong-Field Multiphoton Processes

Committee:

Shih-I Chu, Chair

Thomas E. Cravens

Siyuan Han

Peter M. Hierl

Weizhang Huang

Krzysztof Kuczera

Date approved: November 10, 2009

Contents

List of Figures

List of Tables

Abstract

The study of the strong-field multiphoton processes is a subject of much current significance in physics and chemistry. Recent progress of laser technology has triggered a burst of attosecond science where the electron dynamics plays a vital role in underlying physics. The nonlinear strong-field phenomena, such as multiphoton ionization, multiphoton resonance, high-order harmonic generation, etc, are beyond the perturbative regime and demand novel theoretical approaches for better understanding. This dissertation aims at developing new theoretical and computational methods with innovative spatial and temporal treatments, and delivering comprehensive studies of strong-field multiphoton processes explored by the proposed methods.

The time-dependent Voronoi-cell finite difference method is a new grid-based method for electronic structure and dynamics calculations of polyatomic molecules. The spatial part is accurately treated by the Voronoi-cell finite difference method on multicenter molecular grids, featuring high adaptivity and simplicity. The temporal part is solved by the split-operator time propagation technique, allowing accurate and efficient non-perturbative treatment of electronic dynamics in strong fields. The method is applied to self-interaction-free time-dependent density-functional calculations to probe multiphoton pro-

cesses of polyatomic molecules in intense ultrashort laser fields with arbitrary field–molecule orientation, highlighting the importance of multielectron effects.

The generalized Floquet theory is extended for the investigations of an atom in intense frequency-comb laser fields and a qubit system driven by intense oscillating fields. For the frequency-comb laser generated by a temporal train of pulses, the many-mode Floquet theory is extended to treat the interaction of an atom and a series of comb frequencies, demonstrating coherent control of simultaneous multiphoton resonance processes. For the strongly driven qubit, the Floquet theory is extended and its analytic solution is derived to explore multiphoton quantum interference in the superconducting flux qubit.

Acknowledgments

First of all, I would like to express my sincere gratitude to my advisor, Prof. Shih-I Chu, for giving me the opportunity to work with him and for his constant support, encouragement, guidance, and inspiration. His enthusiasm for science and beyond will be always in my memory. To me, he is not only a role model as the great scholar but also the great mentor in many aspects.

Also I would like to thank my committee members, Prof. Thomas Cravens, Prof. Siyuan Han, Prof. Peter Hierl, Prof. Weizhang Huang, and Prof. Krzysztof Kuczera for their suggestions and thoughtful review on this work.

My special thanks go to Dr. N. Sukumar for his kind assistance about the Voronoi-cell finite difference method, Prof. Siyuan Han for invaluable discussions about the Floquet-qubit project, and Dr. Domagoj Pavičić and Dr. Wen Li for allowance to use their experimental data with useful discussions.

I am grateful to all Prof. Chu's former and current group members. Especially I am indebted to Dr. Dmitry Telnov, aka Dima, and Dr. Zhongyuan Zhou for insightful explanations and fruitful discussions. It is my pleasure to thank Dr. Juan Carrera and Dr. John Heslar for making close friendship. Also I am thankful to Xiaoning Li and Jing Guo as good colleagues. I greatly appreciate all supports from Chemistry Department at University of Kansas. I wish to

thank all group members I have met at National Taiwan University. Although it was a short visit, I never forget the warm and friendly atmosphere from them.

With all my respects, I would like to thank my parents for their endless support and love. With all my hearts, I wish to thank my wife, Huijong, and my dear daughter, Hanna, for sharing love with me and discovering the happiness in my life.

Chapter 1

Introduction

The light–matter interaction is one of fundamentals in physics and chemistry. Light (i.e., the electromagnetic field) is a versatile tool to initiate, probe, and control physical and chemical processes. When the field strength is strong enough to ionize atoms and molecules, a number of novel strong-field phenomena [1, 2] come into view enlarging our insights in atomic, molecular, and chemical physics, and the electronic dynamics is a key ingredient to understand their underlying physics. The emergence of laser in science and technology opened new ways to study rich physics of the strong-field–atom and strong-field–molecule interactions. At the same time, the frequency-comb laser [3], which consists of a series of spectral lines, has revolutionarily impacted on high-precision spectroscopy and ultrafast science. The strong-field–atom interaction is ubiquitous in science. For example, strong-field multiphoton dynamics in artificial atoms can manipulate the qubit states for quantum computing [4].

The state-of-the-art advances of laser techniques lead to a birth of attosecond science [5, 6, 7]. In the attosecond (=10^{-18} sec.) timescale, we are able to achieve real-time observation and steering of the motion of electrons in atoms, molecules, and materials [7, 8], which might be one of ultimate goals most scien-

tists have dreamed of. Recent progresses of attosecond physics include attosecond pulse generation [9, 10, 11, 12], attosecond time-resolved spectroscopy [13], control of electron wave packets [14, 15, 16], probing of nuclear dynamics [17, 18] and electronic dynamics [19, 20], laser-induced electron diffraction [21, 22], lightwave electronics [23], electronic dynamics in chemical and biological phenomena [24], tomographic imaging of molecular orbitals [25, 26], and so on. Also exploration of the attosecond electronic dynamics in the strong-field regime, which cannot be examined in other ways, has attracted much interest theoretically and experimentally [27].

In this dissertation, we focus on theoretical exploration of the strong-field multiphoton processes with novel theoretical and computational approaches in space and time. The scope of the dissertation ranges from artificial atoms to polyatomic molecules, and from a continuous wave to the frequency-comb laser and ultrashort pulsed laser. We develop a new time-dependent Voronoi-cell finite difference method based on highly adaptive spatial discretization designed for polyatomic molecules. Also we extend the generalized Floquet formalism [28] for exact temporal treatments to study the interaction of quantum systems with frequency-comb laser fields and to analyze the strongly driven qubit system.

When the field strength is comparable to or exceeds to the Coulomb field experienced by outer-shell electrons in atoms, it is called a strong field[1], corresponding to the intensity of around 10^{15} W/cm^2 [2]. To help us imagine how strong it is, let us consider all energies from the Sun into the Earth as

[1]Note that some authors distinguish between "strong" and "super-strong", as the latter is equally called "intense" [29]. In this dissertation, however, we shall use both "strong" and "intense" as the same meaning, covering the intermediate regime (10^{13}–10^{15} W/cm^2) and strong-field regime (10^{15}–10^{18} W/cm^2) according to Ref. [2]

follows. Total solar insolation received at the Earth's surface is about 1.75×10^{17} Watts [30]. If all solar energies on the Earth's surface are concentrated into only 5×5 inches^2, then its intensity becomes about 1.1×10^{15} W/cm^2, which is corresponding to the intensity of the strong laser field used in laboratory. In this dissertation, we shall cover the laser intensities from 5×10^{13} W/cm^2 to 2.5×10^{15} W/cm^2.

There are many of nonlinear optical phenomena in the strong-field regime, such as multiphoton excitation (MPE) [31], ionization (MPI) [32], and dissociation (MPD) [33], above-threshold ionization (ATI) [34, 35] and dissociation (ATD) [36, 37], multiple high-order harmonic generation (HHG) [38, 39, 40, 41], Coulomb explosion (CE) [42, 43], chemical bond softening and hardening [44], coherent control of chemical and physical processes [45, 46], etc. These novel processes are far from satisfactory when described by the traditional perturbative approaches. For a theoretical aspect, it demands a non-perturbative treatment to understand these strong-field phenomena.

To capture electronic structure and dynamics inside the strong-field processes, one needs to solve the non-relativistic time-dependent Schrödinger equation (TDSE) including the light–matter interaction [47],

$$i\hbar \frac{\partial}{\partial t} \Psi(\mathbf{R}, t) = H(\mathbf{R}, t) \Psi(\mathbf{R}, t).$$

In fact, the whole of this dissertation is devoted to describe how to solve TDSE and what to do with TDSE solutions. Theoretical and computational challenges to solve TDSE for the molecular strong-field processes are categorized [48] as follows: i) many-electron quantum system, ii) spatial treatment for polyatomic molecules, and iii) temporal treatment in the non-perturbative way.

To address the first issue, we employ density-functional theory (DFT) and time-dependent density-functional theory (TDDFT) [49], which transforms an N-particle problem into an one-particle problem including all multielectron effects through the exchange and correlation functionals. It is worthwhile to note that conventional DFT methods are not applicable for accurate electronic structures and time-dependent problems due to spurious self-interaction energy and improper asymptotic behavior of the long-range potential. Therefore we implement self-interaction-free DFT and TDDFT with the proper long-range potential for electronic structure and dynamics calculations of polyatomic molecules.

Even for the one-electron problem in the 3-dimensional (3D) space, it is not trivial to obtain an accurate numerical solution because of the notorious Coulomb singularity between an electron and nuclei. To advance the spatial treatment for the Coulomb potential in 3D, Professor Chu's group has pioneered the generalized pseudospectral (GPS) method and time-dependent pseudospectral (TDGPS) method on optimal nonuniform grids for atoms and diatomic molecules [41, 50]. To answer the second issue of the spatial treatment for polyatomic molecules, we develop the Voronoi-cell finite difference (VFD) method with the help of geometrical adaptivity of the Voronoi diagram. The VFD method offers very simple numerical expressions on very complicated spatial problems. The spatial part of TDSE for polyatomic molecules is accurately solved by VFD on highly adaptive multicenter molecular grids. This VFD method combined with self-interaction-free DFT formula attains accurate electronic structure calculations for polyatomic molecules.

Regarding the third issue, there are two approaches to treat the temporal part of TDSE in the non-perturbative way. The first one is the time propagation method where the time-dependent wavefunction is directly propagated

under time-dependent Hamiltonian including the light–matter interaction and time-dependent multielectron responses of the wavefunctions (through TDDFT formula). We integrate the VFD method and the split-operator time propagation technique into the time-dependent Voronoi-cell finite difference (TDVFD) method. By means of TDVFD, we can perform TDDFT calculations for probing strong-field multiphoton processes in many-electron polyatomic molecules for the first time. Since a full 3D calculation for polyatomic molecules has been formidable within traditional numerical methods, most of strong-field studies have been based on a simple model. On the contrary, the proposed method allows for detailed studies of attosecond electronic dynamics including multielectron responses. We explore strong-field phenomena such as multiphoton ionization (MPI), photoelectron angular distribution (PAD), and high-order harmonic generation (HHG) for small polyatomic molecules, emphasizing multielectron responses in multiple orbital dynamics.

The second approach for the temporal treatment is to transform the time-dependent problem into a time-independent problem in the framework of the generalized Floquet formalism [28]. In this approach, we can obtain an exact solution of the time-dependent problem with an illuminating physical picture. The generalized Floquet theory is extended to two physical problems of much current interests: the frequency-comb laser, which consists of a series of equal-spacing frequencies, and the qubit (quantum bit), which is a unit of quantum information. To handle a train of pulses generating the comb structure in the frequency domain, we extend the many-mode Floquet theory for the interaction of an artificial two-level system with a series of comb frequencies and discuss coherent control of simultaneous multiphoton resonance processes and HHG enhancement by tuning the carrier-envelope phase shift. We also extend

the Floquet theory for the exploration of multiphoton quantum interference in a superconducting flux qubit driven by intense oscillating fields and devise an analytic solution for multiphoton dynamics in the strongly driven qubit.

This dissertation is organized as follows. In Chapter 2, we introduce a new VFD method for solving the Schrödinger, Kohn–Sham, and Poisson equations for electronic structures of polyatomic molecules [51]. The high-order VFD method is also proposed with open prospects at the end of this chapter. In Chapter 3, we develop a new TDVFD method for an accurate and efficient solution of self-interaction-free TDDFT for polyatomic molecules [52]. We present detailed studies for orientation-dependent MPI of N_2 and H_2O [52] and MPI and PAD of aligned CO_2 [53], as well as HHG of aligned CO_2. In Chapter 4, MMFT is extended for intense frequency-comb laser fields to investigate coherent control of multiphoton resonance dynamics and HHG enhancement for a two-level system [54]. Note that HHG driven by intense frequency-comb laser retains the comb structure for each harmonic [55]. In Chapter 5, we extend the Floquet theory for the strongly driven qubit system and explore multiphoton quantum interference by numerical and analytical studies [56]. It is concluded with a summary of present works in Chapter 6.

For publications, the author has played an active role to prepare Refs. [51, 52, 53, 54, 56] and a partial role for Ref. [55]. He has developed all computer programs to present numerical results in all above publications.

The proposed novel spatial and temporal treatments to solve TDSE will be able to pave the way toward detailed theoretical studies of attosecond electronic dynamics in polyatomic molecules including multielectron effects, and an universal method for artificial atoms and realistic systems in any shaped intense fields.

Chapter 2

Development of a new grid-based method for the electronic structure calculations of polyatomic molecules: Voronoi-cell finite difference method

We introduce a new numerical grid-based method in three-dimensional (3D) real-space to investigate the electronic structure of polyatomic molecules. The Voronoi-cell finite difference (VFD) method is developed to accurately and efficiently solve the Schrödinger equation on *unstructured* grids with the help of geometrical adaptivity of the Voronoi cells and their natural neighbors. The feature of *unstructured* grids enables us to choose any intuitive pictures for an optimal molecular grid system, so we design highly adaptive multicenter molecular grids which consist of spherical atomic grids located at nuclear positions. In this way, we can circumvent the multicenter Coulomb singularity in all-electron calculations of polyatomic molecules. This new VFD method augmented by multicenter molecular grids is applicable to solve the Schrödinger /

Kohn–Sham equation and the Poisson equation with the all-electron Coulomb potentials, regardless of the coordinate system and the molecular symmetry. For numerical examples, we assess accuracy of the VFD method for electronic structures of one-electron polyatomic systems, and apply the method to the density-functional theory (DFT) for many-electron polyatomic molecules. Furthermore, the VFD method is advantageously suitable for time-dependent calculations because it does not demand massive integration to construct the time-dependent Hamiltonian. Extension to time-dependent VFD method and its many applications will be described in details in Chapter 3.

2.1 Grid-based methods for electronic structure and dynamics calculations

The structure and motion of electrons in molecules are the most fundamental topics in atomic and molecular physics and quantum chemistry. The basis set expansion method based on linear combination of atomic orbitals (LCAO) [57] is one of the most conventional methods in quantum chemistry to investigate molecular electronic structures. Despite its wide spread of usage, there have been several drawbacks in the LCAO scheme, such as massive integrals, slow convergence for basis sizes, basis set superposition error [58], and linear dependence problems [59]. In particular, the basis set expansion method based on localized atomic orbitals hinders from exploring strong-field electronic dynamics which inevitably cover long-range motions of the electrons, even though there have been several attempts to use the basis set expansion in strong-field time-dependent calculations [60]. On the opposite side, the numerical grid-based method to solve the Hamiltonian directly represented in real-space grids [61]

has been chosen for describing electronic dynamics, widely in atomic and molecular physics. It is relatively easy for the grid method to be extended to excited/continuum states in electronic dynamics by including long-range grid points, but it requires local refinement of grids to accurately compute even electronic structures of polyatomic molecules, which are prerequisite for electronic dynamics.

From the numerical aspect, the multicenter Coulomb singularity is a key bottleneck for the accurate treatment of electronic structure and dynamics in polyatomic molecules. The Coulomb potential (=$1/r$) in the all-electron Hamiltonian of atoms and molecules incorporates cusps at nuclear positions in electronic wavefunctions, which is called Coulomb singularity [62] that significantly affects accuracy of electronic bound states. The realistic Coulomb potential also influences highly-excited and continuum electrons due to its long-range behavior. The importance of Coulomb effect in the continuum states has been explicitly discussed for strong-field ionization process [63] and high-order harmonic generation [64, 65].

To achieve both the short- and long-range manners of the realistic Coulomb potential, Professor Chu's group [41, 49, 50, 66, 67] has developed the generalized pseudospectral (GPS) method and time-dependent generalized pseudospectral (TDGPS) method on an optimal nonuniform grid system which has denser grid points near the nuclear positions and sparser grid points away from the nuclei. For atomic systems with the spherical coordinates [41] and diatomic systems with the prolate spheroidal coordinates [50, 66, 67], the GPS method has brought in machine accuracy to electronic structure calculations and the TDGPS method has achieved a remarkable success in calculations of strong-

field electronic dynamics such as multiphoton ionization and high-order harmonic generation (for examples, see Ref. [49] and references therein).

As the number of nuclei goes beyond uniatomic and diatomic systems, however, it is not trivial to employ a coordinate system suitable for arbitrary geometries of polyatomic molecules. From this viewpoint, numerical methods on *unstructured* grids [68], which have no fixed number for connectivity among grids, become much attractive for calculations of polyatomic molecules. On *unstructured* grids we can construct highly adaptive *nonuniform* molecular grids with variable resolutions around nuclear positions, regardless of the coordinate system and the molecular symmetry.

For an optimal molecular grid system, it is natural to consider that molecular grids consist of a combination of spherical atomic grids centered at nuclear positions, which can be called multicenter molecular grids. This intuitive idea was introduced and implemented by Becke [69] and Dickson and Becke [70] for basis-set-free DFT calculations. Becke's procedure was based on multicenter numerical integration [71, 72] and solved the Schrödinger equation by means of the single-center decomposition with the spherically-averaged approximation [73], rather than a direct solution on molecular grids. The direct solution on such a multicenter molecular grid distribution is most desirable but not trivial with conventional numerical grid-based methods.

To directly solve the Schrödinger equation or, more generally, the partial differential equations (PDE) on *unstructured* grids (e.g., multicenter molecular grids), one can imagine the Voronoi diagram [74, 75, 76]. Because the Voronoi diagram is geometrically attractive and versatile, there have been tremendous applications in various areas of science and engineering over one century [77, 78]. However, a PDE solver exploiting geometrical advantages of the Voronoi

diagram has not been considered until relatively recent years. In geophysics and solid mechanics, the natural element method (NEM) [79] and the natural neighbor Galerkin method (NNGM) [80, 81] have been developed to realize PDE solutions on *unstructured* grids with the help of Voronoi diagram. More recently, Sukumar [82] and Sukumar and Bolander [83] proposed the discrete Laplacian operator for numerical solutions of the Poisson equation on *unstructured* grids based on the finite difference scheme with Voronoi cells and natural neighbors, and named it the Voronoi-cell finite difference (VFD) method. Because there is no restriction on the location of grid points, the VFD method with arbitrary *unstructured* grids is regarded as a meshfree (or meshless) method, which is of current interest in computer modeling and simulation in engineering applications [84, 85]. Even though an idea to exploit the Voronoi diagram in electronic structure calculations has been reported [86], no practical implementation for the electronic structure has been accomplished in this direction until now.

We first extend VFD to solve the Schrödinger / Kohn–Sham equation and the Poisson equation for electronic structures of polyatomic molecules with the all-electron realistic Coulomb potential on multicenter molecular grids. There have been many grid-based approaches suggested to attack the multicenter Coulomb singularity with local grid refinement in real-space: for examples, finite element [87, 88, 89], spectral element [90], curvilinear adaptive coordinate [91, 92], multigrid [93, 94, 95], multiresolution analysis with wavelet [96, 97, 98], multicenter B-spline [99], and a hybrid combination of basis set expansion and discrete variable representation [100] (for more examples, see Ref. [61] and references therein). Also, one of the most popular grid-based methods is the high-order finite difference method with the pseudopotential on uniform

Cartesian grids [101, 102]. Notable features of the proposed VFD method over these previous approaches are summarized as follows: (i) High adaptivity: by means of *unstructured* grids there is no restriction on local grid refinement for polyatomic molecules regardless of molecular symmetry. (ii) Simplicity: VFD provides a simple and explicit matrix form of the discrete Laplacian operator, which realizes a direct solution of the Schrödinger equation and the Kohn–Sham equation on *unstructured* grids, as well as a simple implementation of the Poisson equation. (iii) No massive integration: the potential matrix is given by a value at each grid and the Hamiltonian matrix is constructed without any integration. (iv) Realistic Coulomb potential: VFD allows us to solve the realistic Coulomb potential in 3D rather than model potentials in order to correctly simulate the short- and long-range features of the Coulomb potential. Furthermore, it can be extended for the time-dependent calculations with capturing accuracy of the bound states and expansibility to the continuum states, because it does not need massive integration for potentials at each time step in time-propagation.

2.2 Voronoi-cell finite difference method

2.2.1 Voronoi discretization

Given an arbitrarily distributed grid-point set $\{\mathbf{r}_i\}$ in n-dimensions, a Voronoi cell surrounding a grid of $\mathbf{r}_i$ is defined by a set of points that are closer to $\mathbf{r}_i$ than to any other grids [78],

$$T_i \equiv \{\mathbf{r} \in \mathbb{R}^n : d(\mathbf{r}, \mathbf{r}_i) \leq d(\mathbf{r}, \mathbf{r}_j) \text{ for } \forall j \neq i\}, \tag{2.1}$$

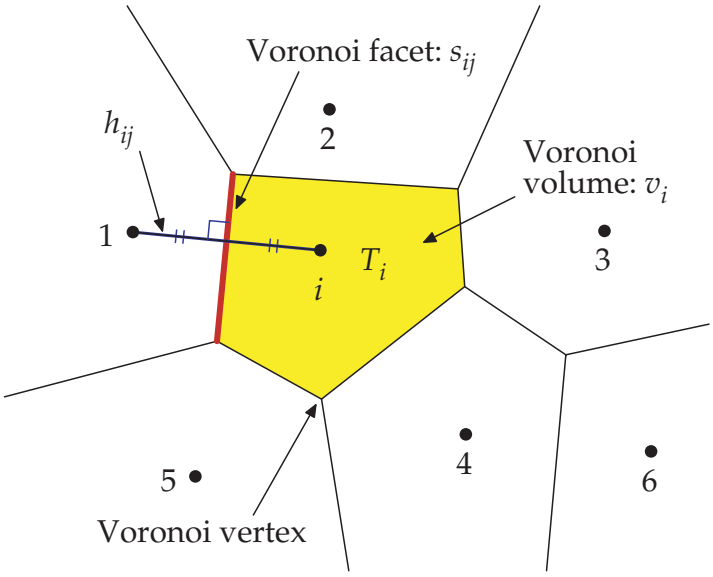

Figure 2.1: Voronoi diagram on arbitrarily distributed grid points

where $d(\mathbf{r}_i, \mathbf{r}_j)$ is a distance between two points $\mathbf{r}_i$ and $\mathbf{r}_j$. It is well known that the Voronoi diagram is uniquely defined for a given grid-point set [78]. Thus from the Voronoi diagram the whole space is uniquely discretized into Voronoi cells and each grid point is enclosed by cells. Figure 2.1 shows one example of the Voronoi diagram in the 2-dimensional (2D) case and some related symbols that are defined as follows.

The Voronoi cell is denoted as T_i encapsulating the ith grid, and its volume is given by v_i. A Voronoi facet s_{ij} is the surface where two adjacent T_i and T_j meet together. Note that the Voronoi facet is a line in 2D (also called the Voronoi edge) as shown in Fig. 2.1 and a polygon plane in 3D. h_{ij} is a distance between the ith and jth grids,

$$h_{ij} = \|\mathbf{r}_j - \mathbf{r}_i\|. \tag{2.2}$$

One of the Voronoi properties is that s_{ij} is the perpendicular bisector of h_{ij}. A natural neighbor [103] is defined by the fact that if two grids share a common

Voronoi facet, they are natural neighbors. For example, in Fig. 2.1 the grids of 1–5 are natural neighbors of the ith grid but the grid of 6 is not. A Voronoi vertex is defined as the point where Voronoi facets converge. In other words, the Voronoi facet between two neighboring grids is surrounded by the Voronoi vertices belonging to the two grids. Therefore, an area of s_{ij} in 3D (or a length in 2D) can be computed using the position of the surrounding vertices. In the 3D case, the area of the polygon is computed by

$$s_{ij} = \frac{1}{2}\left|\sum_{k=1}^{M} \mathrm{sign}\left\|(\mathbf{p}_k - \mathbf{q}) \times (\mathbf{p}_{k+1} - \mathbf{q})\right\|\right|, \tag{2.3}$$

where $\times$ is the cross product, $\mathbf{q} = (\mathbf{r}_i + \mathbf{r}_j)/2$, M is the number of surrounding vertices for s_{ij}, and $\{\mathbf{p}_k\}$ ($k = 1, \cdots, M$ with $\mathbf{p}_1 = \mathbf{p}_{M+1}$) are position vectors of the vertices. The sign is given by positive when $\mathbf{p}_k$, $\mathbf{p}_{k+1}$, and $\mathbf{q}$ are oriented counterclockwise and negative when clockwise. The Voronoi cell T_i is further decomposed into polygonal pyramids that have their apex at the ith grid and their base as each Voronoi facet, so v_i can be computed by the sum of volumes of these polygonal pyramids,

$$v_i = \frac{1}{6}\sum_{j}^{\text{neighbors}} h_{ij} s_{ij}, \tag{2.4}$$

where j runs over natural neighboring grids of the ith grid.

To summarize, for a given set of arbitrarily distributed grids, the Voronoi discretization is uniquely determined and v_i, s_{ij}, and h_{ij} are easily calculated by Voronoi vertices and natural neighboring relations within the Voronoi diagram. For numerical determination of the Voronoi diagram, we use the QHULL package [104], and all calculations are performed in 3D.

2.2.2 Discrete Laplacian operator

The Gauss' theorem [105] states that

$$\int_V \boldsymbol{\nabla} \cdot \mathbf{F}\, dV = \int_S \mathbf{F} \cdot \mathbf{n}\, dS. \tag{2.5}$$

From this theorem, the Laplacian acts on a function φ is defined by the integral form in the limit that the volume is small,

$$\boldsymbol{\nabla}^2 \varphi = \lim_{\int_V dV \to 0} \frac{\int_S \boldsymbol{\nabla}\varphi \cdot \mathbf{n}\, dS}{\int_V dV}, \tag{2.6}$$

where $\mathbf{n}$ is the normal unit vector of the surface S. To find the discrete Laplacian form at a grid i, imagine the Voronoi cell corresponding to the ith grid. After the Voronoi discretization, the volume in the vicinity of the ith grid can be given by the Voronoi cell T_i. Then the volume integral is converted into the Voronoi volume v_i,

$$\int_{V \subset T_i} dV \to v_i, \tag{2.7}$$

and the surface integral is decomposed into the areas of the Voronoi facets s_{ij} over the neighboring grid j's,

$$\int_{S \subset \partial T_i} \boldsymbol{\nabla}\varphi \cdot \mathbf{n}\, dS \to \sum_j^{\text{neighbors}} (\boldsymbol{\nabla}\varphi)_i \cdot \mathbf{n}_{ij} s_{ij}, \tag{2.8}$$

where ∂T_i indicates the boundary surface of T_i. Here the inner product indicates a directional derivative of φ, which is given by the projection of $\boldsymbol{\nabla}\varphi$ on the normal vector of the Voronoi facet. Because a line between neighboring grids i and j is perpendicular to the corresponding Voronoi facet, the directional derivative at the ith grid in the direction to the neighboring grid j can be evaluated by the

simple difference scheme,

$$(\boldsymbol{\nabla}\varphi)_i \cdot \mathbf{n}_{ij} \approx \frac{\varphi_j - \varphi_i}{h_{ij}}. \tag{2.9}$$

Thus the discrete Laplacian at the ith grid in the VFD scheme can be evaluated by [82, 83]

$$\left(\boldsymbol{\nabla}^2\varphi\right)_i = \frac{1}{v_i} \sum_{j}^{\text{neighbors}} \frac{\varphi_j - \varphi_i}{h_{ij}} s_{ij}. \tag{2.10}$$

Note that this scheme relies on two computational approximations: firstly the volume of the Voronoi cell is small in the limit of Eq. (2.6), and secondly the finite difference scheme is used for the directional derivative in Eq. (2.9). Once v_i, s_{ij}, and h_{ij} for given grid points are available, one can simply and explicitly compute the Laplacian in the framework of VFD.

From Eq. (2.10), the matrix form of the Laplacian operator $\mathbf{L}$ in VFD is expressed as

$$\mathbf{L}: \; L_{ij} = \begin{cases} -\dfrac{1}{v_i} \displaystyle\sum_{k}^{\text{neighbors}} \dfrac{s_{ik}}{h_{ik}} & (i = j), \\ \dfrac{1}{v_i}\dfrac{s_{ij}}{h_{ij}} & (i, j\text{: neighbors}), \\ 0 & (\text{otherwise}), \end{cases} \tag{2.11}$$

where k runs over natural neighbors of the ith grid. Note that $\mathbf{L}$ is not symmetric ($L_{ij} \neq L_{ji}$) due to v_i.

A remarkable distinction between VFD and ordinary finite difference (FD) method with regular uniform grids is that VFD on *unstructured* grids can accommodate any types of grid distributions. Thus the VFD method is compared with the generalized finite difference (GFD) method [106, 107] that also can accommodate irregular grids. GFD usually employs the Taylor expansion and

solves a linear system of equations to compute the first and second derivative quantities at every grid. Therefore GFD does not provide explicit expressions of the Laplacian matrix elements and in many cases the matrix involved in the linear system of equations becomes ill-conditioned, whereas VFD offers the explicit forms of the Laplacian matrix elements that unconditionally exist.

Also the VFD scheme resembles the finite volume method (FVM) [108, 109, 110] because both are based on the Gauss' theorem and utilize cell volumes to derive basic formula. However, VFD substitutes the volume integral with the Voronoi volume and the surface integral with the simple finite difference form of the directional derivatives, while FVM generally evaluates those integrals using interpolation and quadrature. As a result, VFD provides the simple and explicit expressions at each grid without additional background grids.

2.2.3 Symmetrization of the Hamiltonian matrix

In this section, we discuss how to solve the time-independent Schrödinger equation with the symmetrized VFD Hamiltonian matrix [51]. One can directly use the discrete Laplacian operator in VFD to solve the Schrödinger equation for one electron,

$$\left[-\frac{1}{2}\boldsymbol{\nabla}^2 + u(\mathbf{r})\right]\psi(\mathbf{r}) = \varepsilon\psi(\mathbf{r}), \tag{2.12}$$

where $u(\mathbf{r})$ is a potential function, $\psi(\mathbf{r})$ is an eigenfunction, and ε is an eigenvalue. Note that the atomic units are used throughout the dissertation, unless otherwise indicated. The reduced mass of the electron is set to the unity in the atomic units. In the matrix representation, the Hamiltonian matrix is given by

$$\mathbf{H} = -\tfrac{1}{2}\mathbf{L} + \mathbf{U}, \tag{2.13}$$

where $\mathbf{U}$ is a potential matrix and given by diagonal elements evaluated at each grid,

$$\mathbf{U}: \ U_{ij} = \delta_{ij} u(\mathbf{r}_i). \tag{2.14}$$

Then, the eigenvalue problem to be solved is

$$\mathbf{HC} = \mathbf{CE}, \tag{2.15}$$

where $\mathbf{C}$ is the eigenvector matrix and $\mathbf{E}$ is the diagonal matrix of eigenvalues. Since $\mathbf{L}$ is non-symmetric, it is advantageous to transform $\mathbf{H}$ into a symmetric form to facilitate the eigenvalue solution.

Here we introduce a transformation of $\tilde{\mathbf{C}} = \mathbf{V}^{\frac{1}{2}}\mathbf{C}$ where $\mathbf{V}$ is given by diagonal elements of Voronoi volumes,

$$\mathbf{V}: \ V_{ij} = \delta_{ij} v_i, \tag{2.16}$$

and then $\mathbf{V}^{\frac{1}{2}}$ is given by diagonal elements of $\sqrt{v_i}$ and $\mathbf{V}^{-\frac{1}{2}}$ by $1/\sqrt{v_i}$. When $\mathbf{C} = \mathbf{V}^{-\frac{1}{2}}\tilde{\mathbf{C}}$ is substituted into Eq. (2.15), one obtains

$$\left(-\tfrac{1}{2}\mathbf{L} + \mathbf{U}\right)\mathbf{V}^{-\frac{1}{2}}\tilde{\mathbf{C}} = \mathbf{V}^{-\frac{1}{2}}\tilde{\mathbf{C}}\mathbf{E}, \tag{2.17a}$$

$$\mathbf{V}^{\frac{1}{2}}\left(-\tfrac{1}{2}\mathbf{L} + \mathbf{U}\right)\mathbf{V}^{-\frac{1}{2}}\tilde{\mathbf{C}} = \tilde{\mathbf{C}}\mathbf{E}, \tag{2.17b}$$

$$\left(-\tfrac{1}{2}\mathbf{V}^{\frac{1}{2}}\mathbf{L}\mathbf{V}^{-\frac{1}{2}} + \mathbf{U}\right)\tilde{\mathbf{C}} = \tilde{\mathbf{C}}\mathbf{E}, \tag{2.17c}$$

where $\mathbf{V}^{\frac{1}{2}}\mathbf{U}\mathbf{V}^{-\frac{1}{2}} = \mathbf{U}$ is used because both $\mathbf{U}$ and $\mathbf{V}$ are diagonal matrices. Using a similarity transformation of $\mathbf{L}$,

$$\tilde{\mathbf{L}} = \mathbf{V}^{\frac{1}{2}}\mathbf{L}\mathbf{V}^{-\frac{1}{2}}, \tag{2.18}$$

one obtains a symmetric matrix $\tilde{\mathbf{L}}$. The explicit expressions for $\tilde{\mathbf{L}}$ elements are

$$\tilde{\mathbf{L}}: \ \tilde{L}_{ij} = \begin{cases} -\dfrac{1}{v_i} \displaystyle\sum_{k}^{\text{neighbors}} \dfrac{s_{ik}}{h_{ik}} & (i = j), \\ \dfrac{1}{\sqrt{v_i v_j}} \dfrac{s_{ij}}{h_{ij}} & (i, j: \text{neighbors}), \\ 0 & (\text{otherwise}). \end{cases} \tag{2.19}$$

Note that VFD provides a very sparse matrix because it consists of diagonal elements and nonzero elements only at natural neighboring indexes.

Now one can solve the symmetric eigenvalue problem with $\tilde{\mathbf{H}} = -\frac{1}{2}\tilde{\mathbf{L}} + \mathbf{U}$ instead of Eq. (2.15),

$$\tilde{\mathbf{H}}\tilde{\mathbf{C}} = \tilde{\mathbf{C}}\mathbf{E}. \tag{2.20}$$

After solving $\tilde{\mathbf{H}}$, the eigenvectors are recovered by $\mathbf{C} = \mathbf{V}^{-\frac{1}{2}}\tilde{\mathbf{C}}$,

$$c_i^{(k)} = \frac{\tilde{c}_i^{(k)}}{\sqrt{v_i}}, \tag{2.21}$$

where $c_i^{(k)}$ and $\tilde{c}_i^{(k)}$ are values at the ith grid of the kth eigenvector of $\mathbf{H}$ and $\tilde{\mathbf{H}}$, respectively. Note that for electronic structure calculations of polyatomic molecules $c_i^{(k)}$ has cusps in the vicinity of nuclear positions due to the Coulomb singularity. If the grid distribution is designed to let v_i be small enough around nuclear positions, the solution of $\tilde{c}_i^{(k)}$ can be smoothed out near cusps of $c_i^{(k)}$ because of Eq. (2.21). A multicenter molecular grid distribution is introduced in Section 2.2.5 for this purpose. The eigenvalues of this real symmetric sparse matrix are numerically determined by the implicitly restarted Lanczos method of ARPACK [111] and the large sparse matrix solver of PARDISO [112].

When a numerical integral is required, for examples, computations of the energy functionals in Section 2.3 or the ionization probability in Section 3.3, a set of Voronoi volumes $\{v_i\}$ works as weights in the nodal quadrature method [113] without additional background cells or grids. The integral in the VFD scheme is simply evaluated by the summation over all grids,

$$\int_V f(\mathbf{r})dV \approx \sum_i^{\text{all}} f(\mathbf{r}_i)v_i. \tag{2.22}$$

2.2.4 Discrete gradient operator

In this section, we derive a discrete gradient operator in the VFD scheme as the same manner as the Laplacian operator in Section 2.2.2. One can recall an alternative form of the Gauss' theorem [105],

$$\int_V \boldsymbol{\nabla} f \, dV = \int_S f\mathbf{n} \, dS. \tag{2.23}$$

The gradient is defined in the integral form,

$$\boldsymbol{\nabla}\varphi = \lim_{\int_V dV \to 0} \frac{\int_S \varphi\mathbf{n} \, dS}{\int_V dV}. \tag{2.24}$$

The gradient at the ith grid is given by the summation over Voronoi facet areas divided by the Voronoi volume after the Voronoi discretization. To evaluate the surface integral over S, φ on S is approximated to $(\varphi_i + \varphi_j)/2$ on s_{ij} because s_{ij} is the perpendicular bisector of h_{ij}. Utilizing $\sum_j \mathbf{n}_{ij}s_{ij} = \mathbf{0}$ and the normal vector on s_{ij} by $\mathbf{n}_{ij} = (\mathbf{r}_j - \mathbf{r}_i)/h_{ij}$, one obtain the discrete gradient at the ith grid in the

VFD scheme as

$$(\boldsymbol{\nabla}\varphi)_i = \frac{1}{v_i}\sum_{j}^{\text{neighbors}} \frac{\varphi_j + \varphi_i}{2}\mathbf{n}_{ij}s_{ij} = \frac{1}{2v_i}\sum_{j}^{\text{neighbors}} \frac{\varphi_j s_{ij}(\mathbf{r}_j - \mathbf{r}_i)}{h_{ij}}.$$

Note that this expression using the middle point of φ_i and φ_j is different from the gradient operator using the center of mass of the Voronoi facet [114]. The matrix form of the x-component of the gradient operator $\mathbf{G}^{(x)}$ is expressed as

$$\mathbf{G}^{(x)} : \; G_{ij}^{(x)} = \begin{cases} 0 & (i = j), \\ \dfrac{1}{2v_i}\dfrac{s_{ij}}{h_{ij}}(\mathbf{r}_j - \mathbf{r}_i)\cdot\hat{\mathbf{e}}_x & (i, j\text{: neighbors}), \\ 0 & (\text{otherwise}), \end{cases} \tag{2.25}$$

where $\hat{\mathbf{e}}_x$ is the unit vector of the x-axis. Also $\mathbf{G}^{(y)}$ and $\mathbf{G}^{(z)}$ are defined likewise. Note that the gradient operator is intrinsically non-symmetric.

2.2.5 Multicenter molecular grids

In the real-space grid method, local refinement around nuclear positions is requisite to capture the multicenter Coulomb singularity. The VFD method realizes highly adaptive local refinement with *unstructured* grids. In the grid generation [68], *unstructured* refers to the grid system that there is no fixed number for connectivity among grids, while *structured* means that there is a fixed number for connectivity among grids. Since the *unstructured* scheme grants us the freedom to choose any arbitrary grid distributions, it may be possible to optimize molecular grids in a highly *structured manner*, which means that we can design highly adaptive nonuniform molecular grids according to molecu-

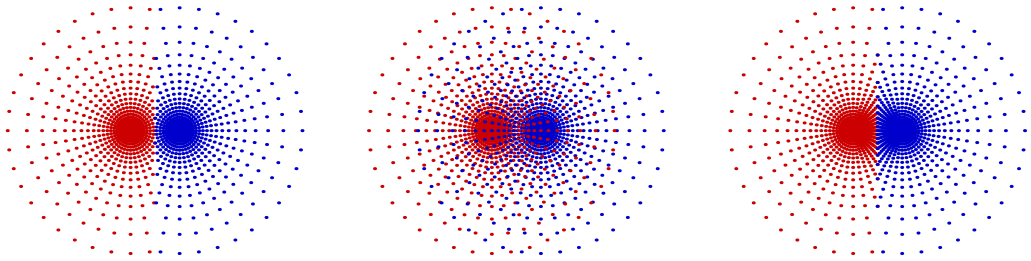

(a) Non-overlap (b) Overlap (c) Squeezed

Figure 2.2: 2D sketches of different types of molecular grids

lar structures. Even though an optimal molecular grid system may be reflected by the molecular structure, there is no limitation on the coordinate system and the molecular symmetry because the design of molecular grids is based on *unstructured* grids.

For polyatomic molecular calculations, it is natural and intuitive to consider spherical atomic grids located at nuclear positions and combine them together to locate more grids near each nucleus. Figure 2.2 shows 2D sketches of three different types of multicenter molecular grids in this manner of composite grids. Note that all calculations are done in 3D molecular grid systems. (a) Non-overlapping composite grids: the atomic grids are combined and the grids in the overlapping region are removed except ones closer to the atom that each grid belongs to. As a result, the sphere of the atomic grids is cut out when it overlaps with others. (b) Overlapping composite grids: all overlapping grids are kept except two grid positions exactly coincide. (c) Squeezed composite grids: to avoid the overlap, the maximum radius of the atomic grids is varied when it meets with others. As a result, the sphere of the atomic grids is squeezed. Among these three types, the non-overlap one has the smallest

number of grids because some grids in the overlap are cut out. The numerical results for three different types will be compared in Section 2.4.

Note that the grid distribution of the overlapping composite grids in this manner is exactly matched to the one used in Becke's basis-set-free DFT calculation [69, 70]. Differences from Becke's scheme are that in VFD there is no single-center decomposition and the Schrödinger equation is directly solvable on this grid distribution, which remarkably simplifies the numerical algorithm and implementation.

To achieve more local refinement in the vicinity of nuclei, the radial part of the spherical atomic grids is generated by an algebraic mapping function [115] in two different ways. First, the mapping function is given by

$$r(x) = L\frac{1+x}{1-x} \quad (-1 < x < 1), \tag{2.26}$$

where L is a mapping parameter and x is defined as uniform grid points in 1D,

$$x_i = \frac{2i}{N_r+1} - 1 \quad (i = 1, \cdots, N_r), \tag{2.27}$$

where N_r is the number of radial grids. Thus, the grid location in the radius ranges from $L/(2N_r+1)$ to LN_r, realizing dense grid points near the nuclear position. Second, the mapping function with a finite maximum radius $r_{\max}$ is given by

$$r(x) = L\frac{1+x}{1-x+\frac{2L}{r_{\max}}} \quad (-1 < x \leq 1), \tag{2.28}$$

and x is defined as uniform grid points in 1D,

$$x_i = \frac{2i}{N_r} - 1 \quad (i = 1, \cdots, N_r). \tag{2.29}$$

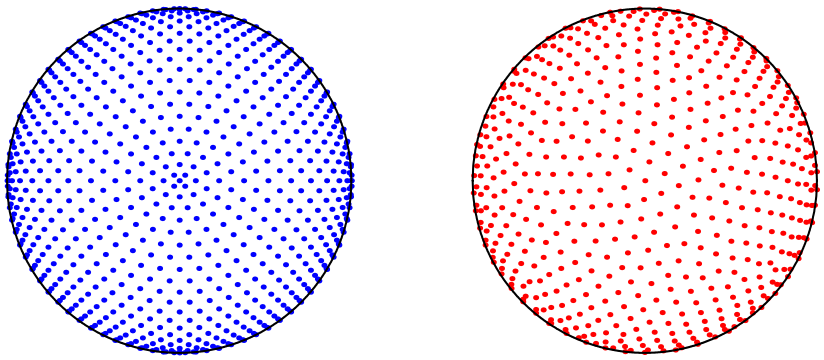

(a) Lebedev grids (b) Womersley grids

Figure 2.3: Comparison between two angular grid distributions plotted over the half sphere.

In this way, the grid location ranges from $L/\{(1+L/r_{\max})N_r - 1\}$ to $r_{\max}$ and still realizes dense grids near the nucleus.

For the angular part of the spherical atomic grids, we adopt angular gird distributions from the Lebedev quadrature [116, 117, 118] and the Womersley quadrature [119, 120]. The former has been widely used in multicenter numerical integration [71, 72]. Figures 2.3 compares the Lebedev and Womersley grid distributions for $l_{\max}$=32 that is the order of angular grids and also indicates the maximum angular momentum. The Lebedev grids retain the octahedral symmetry, so their distribution is to some extent biased around x, y, and z-axes. For a given $l_{\max}$, the number of angular grids is estimated by $N_{\text{ang}} \approx 4(l_{\max}+1)^2/3$. On the other side, the Womersley grids are designed to be fairly uniform over the sphere, and the number of angular grids is exactly given by $N_{\text{ang}} = (l_{\max}+1)^2$. Since numerical results of eigenvalues for both grid types show a very small difference ($\ll 5 \times 10^{-5}$ a.u. for $l_{\max}$=10), we will use either the Lebedev scheme or the Womersley scheme case by case. The rule

of thumb is that the Womersley scheme is more efficient because it offers the smaller N_r for a given $l_{\max}$, but the Lebedev scheme is more useful for better accuracy, especially for accurate dipole moments in HHG calculations in Section 3.8, because it preserves the symmetry.

There are only four parameters to build up spherical atomic grids: N_r, L, and $r_{\max}$ for the radial part, and $l_{\max}$ for the angular part. Also, it is possible to have only three parameters if $r_{\max}$ is not specified. For further calculations, we will use Eqs. (2.26) and (2.27) when N_r, L, and $l_{\max}$ are specified, and will use Eqs. (2.28) and (2.29) when all four parameters, N_r, L, $r_{\max}$, and $l_{\max}$ are specified.

Using the non-overlap scheme, we can construct molecular grids from the spherical atomic grids for the VFD calculations. Figure 2.4 shows 2D sketches of four examples of molecular grids: diatomic nitrogen N_2, linear triatomic carbon dioxide CO_2, bent triatomic water H_2O, and benzene C_6H_6. One can observe that molecular grids are highly adaptive satisfying more grid points around nuclei.

2.3 Application to density-functional theory

Now we apply the VFD method developed in the previous section to accurately compute the electronic structure of many-electron polyatomic molecules using the density-functional theory (DFT) [121]. The DFT states the total energy can be obtained by energy functional [122],

$$E_{\text{total}} = E[\rho] = T_{\text{s}}[\rho] + J[\rho] + E_{\text{ne}}[\rho] + E_{\text{xc}}[\rho_\uparrow, \rho_\downarrow], \tag{2.30}$$

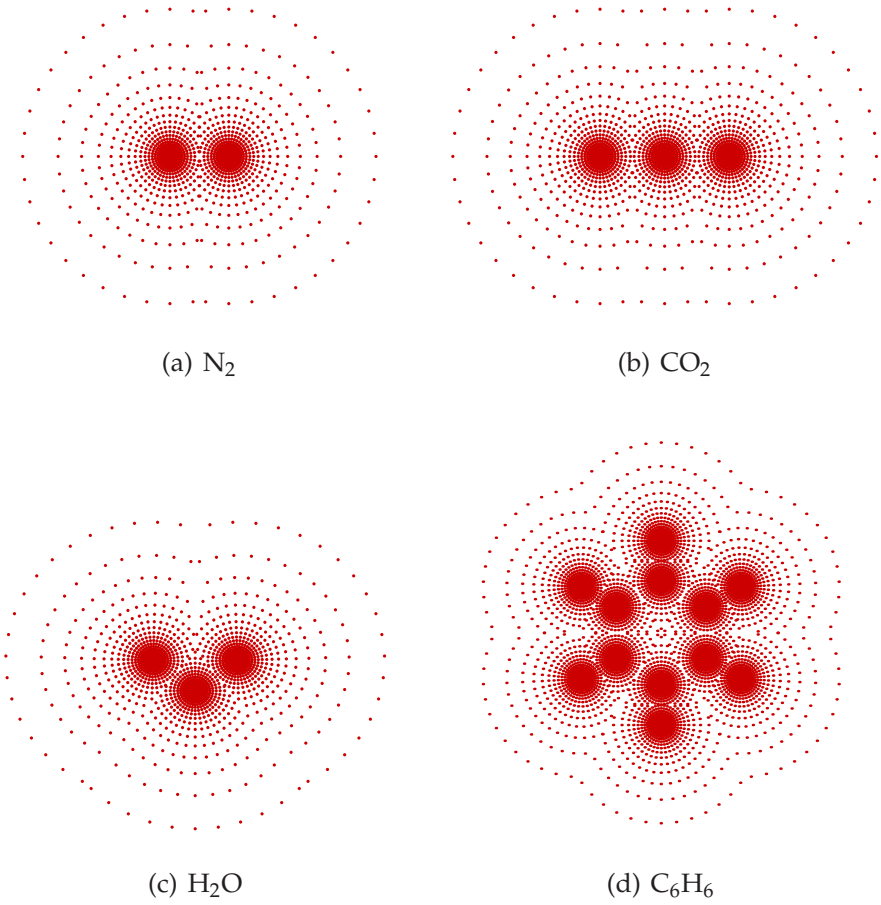

(a) N_2 (b) CO_2

(c) H_2O (d) C_6H_6

Figure 2.4: Examples of multicenter molecular grids (2D sketches) used in the Voronoi-cell finite difference method

where ρ is the total density, and $\uparrow$ and $\downarrow$ indicate spin-up and spin-down, respectively. $T_s[\rho]$ is the noninteracting kinetic energy functional, $J[\rho]$ is the classical electron–electron repulsion energy functional,

$$J[\rho] = \frac{1}{2}\iint \frac{\rho(\mathbf{r})\rho(\mathbf{r}')}{|\mathbf{r}-\mathbf{r}'|} d\mathbf{r} d\mathbf{r}', \tag{2.31}$$

and $E_{ne}[\rho]$ is the nucleus–electron Coulomb interaction energy functional,

$$E_{ne}[\rho] = \int \sum_A \frac{Z_A \rho(\mathbf{r})}{|\mathbf{r}-\mathbf{R}_A|} d\mathbf{r}, \tag{2.32}$$

where $\mathbf{R}_A$ and Z_A are the nuclear position and charge of the Ath nucleus, respectively. $E_{xc}[\rho_\uparrow, \rho_\downarrow]$ is the exchange–correlation energy functional whose exact form is unknown and it needs to be approximated.

In the Kohn–Sham DFT formulation [123], one solves the Schrödinger-like equation for N-electron systems,

$$\left[-\frac{1}{2}\boldsymbol{\nabla}^2 + u_{\text{eff},\sigma}(\mathbf{r})\right] \psi_{i\sigma}(\mathbf{r}) = \varepsilon_{i\sigma}\psi_{i\sigma}(\mathbf{r}), \quad (i = 1, 2, ..., N_\sigma) \tag{2.33}$$

where i and σ are the orbital and spin indexes, respectively. N_σ is the number of σ-spin electrons and $N = N_\uparrow + N_\downarrow$. The spin density is given by

$$\rho_\sigma(\mathbf{r}) = \sum_{i=1}^{N_\sigma} |\psi_{i\sigma}(\mathbf{r})|^2, \tag{2.34}$$

and the total density is given by

$$\rho(\mathbf{r}) = \sum_\sigma \rho_\sigma(\mathbf{r}) = \rho_\uparrow(\mathbf{r}) + \rho_\downarrow(\mathbf{r}). \tag{2.35}$$

The effective potential $u_{\mathrm{eff},\sigma}(\mathbf{r})$ consists of three terms,

$$u_{\mathrm{eff},\sigma}(\mathbf{r}) = u_{\mathrm{ne}}(\mathbf{r}) + u_{\mathrm{h}}(\mathbf{r}) + u_{\mathrm{xc},\sigma}(\mathbf{r}). \tag{2.36}$$

In the framework of VFD, detailed expressions for each term are as follows.

(i) Nucleus–electron potential: The Coulomb interaction between the electron and nuclei is given by

$$u_{\mathrm{ne}}(\mathbf{r}) = \sum_A \frac{Z_A}{|\mathbf{r} - \mathbf{R}_A|}. \tag{2.37}$$

Its matrix form in VFD is simply given by diagonal elements evaluated at each grid.

(ii) Hartree potential: The Hartree potential is given by the classical electron–electron repulsion,

$$u_{\mathrm{h}}(\mathbf{r}) = \int \frac{\rho(\mathbf{r}')}{|\mathbf{r} - \mathbf{r}'|} d\mathbf{r}'. \tag{2.38}$$

Alternatively, it is computable by solving the Poisson equation,

$$\boldsymbol{\nabla}^2 u_{\mathrm{h}}(\mathbf{r}) = -4\pi\rho(\mathbf{r}). \tag{2.39}$$

Its discrete form $\mathbf{u}_{\mathrm{h}}$ is simply solvable by a linear system solution of the Laplacian matrix in VFD,

$$\mathbf{L}\mathbf{u}_{\mathrm{h}} = -4\pi\boldsymbol{\rho}, \tag{2.40}$$

where $\mathbf{u}_\mathrm{h}$ and $\boldsymbol{\rho}$ are column vector forms of the Hartree potential and the total density represented in every grid.

$$\mathbf{u}_\mathrm{h} = (\cdots w_i \cdots)^T; \quad w_i = u_\mathrm{h}(\mathbf{r}_i), \tag{2.41}$$

$$\boldsymbol{\rho} = (\cdots \rho_i \cdots)^T; \quad \rho_i = \rho(\mathbf{r}_i). \tag{2.42}$$

Here $\mathbf{L}$ is the VFD Laplacian matrix in Eq. (2.11). After substituting the similarity transformation of Eq. (2.18) into Eq. (2.40), one obtains the symmetric form,

$$\tilde{\mathbf{L}}\tilde{\mathbf{u}}_\mathrm{h} = -4\pi\tilde{\boldsymbol{\rho}}, \tag{2.43}$$

where $\tilde{\mathbf{u}}_\mathrm{h} = \mathbf{V}^{\frac{1}{2}}\mathbf{u}_\mathrm{h}$ and $\tilde{\boldsymbol{\rho}} = \mathbf{V}^{\frac{1}{2}}\boldsymbol{\rho}$. The boundary conditions for the Hartree potential (=Q/r where Q is the total charge of electrons) are easily incorporated within $\tilde{\mathbf{L}}$. Note that the Poisson equation is solved with the same local grid refinement as the Schrödinger equation or the Kohn–Sham equation. Although multicenter molecular grids are introduced to capture the nucleus–electron Coulomb singularity, one can expect that they also take care of the electron–electron Coulomb singularity because the total electronic density is localized near the nuclear positions.

(iii) Exchange–correlation potential: The simplest form of the exchange–correlation potential is local spin-density approximation (LSDA) [121], which consists of the Slater exchange part [124],

$$u_{\mathrm{x},\sigma}^{\mathrm{LSDA}}(\mathbf{r}) = -\left[\frac{6}{\pi}\rho_\sigma(\mathbf{r})\right]^{1/3}, \tag{2.44}$$

and the Vosko–Wilk–Nusair (VWN) correlation part [125] whose practical implementation is found in Ref. [126]. Thus, LSDA is also known as SVWN in

many quantum chemistry program packages [126]. However, the conventional exchange–correlation functionals, such as LSDA or generalized gradient approximation (GGA), contain spurious self-interaction energy [121] and they do not possess the correct long-range Coulombic $(-1/r)$ behavior. To take into account the proper long-range potential and remove the self-interaction energy, we adopt the improved Leeuwen–Baerends (LBα) potential [127, 128],

$$u_{\mathrm{xc},\sigma}^{\mathrm{LB}\alpha}(\mathbf{r}) = \alpha u_{\mathrm{x},\sigma}^{\mathrm{LSDA}}(\mathbf{r}) + u_{\mathrm{c},\sigma}^{\mathrm{LSDA}}(\mathbf{r}) - \frac{\beta x_\sigma^2(\mathbf{r})\rho_\sigma^{1/3}(\mathbf{r})}{1 + 3\beta x_\sigma(\mathbf{r}) \log\left(x_\sigma(\mathbf{r}) + \sqrt{x_\sigma^2(\mathbf{r}) + 1}\right)}, \tag{2.45}$$

where $x_\sigma(\mathbf{r}) = |\boldsymbol{\nabla}\rho_\sigma(\mathbf{r})|/\rho_\sigma^{4/3}(\mathbf{r})$. Note that α and β are two adjustable parameters in the LBα potential. $u_{\mathrm{x},\sigma}^{\mathrm{LSDA}}$ and $u_{\mathrm{c},\sigma}^{\mathrm{LSDA}}$ indicate the exchange and correlation potentials of LSDA, respectively, and in this case we use the Perdew–Wang representation for the correlation functional [129]. To assure the asymptotic Coulombic tail of $-1/r$, the Fermi–Amaldi term is smoothly attached for the long-range distance [130]. By means of the VFD gradient operator in Eq. (2.25), $x_\sigma(\mathbf{r})$ at the ith grid is computed by

$$x_\sigma(\mathbf{r}_i) = \frac{\sqrt{\left(g_i^{(x)}\right)^2 + \left(g_i^{(y)}\right)^2 + \left(g_i^{(z)}\right)^2}}{\rho_\sigma^{4/3}(\mathbf{r}_i)}, \tag{2.46}$$

where $g_i^{(x)} = [\boldsymbol{\nabla}\rho_\sigma(\mathbf{r}) \cdot \hat{\mathbf{e}}_x]_i = \sum_j G_{ij}^{(x)} \rho_\sigma(\mathbf{r}_j)$ and likewise for $g_i^{(y)}$ and $g_i^{(z)}$.

2.4 Accuracy assessment for one-electron systems

First, three different types of molecular grids proposed in Section 2.2.5 are tested. Figure 2.5 compares numerical accuracy for choosing three different types as a function of N_r. The y-axis represents absolute errors $|\delta|$ on the ground-state energy of H_2^+, defined by differences between computed values with VFD and an exact value [131]. N_r is varied, and L=1 and $l_{\max}$=20 with Lebedev grids are used. As N_r increases, the ground energies are converged to the exact value. Unresolved errors at large N_r are due to small $l_{\max}$, which can be reduced as $l_{\max}$ increases. The squeezed type always shows better convergence and the overlap type does worse than others, while the non-overlap type becomes close to the squeezed type when N_r increases. Because the non-overlap type has the smallest total number of grids at given N_r and $l_{\max}$, we will use the non-overlap type for further calculations.

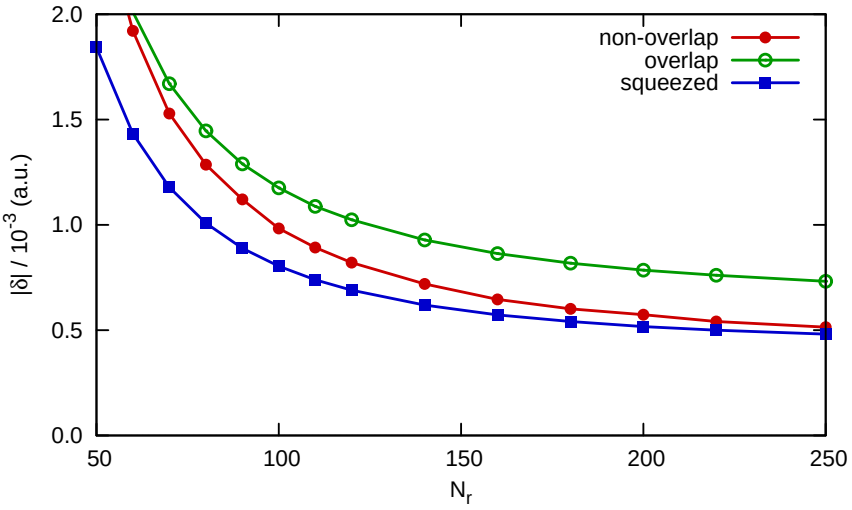

Figure 2.5: Comparison of numerical accuracy for different types of molecular grids.

For the simplest one-electron diatomic system, H_2^+, we perform accuracy tests with respect to N_r and $l_{\max}$. Figures 2.6(a) and (b) plot absolute errors $|\delta|$ of the ground-state energies of H_2^+ as a function of N_r and $l_{\max}$, respectively. The internuclear distance is fixed at R=2.0 a.u. and the Lebedev grids are used for the angular part. Errors are getting smaller as N_r and $l_{\max}$ increase, confirming that accuracy of the VFD method is systematically improved by increasing the number of grids to compute electronic structures with the realistic Coulomb potential. Note that low-lying excited states also show similar trends of convergence as the ground state. Figure 2.6 indicates that the ground-state energies are converged up to the fourth decimal place, i.e., ($|\delta| < 5 \times 10^{-4}$ a.u.) with $N_r \geq 150$ and $l_{\max} \geq 29$.

Table 2.1 lists electronic energies of low-lying bound states of H_2^+ up to first 16 states. All computed energies are lower by less than 2.57×10^{-4} a.u. from the exact values [131] and all error percentages are less than 0.12%. N_r=400, L=1 and $l_{\max}$=47 are used with the Lebedev scheme, the non-overlap type of molecular grids, and the mapping function of Eqs. (2.26) and (2.27). The matrix dimension with these parameters is approximately 2 millions (N_{total}=2,086,662) but it becomes very sparse because VFD considers only closest natural neighbors of each grid. With ARPACK [111] and PARDISO [112], the computation time to solve selected eigenvalues of the 2,086,662×2,086,662 matrix takes about 1.2 hours on the lab workstation equipped with two Intel Xeon X5355 (quad core, 2.66GHz) CPUs. For comparison, Table 2.1 includes results from LCAO performed by GAMESS [132] with a huge basis set of aug-cc-pV6Z [133] that converges systematically to the complete basis set limit. All basis sets used in LCAO calculations through the dissertation are retrieved from BASIS SET EXCHANGE [134]. For the ground and first excited states, the LCAO results agree

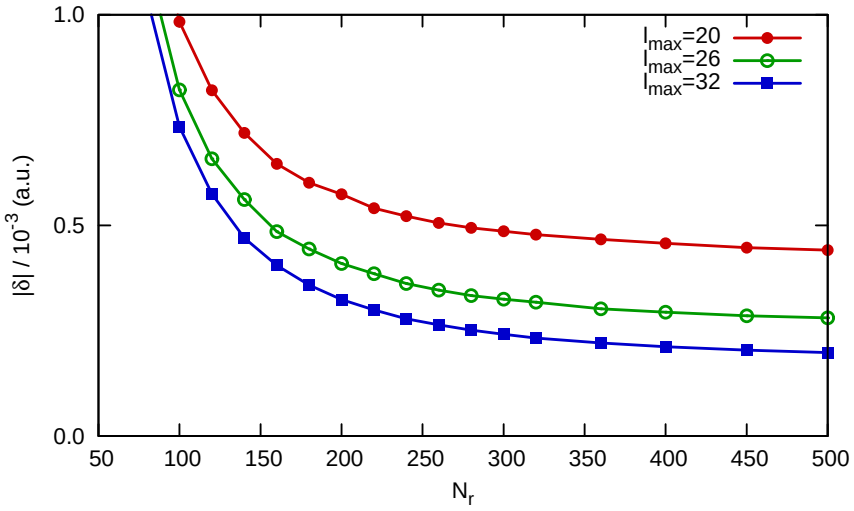

(a) Convergence as N_r increases

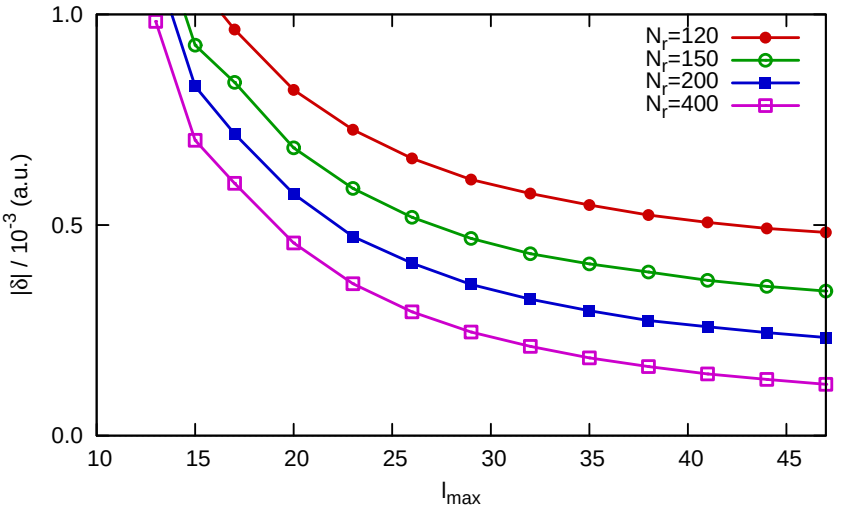

(b) Convergence as $l_{\max}$ increases

Figure 2.6: Accuracy on the ground-state energies of H_2^+ computed by VFD.

Table 2.1: Electronic energies (in a.u.) and numerical errors δ of the ground and excited states of H_2^+ at R=2.0 a.u. The number in parentheses in orbital symmetry indicates degeneracy.

		LCAO		VFD	
Orbital	Exact [131]	δ (a.u.)	$\lvert\delta\rvert$ (%)	δ (a.u.)	$\lvert\delta\rvert$ (%)
$1\sigma_g$	$-1.102\,634$	1.41×10^{-6}	0.00	-1.22×10^{-4}	0.01
$1\sigma_u$	$-0.667\,534$	1.69×10^{-6}	0.00	-1.55×10^{-4}	0.02
$1\pi_u(2)$	$-0.428\,772$	1.09×10^{-4}	0.03	-7.92×10^{-5}	0.02
$2\sigma_g$	$-0.360\,865$	5.29×10^{-5}	0.01	-6.65×10^{-5}	0.02
$2\sigma_u$	$-0.255\,413$	2.49×10^{-4}	0.10	-7.14×10^{-5}	0.03
$3\sigma_g$	$-0.235\,778$	3.46×10^{-3}	1.47	-1.20×10^{-4}	0.05
$1\pi_g(2)$	$-0.226\,700$	4.23×10^{-3}	1.87	-1.81×10^{-4}	0.08
$1\delta_g(2)$	$-0.212\,733$	5.40×10^{-2}	25.40	-2.57×10^{-4}	0.12
$2\pi_u(2)$	$-0.200\,865$	6.02×10^{-2}	29.97	-7.81×10^{-5}	0.04
$4\sigma_g$	$-0.177\,681$	1.39×10^{-3}	0.78	-7.70×10^{-5}	0.04
$3\sigma_u$	$-0.137\,313$	6.44×10^{-3}	4.69	-8.55×10^{-5}	0.06
$5\sigma_g$	$-0.130\,792$	3.77×10^{-2}	28.82	-1.05×10^{-4}	0.08

well with exact values but there are remarkable discrepancies in higher excited states. This is not surprising because atomic-centered basis functions in LCAO are optimized for the ground-state calculation. On the other hand, VFD results show fair agreements for all ground and excited states.

Next, we compute the simplest one-electron triatomic molecule, H_3^{++}, that has the equilateral triangular shape. It has been known that triangular H_3^{++} does not exist [135] but there have been a few results for the ground state with a fixed internuclear distance computed by LCAO and FE [87] as the accuracy assessment beyond atoms and diatomic molecules. We note that there have been recent discussions on existence of triangular H_3^{++} in strong magnetic fields [135]. Table 2.2 lists the ground- and excited-state electronic energies of

Table 2.2: Electronic energies (in a.u.) of the ground and excited states of equilateral triangular H_3^{++} at R=1.68 a.u. Δ=$E_{\mathrm{VFD}} - E_{\mathrm{LCAO}}$.

Orbital	FE [87]	LCAO	VFD	Δ
$1a_1'$	−1.909 571	−1.909 569	−1.909 787	-2.18×10^{-4}
$1e'(2)$		−1.138 578	−1.138 979	-4.02×10^{-4}
$1a_2''$		−0.869 699	−0.870 008	-3.10×10^{-4}
$2a_1'$		−0.704 969	−0.705 131	-1.62×10^{-4}
$2e'(2)$		−0.534 978	−0.535 372	-3.93×10^{-4}
$3e'(2)$		−0.484 387	−0.485 081	-6.94×10^{-4}
$1e''(2)$		−0.481 488	−0.481 732	-2.44×10^{-4}
$3a_1'$		−0.479 498	−0.480 741	-1.24×10^{-3}
$2a_2''$		−0.415 434	−0.422 375	-6.94×10^{-3}
$4a_1'$		−0.362 325	−0.362 826	-5.01×10^{-4}
$4e'(2)$		−0.283 203	−0.295 392	-1.22×10^{-2}

H_3^{++} from VFD. For comparison, it includes the results from FE [87] and from LCAO with the aug-cc-pV6Z basis set. The distance between nuclei is fixed at R=1.68 a.u. corresponding to one side of the equilateral triangular shape. For grid parameters, N_r=400, L=1, and l_{max}=41 with the Lebedev grids are used. Note that all VFD results in Table 2.2 are converged up to the third decimal place with respect to the number of grid points. Differences between VFD and LCAO (Δ=$E_{\mathrm{VFD}} - E_{\mathrm{LCAO}}$) get increased for higher excited states.

2.5 Tests of nodal integration

Since energy functionals for DFT calculations in Eq. (2.30) involve integrals over the whole space, accuracy of VFD nodal quadrature integration of Eq. (2.22) needs to be preliminarily assessed for DFT energy calculations. Table 2.3 shows VFD integrals computed by Eq. (2.22) using converged density from LCAO cal-

culations and corresponding exact values of integrals. Error percentages δ (%) of VFD integrals from exact values are also included. Molecular systems are He, H_2, and H_2O representing one-, two-, and three-center problems, respectively. For mapping parameters, L=1 is used for He and H_2, and L=0.5 for all nuclei of H_2O to refine more grids around a heavy atom which has steeper Coulomb potential. The computed integrals include normalization $n[\bar{\rho}]$, nucleus–electron interaction functional $E_{\mathrm{ne}}[\bar{\rho}]$, and exchange-only local density approximation (XLDA) functional $E_{\mathrm{x}}[\bar{\rho}]$,

$$n[\bar{\rho}] = \frac{1}{N_{\mathrm{elec}}} \int \bar{\rho}(\mathbf{r}) d\mathbf{r}, \tag{2.47}$$

$$E_{\mathrm{ne}}[\bar{\rho}] = \int \sum_A \frac{Z_A \bar{\rho}(\mathbf{r})}{|\mathbf{r} - \mathbf{R}_A|} d\mathbf{r}, \tag{2.48}$$

$$E_{\mathrm{x}}[\bar{\rho}] = -\frac{3}{4}\left(\frac{3}{\pi}\right)^{1/3} \int \bar{\rho}(\mathbf{r})^{4/3} d\mathbf{r}, \tag{2.49}$$

where N_{elec} is the number of electrons. Here, $\bar{\rho}$ is converged Gaussian-type orbital (GTO)-based density which consists of linear combination of GTOs obtained from LCAO calculations with a large basis set of aug-cc-pVQZ [136] that nearly converges to the complete basis set limit [133]. Note that exact values of $n[\bar{\rho}]$ and $E_{\mathrm{ne}}[\bar{\rho}]$ are computed by the analytical integration, while an exact value of $E_{\mathrm{x}}[\bar{\rho}]$ is computed by the multicenter numerical integration [71, 72] and fully converged with large quadrature points (N_r=288/N_θ=36/N_ϕ=72). In Table 2.3, the error percentages δ on normalization of density are less than 0.68% and decrease as the number of grids increases. Also the error percentages on other energy functionals are almost the same as ones on the normalization for the same number of grids. Note that these integration errors do not contaminate

solutions of the eigenvalue problem because the Hamiltonian matrix in VFD is constructed without any integration.

Because eigenvectors in VFD computed by Eqs. (2.20) and (2.21) are always normalized to the unity by means of the VFD integration in Eq. (2.22),

$$\int \left|\psi^{(k)}(\mathbf{r})\right|^2 d\mathbf{r} = \sum_i \left|c_i^{(k)}\right|^2 v_i = \sum_i \left|\tilde{c}_i^{(k)}\right|^2 = 1, \tag{2.50}$$

the density computed by VFD becomes smaller than the true density by the amount of the normalization factor $n[\bar{\rho}]$. Even though this factor surely diminishes when the number of grids becomes larger, it affects the exchange–correlation and Hartree potentials computed by the density and successively quality of DFT calculations. From this consideration, the density obtained by VFD can be scaled by the normalization factor computed from the GTO-based density in order to correctly compute the exchange–correlation and Hartree potentials,

$$\rho_{\mathrm{norm}} = \rho \times n[\bar{\rho}]. \tag{2.51}$$

For energy functionals, we also use energy functionals with the normalization factor correction to reduce errors occurring at normalization,

$$E_{\mathrm{norm}}[\rho] = \frac{E[\rho_{\mathrm{norm}}]}{n[\bar{\rho}]}. \tag{2.52}$$

This artificial normalization factor is introduced to compensate for inaccuracy of the simplest nodal quadrature in Eq. (2.22). It is possible to avoid this factor if the high-order scheme of integration is employed.

Table 2.3: Tests of nodal integrals for one-, two-, and three-center problems

Molecule	Grid ($N_r/l_{\max}$)	$n[\bar{\rho}]$	δ (%)	$E_{\mathrm{ne}}[\bar{\rho}]$	δ (%)	$E_{\mathrm{x}}[\bar{\rho}]$	δ (%)
He	120/20	1.006 337	0.63	−6.610 486	0.65	−0.858 062	0.62
	200/26	1.003 578	0.36	−6.591 954	0.36	−0.855 769	0.35
	300/32	1.002 310	0.23	−6.583 447	0.23	−0.854 706	0.23
	400/38	1.001 628	0.16	−6.578 890	0.16	−0.854 130	0.16
	Exact	1.000 000		−6.568 063		−0.852 750	
H_2	120/20	1.006 433	0.64	−3.588 689	0.63	−0.554 628	0.62
	200/26	1.003 620	0.36	−3.578 969	0.36	−0.553 154	0.35
	300/32	1.002 325	0.23	−3.574 453	0.23	−0.552 465	0.23
	Exact	1.000 000		−3.566 205		−0.551 199	
H_2O	120/20	1.006 816	0.68	−199.463 401	0.70	−8.099 123	0.65
	200/26	1.003 743	0.37	−198.845 443	0.38	−8.075 928	0.37
	300/32	1.002 376	0.24	−198.567 578	0.24	−8.065 431	0.24
	Exact	1.000 000		−198.083 473		−8.046 506	

To examine how this normalization factor on the density affects the DFT results, we compare XLDA energies of H_2 with and without the normalization factor correction in Table 2.4. The internuclear distance of H_2 is fixed at R=1.4 a.u. The table includes the highest occupied molecular orbital (HOMO) and total energies. Exact XLDA values for this diatomic molecule are obtained by the GPS method that accurately computes $\varepsilon_{\mathrm{HOMO}} = -0.331\ 463$ a.u. and $E_{\mathrm{total}} = -1.043\ 685$ a.u. with only 20 and 6 grid points for the ξ and η coordinates in the prolate spheroidal coordinates [137]. Note that the HOMO and total energies are getting close to exact values no matter whether the normalization factor correction is included or not. However, the results with the correction show faster convergency than ones without the correction and reach sufficient accuracy with very limited number of grid points.

Table 2.4: XLDA energies (in a.u.) of H_2 at R=1.4 a.u.

Method	Grid (N_r/l_{max})	$\varepsilon_{\mathrm{HOMO}}$	E_{total}
VFD (without correction)	30/10	−0.360 2	−1.084 4
	50/15	−0.343 2	−1.060 6
	80/17	−0.339 1	−1.054 1
	120/20	−0.336 7	−1.050 6
	200/26	−0.334 4	−1.047 5
	300/32	−0.333 4	−1.046 1
VFD (with correction)	30/10	−0.330 5	−1.049 9
	50/15	−0.330 4	−1.045 7
	80/17	−0.331 1	−1.044 8
	120/20	−0.331 3	−1.044 4
	200/26	−0.331 4	−1.044 0
	300/32	−0.331 4	−1.043 9
Exact XLDA [137]		−0.331 5	−1.043 7

2.6 Electronic structure calculations of polyatomic molecules

In the previous sections, we have shown that VFD for one-electron systems provides an accurate and efficient Schrödinger equation solver for polyatomic molecules involving the multicenter Coulomb singularity, and developed VFD implementation for DFT including the normalization factor correction for accurate energy functional calculations. Now we explore the capability of the VFD method to perform DFT calculations of polyatomic molecules, and the importance of the self-interaction-correction DFT for accurate electronic structures.

For molecular geometries, we use experimental equilibrium geometries for the bond length (R) and the bond angle ($\angle$):

(i) N_2: R(N–N)=2.074 a.u. [138],

(ii) F_2: R(F–F)=2.668 a.u. [138],

(iii) CO_2: R(C–O)=2.196 a.u. [139] and $\angle$(O–C–O)=180°,

(iv) H_2O: R(O–H)=1.810 a.u. and $\angle$(H–O–H)=104.48° [140],

(v) NH_3: R(N–H)=1.913 a.u. and $\angle$(H–N–H)=106.67° [139],

(vi) CH_4: R(C–H)=2.054 a.u. [141] and $\angle$(H–C–H)=109.471°,

(vii) C_6H_6: R(C–C)=2.640 a.u. and R(C–H)=2.048 a.u. [139].

First, we present LSDA results for N_2, H_2O, and C_6H_6 molecules to assess numerical accuracy of the VFD method for the DFT calculations. The LSDA potential is chosen for the accuracy test because it is the the simplest potential and has been widely implemented in many quantum chemistry programs. Table 2.5

shows LSDA orbital and total energies computed by VFD and other calculations. FD indicates the fourth-order finite difference method on uniform equal-spacing grids performed by OCTOPUS [142] with the realistic Coulomb potentials. The LCAO results is performed by GAMESS [132] with aug-cc-pVQZ [136] for N_2 and H_2O; and 6-311++G(3df,3pd) [143] for C_6H_6. Note that these LCAO results are nearly converged to the complete basis set limit. The GPS results for diatomic N_2 [66] are also included for comparison. To keep consistency, the internuclear distance of N_2 in this table is R(N–N)=2.072 a.u. following Ref. [66], and then the LCAO values for N_2 are almost exactly matched with the GPS results. The computational parameters for VFD are N_r=300, L=0.5, and $l_{\max}$=32 with the Lebedev scheme for all nuclei of N_2 and H_2O; and N_r=200, L=0.5, and $l_{\max}$=26 with the Lebedev scheme for all nuclei of C_6H_6.

In Table 2.5, one can see that the valence-electron orbital energies by VFD are comparable to ones by LCAO within less than 0.003 a.u., while the core-electron orbital energies show discrepancies of 0.005–0.010 a.u. For the total energy, the VFD results successfully reproduce the LCAO results by 0.030–0.039 a.u. (0.01–0.04%) deviations. On the other hand, the conventional FD on uniform grids is not adequate to handle the Coulomb singularity, so affecting orbital and total energies significantly. For N_2, the valence-electron orbital energies by FD are deviated from the LCAO values by 0.004–0.049 a.u., the core-electron orbital energies by 0.993 a.u., and the total energy by 5.402 a.u. (5.0%). The total energy for H_2O differs from the LCAO value by 1.626 a.u. (2.1%) and for C_6H_6 the deviation is 11.521 a.u. (5.0%). Moreover, FD with equal-spacing grids unavoidably uses a very large number of grid points to resolve the Coulomb singularity. For the N_2 case, the FD grid parameters are Δx=0.1 a.u. and $r_{\max}$=10 a.u., corresponding to N_{total}=4,187,857. In the mean-

Table 2.5: Comparison of LSDA energies (in a.u.) computed by various numerical methods.

Molecule	Orbital	FD	LCAO	VFD	GPS [66]
N_2	$3\sigma_g$	-0.379	-0.383	-0.383	-0.383
	$1\pi_u$	-0.411	-0.437	-0.438	-0.438
	$2\sigma_u$	-0.543	-0.494	-0.494	-0.493
	$2\sigma_g$	-1.048	-1.039	-1.038	-1.040
	$1\sigma_u$	-14.958	-13.965	-13.971	-13.964
	$1\sigma_g$	-14.959	-13.967	-13.972	-13.966
	E_{total}	-114.100	-108.698	-108.737	
H_2O	$1b_1$	-0.281	-0.272	-0.273	
	$3a_1$	-0.341	-0.346	-0.346	
	$1b_2$	-0.487	-0.488	-0.488	
	$2a_1$	-0.898	-0.926	-0.927	
	$1a_1$	-17.935	-18.610	-18.620	
	E_{total}	-74.286	-75.912	-75.942	
C_6H_6	$1e_{1g}$	-0.249	-0.240	-0.240	
	$3e_{2g}$	-0.310	-0.305	-0.303	
	$1a_{2u}$	-0.347	-0.341	-0.340	
	$3e_{1u}$	-0.382	-0.379	-0.377	
	$1b_{2u}$	-0.397	-0.407	-0.404	
	$2b_{1u}$	-0.415	-0.411	-0.410	
	$3a_{1g}$	-0.481	-0.478	-0.477	
	$2e_{2g}$	-0.531	-0.545	-0.543	
	$2e_{1u}$	-0.643	-0.676	-0.673	
	$2a_{1g}$	-0.741	-0.778	-0.775	
	$1b_{1u}$	-9.152	-9.790	-9.796	
	$1e_{2g}$	-8.858	-9.790	-9.797	
	$1e_{1u}$	-9.151	-9.791	-9.797	
	$1a_{1g}$	-9.152	-9.791	-9.797	
	E_{total}	-218.656	-230.177	-230.211	

time, the VFD grid parameters used for N_2 produce N_{total}=592,532 and the maximum radius becomes 150 a.u. Therefore, VFD utilizes about 7 times less grids covering 15^3 times larger computational spaces than FD. Note that the proposed VFD method is the first-order scheme in the sense that it considers only nearest natural neighboring grids, while FD used here is the fourth-order scheme. Nonetheless, the numerical accuracy and efficiency of VFD are superior to ones of FD, mainly due to the benefit of the highly adaptive multicenter molecular grids.

Next, we present self-interaction-free DFT results showing considerable improvement on the electronic structure of atoms and molecules. Analogue to Koopmans' theorem [144] for the Hartree–Fock approximation, orbital energies from the Kohn–Sham equation in Eq. (2.33) are comparable to the experimental vertical ionization potentials when the self-interaction-correction term is taken into account [145, 146]. We present orbital binding energies ($-\varepsilon$) of a couple of diatomic molecules in Table 2.6, several small polyatomic molecules in Table 2.7, and benzene in Table 2.8, calculated by the VFD method with the LSDA and LBα potentials, in comparison with experiments. In Tables 2.6–2.8, we use the unit of electron volts for better comparison with experiments. The computational parameters in VFD are N_r=300, L=0.5 a.u., r_{max}=20 a.u., and l_{max}=25 with the Womersley scheme for all molecular cases, except N_r=200 for the benzene case. For the LBα parameters, we use α=1.19 and β=0.01 for all cases.

For N_2 and F_2 in Table 2.6, we compare the VFD values with the GPS results, which provides machine accuracy for atoms and diatomic molecules [67]. The LBα valence orbital energies by VFD are almost exactly matched with the GPS values [147], again ensuring the numerical accuracy of the VFD method.

Table 2.6: Orbital binding energies (in eV) of diatomic molecules computed by the VFD method with LSDA and LBα potentials in comparison with the GPS method and experimental (EXP) vertical ionization potentials.

		LSDA	LBα		
Molecule	Orbital	VFD	VFD	GPS [147]	EXP [Ref.]
N_2	$3\sigma_g$	10.4	15.5	15.5	15.5 [148]
	$1\pi_u$	11.9	16.9	16.9	16.8 [148]
	$2\sigma_u$	13.5	18.5	18.5	18.6 [148]
	$2\sigma_g$	28.2	33.0		37.3 [148]
	$1\sigma_u$	380.1	402.8		409.9 [148]
	$1\sigma_g$	380.2	402.8		409.9 [148]
F_2	$1\pi_g$	9.7	16.0	16.0	15.9 [149]
	$1\pi_u$	13.1	19.3	19.2	18.8 [149]
	$3\sigma_g$	15.8	21.9	21.9	21.1 [149]
	$2\sigma_u$	27.5	33.8		
	$2\sigma_g$	33.9	39.9		
	$1\sigma_u$	659.1	686.7		
	$1\sigma_g$	659.1	686.7		

For all molecular cases in Tables 2.6–2.8, the LBα values are comparable with experimental vertical ionization potentials [148, 149, 150, 151, 152, 153, 154, 155, 156]. LBα valence orbital energies computed by VFD are close to experimental values. For HOMO of N_2, F_2, H_2O, NH_3, and CH_4, the difference of the LBα energy and the experimental value is less than 0.3 eV. For HOMO of CO_2 and C_6H_6, the difference is 0.9 and 1.4 eV, respectively. Note that conventional LSDA functional without the self-interaction correction cannot describe electronic structure and ionization potential correctly. In other words, LSDA valence orbital energies are too weakly bound for all molecules.

Table 2.7: Orbital binding energies (in eV) of polyatomic molecules computed by the VFD method with LSDA and LBα potentials in comparison with experimental (EXP) vertical ionization potentials.

Molecule	Orbital	LSDA	LBα	EXP [Ref.]
CO_2	$1\pi_g$	9.4	14.7	13.8 [150]
	$1\pi_u$	13.0	18.2	17.6 [150]
	$3\sigma_u$	12.8	18.2	18.1 [150]
	$4\sigma_g$	13.8	19.2	19.4 [150]
	$2\sigma_u$	28.1	33.3	36.9 [151]
	$3\sigma_g$	29.1	34.2	38.0 [151]
	$2\sigma_g$	271.1	291.7	297.5 [148]
	$1\sigma_u$	508.9	533.7	540.8 [148]
	$1\sigma_g$	508.9	533.7	540.8 [148]
H_2O	$1b_1$	7.4	12.5	12.6 [152]
	$3a_1$	9.4	14.5	14.8 [152]
	$1b_2$	13.3	18.2	18.7 [152]
	$2a_1$	25.2	30.1	32.4 [152]
	$1a_1$	506.6	531.0	539.7 [148]
NH_3	$3a_1$	6.3	10.9	10.8 [153]
	$1e$	11.4	15.9	16.0 [153]
	$2a_1$	21.1	25.6	27.7 [153]
	$1a_1$	376.7	398.7	405.6 [148]
CH_4	$1t_2$	9.5	13.9	13.6 [154]
	$2a_1$	17.0	21.3	22.9 [154]
	$1a_1$	265.6	285.4	290.7 [148]

Table 2.8: Orbital binding energies (in eV) of benzene computed by the VFD method with LSDA and LBα potentials in comparison with experimental (EXP) vertical ionization potentials.

Molecule	Orbital	LSDA	LBα	EXP [Ref.]
C_6H_6	$1e_{1g}$	6.7	10.9	9.5 [155]
	$3e_{2g}$	8.3	12.6	11.7 [155]
	$1a_{2u}$	9.4	13.5	12.3 [155]
	$3e_{1u}$	10.3	14.6	14.0 [155]
	$1b_{2u}$	11.1	15.2	14.8 [155]
	$2b_{1u}$	11.2	15.6	15.8 [155]
	$3a_{1g}$	13.0	17.2	17.0 [155]
	$2e_{2g}$	14.9	19.0	
	$2e_{1u}$	18.4	22.5	
	$2a_{1g}$	21.2	25.2	
	C $1s$	266.6	286.3	284.9 [156]

2.7 Extension to the high-order scheme

Development of the VFD method in Section 2.2 is regarded as the first-order scheme in the sense that it considers only nearest natural neighboring grids. In the conventional finite difference (FD) method, numerical accuracy can be improved by including next grid points in the FD stencil. Fornberg and Sloan [157] and Fornberg [158] showed that increasing-order FD method in 1D becomes close toward the pseudospectral method when all grids are globally included in the stencil and its grid distribution is matched to the same distribution in the pseudospectral method. Analogue to the conventional FD method, we will show that numerical accuracy of the VFD method can be systematically improved by including further neighboring grids in the numerical scheme, i.e., neighbors of neighbors, neighbors of neighbors of neighbors, and so on. In this section, we analyze the numerical accuracy of VFD by the Taylor expansion,

and develop the high-order VFD scheme of the Laplacian operator by including further neighboring grids.

We start from the Laplacian definition in the integral form in Eq. (2.6),

$$\boldsymbol{\nabla}^2\varphi = \lim_{\int_V dV \to 0} \frac{\int_S \boldsymbol{\nabla}\varphi \cdot \mathbf{n}\, dS}{\int_V dV}. \tag{2.53}$$

Let v be a volume of space computed by the volume integral and $f(v)$ be the surface integral as a function of v,

$$v = \int_V dV \quad \text{and} \quad f(v) = \int_S \boldsymbol{\nabla}\varphi \cdot \mathbf{n}\, dS. \tag{2.54}$$

Trivially, $f(0) = 0$. Then, the Laplacian is alternatively expressed by the first derivative of $f(v)$ with respect to v at $v = 0$,

$$\boldsymbol{\nabla}^2\varphi = \lim_{v \to 0} \frac{f(v) - f(0)}{v - 0} = f'(0). \tag{2.55}$$

To compute the first derivative $f'(0)$ with truncation errors, one employs the Taylor expansion near $v = 0$,

$$f(v) = f(0) + vf'(0) + \frac{v^2}{2!}f''(0) + \frac{v^3}{3!}f^{(3)}(0) + \cdots. \tag{2.56}$$

Note that error analysis in the conventional FD usually makes use of a grid spacing, whereas this approach utilizes the Taylor expansion with respect to a grid volume that surely includes information of adjacent neighboring grids. From the Taylor expansion in Eq. (2.56), $f'(0)$ can be expressed by higher-order

terms with truncation errors,

$$
\begin{aligned}
f'(0) &= \frac{1}{v}\left[f(v) + O(v^2)\right] && \text{: 1st-order} && (2.57a)\\
&= \frac{1}{v}\left[f(v) - \frac{v^2}{2!}f''(0) + O(v^3)\right] && \text{: 2nd-order} && (2.57b)\\
&= \frac{1}{v}\left[f(v) - \frac{v^2}{2!}f''(0) - \frac{v^3}{3!}f^{(3)}(0) + O(v^4)\right] && \text{: 3rd-order} && (2.57c)\\
&\;\;\vdots \\
&= \frac{1}{v}\left[f(v) - \sum_{k=2}^{n}\frac{v^k}{k!}f^{(k)}(0) + O(v^{n+1})\right]. && \text{: } n\text{th-order} && (2.57d)
\end{aligned}
$$

To compute $f'(0)$ with high-order accuracy, one needs to evaluate the volume v, the surface integral $f(v)$ and high-order derivatives $f^{(k)}(0)$.

After Voronoi discretization in Section 2.2.1, one can rewrite discretized quantities of v and $f(v)$ as follows. Let v_i be a discretized version of v, and $F(v_i)$ be a discretized version of $f(v)$ at $v = v_i$. From Eqs. (2.4), (2.8), and (2.9),

$$v_i = \frac{1}{6}\sum_{j\in n_i} h_{ij}s_{ij}, \tag{2.58}$$

$$F(v_i) = \sum_{j\in n_i}\frac{\varphi_j - \varphi_i}{h_{ij}}s_{ij}, \tag{2.59}$$

where n_i represents a set of natural neighbors of the ith grid, and $j \in n_i$ indicates that j is one of neighbors of the ith grid. Note that $F(v_i)$ requires the summation over nearest neighboring grids only. From the property of the surface integral, F has additivity property,

$$F(v_i + v_j) = F(v_i) + F(v_j), \tag{2.60}$$

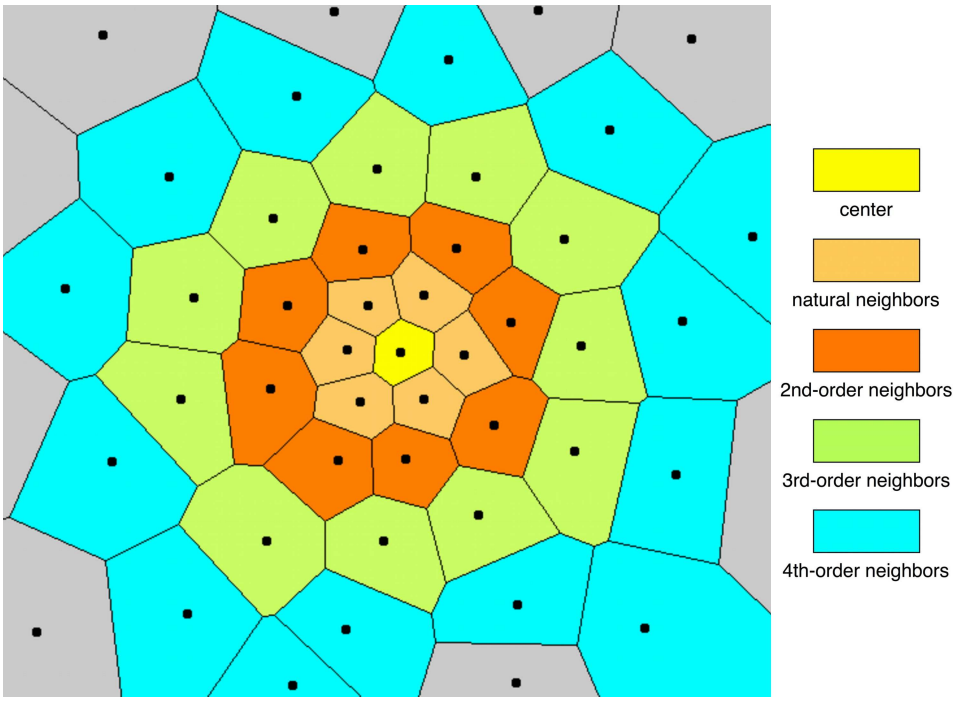

Figure 2.7: High-order neighbors on Voronoi diagram

where v_i and v_j do not overlap.

For convention, one can define sets of further outer neighbors (high-order neighbors) as

$$
\begin{aligned}
&n_i^{(1)}\text{: nearest natural neighbors of the } i\text{th grid } (= n_i) \\
&n_i^{(2)}\text{: outer neighbors of } n_i^{(1)};\ n_i^{(2)} = \{k : k \in n_j^{(1)} \text{ for } j \in n_i^{(1)}; k \neq i\} \\
&\qquad\qquad \vdots \\
&n_i^{(m)}\text{: outer neighbors of } n_i^{(m-1)};\ n_i^{(m)} = \{k : k \in n_j^{(1)} \text{ for } j \in n_i^{(m-1)}; k \notin n_i^{(m-2)}\}.
\end{aligned}
\tag{2.61}
$$

Here $n_i^{(2)}$ indicates non-duplicated outer neighbors of neighbors of the ith grid, and all high-order neighbors can be defined in this recursive way. Figure 2.7 displays these high-order neighbors around the ith grid (center). Then, mth-

order neighboring volume $v_i^{(m)}$ can be defined as,

$$v_i^{(m)} = \sum_{j \in n_i^{(m)}} v_j. \tag{2.62}$$

Also $V_i^{(m)}$ is defined as the total volume inside outer neighbors including outer neighbors themselves,

$$\begin{aligned} V_i^{(1)} &= v_i^{(1)} + v_i \\ V_i^{(2)} &= v_i^{(2)} + V_i^{(1)} \\ &\vdots \\ V_i^{(m)} &= v_i^{(m)} + V_i^{(m-1)}. \end{aligned} \tag{2.63}$$

Now, let us consider nth-order derivatives, $F^{(n)}(0)$. We can employ the simple finite difference scheme to compute derivatives and further neighbors to achieve the high-order derivatives. In other words, the first derivative is evaluated by the simple finite difference scheme,

$$F'(0) = \frac{F(v_i) - F(0)}{v_i - 0} = \frac{F(v_i)}{v_i}, \tag{2.64}$$

and then the second derivative is given by the derivative of the first-order derivative,

$$F''(0) = \frac{F'(v_i) - F'(0)}{v_i - 0}, \tag{2.65}$$

where $F'(0)$ is previously computed and $F'(v_i)$ will be evaluated with further neighbors using the additivity of F,

$$F'(v_i) = \frac{F(V_i^{(1)}) - F(v_i)}{V_i^{(1)} - v_i} = \frac{F(v_i^{(1)}) + F(v_i) - F(v_i)}{v_i^{(1)} + v_i - v_i} = \frac{F(v_i^{(1)})}{v_i^{(1)}}. \tag{2.66}$$

Thus, $F''(0)$ is finally evaluated by,

$$F''(0) = \frac{F(v_i^{(1)})}{v_i v_i^{(1)}} - \frac{F(v_i)}{v_i^2}, \tag{2.67}$$

where $F(v_i^{(1)})$ is easily computed by $F(v_i^{(1)}) = F(\sum_j v_j) = \sum_j F(v_j)$ where $j \in n_i^{(1)}$ using the additivity of F. In the general cases, these expressions yield a recursive equation with respect to two indexes, n and m.

$$\begin{aligned} F^{(n)}(V_i^{(m)}) &= \frac{F^{(n-1)}(V_i^{(m+1)}) - F^{(n-1)}(V_i^{(m)})}{V_i^{(m+1)} - V_i^{(m)}} \\ &= \frac{F^{(n-1)}(V_i^{(m+1)}) - F^{(n-1)}(V_i^{(m)})}{v_i^{(m+1)}} \quad (n \geq 1 \text{ and } m \geq -1). \end{aligned} \tag{2.68}$$

In the special cases, $V_i^{(0)} = v_i^{(0)} = v_i$ and $V_i^{(-1)} = 0$. Evaluation of the nth derivative at a given volume requires the $(n-1)$th derivative at both the same volume and further neighboring volume. After simplifying the recursive equation with respect to m,

$$F^{(n)}(V_i^{(m)}) = (-1)^{n+1} \frac{F(v_i^{(m+1)})}{(v_i^{(m+1)})^n} + \sum_{k=1}^{n-1} (-1)^{n-k+1} \frac{F^{(k)}(V_i^{(m+1)})}{(v_i^{(m+1)})^{n-k}}. \tag{2.69}$$

Especially, $F^{(n)}(0)$ is expressed by,

$$F^{(n)}(0) = \sum_{k=0}^{n-1} (-1)^{n-k+1} \frac{F^{(k)}(v_i)}{(v_i)^{n-k}}. \tag{2.70}$$

Using Eq. (2.69) and (2.70), $F^{(n)}(0)$ can be expressed with $F(v_i^{(m)})$ which is easily computable by the additivity of F. The solution has the following form,

$$F^{(n)}(0) = \sum_{k=0}^{n-1} \left[(-1)^{n-k+1} \frac{F(v_i^{(k)})}{\prod_{l=0}^{k} v_i^{(l)}} \left(\sum_{\substack{\alpha_0+\cdots+\alpha_l \\ =n-k-1 \\ \alpha_0,\alpha_1,\ldots,\alpha_l}} \frac{1}{(v_i^{(0)})^{\alpha_0} (v_i^{(1)})^{\alpha_1} \cdots (v_i^{(l)})^{\alpha_l}} \right) \right], \tag{2.71}$$

where $\alpha_0, \alpha_1, \ldots, \alpha_l$ are all integers ≥ 0. For instance, the 1st- to the 4th-order derivatives are expressed as follows,

$$F'(0) = \frac{F(v_i)}{v_i} \tag{2.72a}$$

$$F''(0) = -\frac{F(v_i)}{v_i^2} + \frac{F(v_i^{(1)})}{v_i v_i^{(1)}} \tag{2.72b}$$

$$F^{(3)}(0) = \frac{F(v_i)}{v_i^3} - \frac{1}{v_i v_i^{(1)}} \left(\frac{1}{v_i} + \frac{1}{v_i^{(1)}} \right) F(v_i^{(1)}) + \frac{F(v_i^{(2)})}{v_i v_i^{(1)} v_i^{(2)}} \tag{2.72c}$$

$$\begin{aligned} F^{(4)}(0) = &-\frac{F(v_i)}{v_i^4} + \frac{1}{v_i v_i^{(1)}} \left(\frac{1}{v_i^2} + \frac{1}{v_i v_i^{(1)}} + \frac{1}{(v_i^{(1)})^2} \right) F(v_i^{(1)}) \\ &+ \frac{1}{v_i v_i^{(1)} v_i^{(2)}} \left(\frac{1}{v_i} + \frac{1}{v_i^{(1)}} + \frac{1}{v_i^{(2)}} \right) F(v_i^{(2)}) + \frac{F(v_i^{(3)})}{v_i v_i^{(1)} v_i^{(2)} v_i^{(3)}}. \end{aligned} \tag{2.72d}$$

From the high-order expressions in Eq. (2.57) using discretized evaluations of the high-order derivatives and further natural neighbors in Eq. (2.71), one can compute the Laplacian at the ith grid with the high-order precision. The first-

order VFD scheme yields

$$\left(\nabla^2\varphi\right)_i = \frac{1}{v_i}\sum_{j\in n_i^{(1)}}\frac{\varphi_j-\varphi_i}{h_{ij}}s_{ij}, \tag{2.73}$$

which is reduced to Eq. (2.10). The second-order VFD expression is

$$\left(\nabla^2\varphi\right)_i = \left[1+\frac{1}{2!}\right]\frac{1}{v_i}\sum_{j\in n_i^{(1)}}\frac{\varphi_j-\varphi_i}{h_{ij}}s_{ij} - \frac{1}{2!}\frac{1}{v_i^{(1)}}\sum_{j\in n_i^{(1)}}\sum_{k\in n_j^{(1)}}\frac{\varphi_k-\varphi_j}{h_{jk}}s_{jk}. \tag{2.74}$$

The third-order VFD is

$$\begin{aligned}\left(\nabla^2\varphi\right)_i = &\left[1+\frac{1}{2!}-\frac{1}{3!}\right]\frac{1}{v_i}\sum_{j\in n_i^{(1)}}\frac{\varphi_j-\varphi_i}{h_{ij}}s_{ij}\\ &+\left[-\frac{1}{2!}+\frac{1}{3!}\left(1+\frac{v_i}{v_i^{(1)}}\right)\right]\frac{1}{v_i^{(1)}}\sum_{j\in n_i^{(1)}}\sum_{k\in n_j^{(1)}}\frac{\varphi_k-\varphi_j}{h_{jk}}s_{jk}\\ &-\frac{1}{3!}\frac{v_i}{v_i^{(1)}}\frac{1}{v_i^{(2)}}\sum_{j\in n_i^{(2)}}\sum_{k\in n_j^{(1)}}\frac{\varphi_k-\varphi_j}{h_{jk}}s_{jk}.\end{aligned} \tag{2.75}$$

The fourth-order VFD is

$$\begin{aligned}\left(\nabla^2\varphi\right)_i = &\left[1+\frac{1}{2!}-\frac{1}{3!}+\frac{1}{4!}\right]\frac{1}{v_i}\sum_{j\in n_i^{(1)}}\frac{\varphi_j-\varphi_i}{h_{ij}}s_{ij}\\ &+\left[-\frac{1}{2!}+\frac{1}{3!}\left(1+\frac{v_i}{v_i^{(1)}}\right)-\frac{1}{4!}\left(1+\frac{v_i}{v_i^{(1)}}+\frac{v_i^2}{(v_i^{(1)})^2}\right)\right]\frac{1}{v_i^{(1)}}\sum_{j\in n_i^{(1)}}\sum_{k\in n_j^{(1)}}\frac{\varphi_k-\varphi_j}{h_{jk}}s_{jk}\\ &+\left[-\frac{1}{3!}\frac{v_i}{v_i^{(1)}}+\frac{1}{4!}\left(\frac{v_i}{v_i^{(1)}}+\frac{v_i^2}{(v_i^{(1)})^2}+\frac{v_i^2}{v_i^{(1)}v_i^{(2)}}\right)\right]\frac{1}{v_i^{(2)}}\sum_{j\in n_i^{(2)}}\sum_{k\in n_j^{(1)}}\frac{\varphi_k-\varphi_j}{h_{jk}}s_{jk}\\ &-\frac{1}{4!}\frac{v_i^2}{v_i^{(1)}v_i^{(2)}}\frac{1}{v_i^{(3)}}\sum_{j\in n_i^{(3)}}\sum_{k\in n_j^{(1)}}\frac{\varphi_k-\varphi_j}{h_{jk}}s_{jk}.\end{aligned} \tag{2.76}$$

The high-order VFD formulation throughout Eqs. (2.73)–(2.76) provides an explicit expression for all grid points. It includes evaluations of the neighboring volumes and the surface integral for nearest neighboring grids as well as finding further high-order neighbors. The high-order neighbors are determined by the recursive manner of finding nearest neighbors. Thus, it is worthwhile to note that the VFD method is systematically improvable by recursive self-enhancement.

We first perform the electronic structure calculations of H_2^+ by means of the high-order VFD method on multicenter molecular grids in Section 2.2.5. Figuires 2.8(a) and (b) shows errors δ of the ground-state energies of H_2^+ as a function of N_r and $l_{\max}$, respectively. For VFD computational parameters, $l_{\max}$=15 is fixed for Fig. 2.8(a) and N_r=50 is fixed for Fig. 2.8(b). The mapping parameter is L=1 for both cases and the Lebedev scheme is used for the angular grid distribution. The high-order schemes remarkably improve convergency with respect to both radial grids and angular grids. For instances, the number of grid points to be required for convergence up to the third decimal place, i.e., $|\delta| < 5 \times 10^{-4}$ a.u., is dramatically reduced as the higher-order scheme is used:

(i) 1st-order VFD: $N_r \geq 150$ and $l_{\max} \geq 29 \rightarrow N_{\text{tot}}$=293,932

(ii) 2nd-order VFD: $N_r \geq 60$ and $l_{\max} \geq 15 \rightarrow N_{\text{tot}}$=34,146

(iii) 3rd-order VFD: $N_r \geq 30$ and $l_{\max} \geq 12 \rightarrow N_{\text{tot}}$=11,236

(iv) 4th-order VFD: $N_r \geq 25$ and $l_{\max} \geq 10 \rightarrow N_{\text{tot}}$=6,879

Although the proposed high-order scheme is very promising for solving the Schrödinger equation, there exist several limitations, especially to be extended for DFT and TDDFT calculations. First, error analysis for each high-

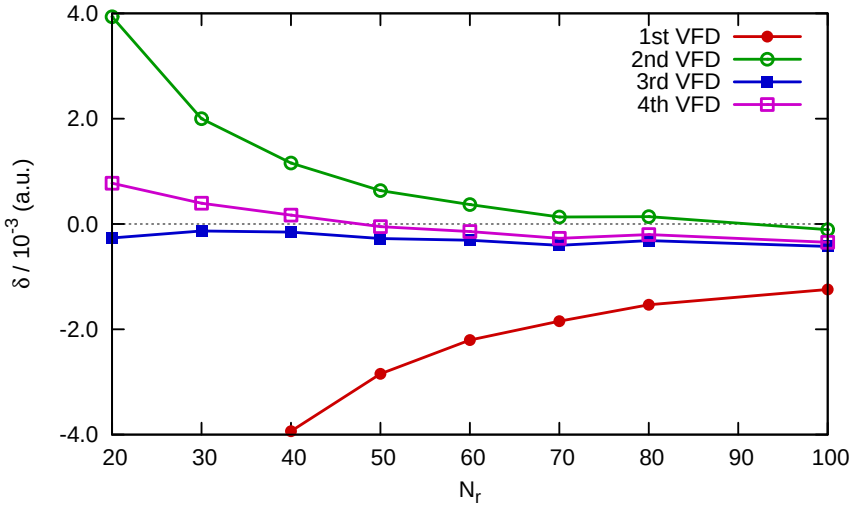

(a) Convergence as N_r increases ($l_{\max}$=15)

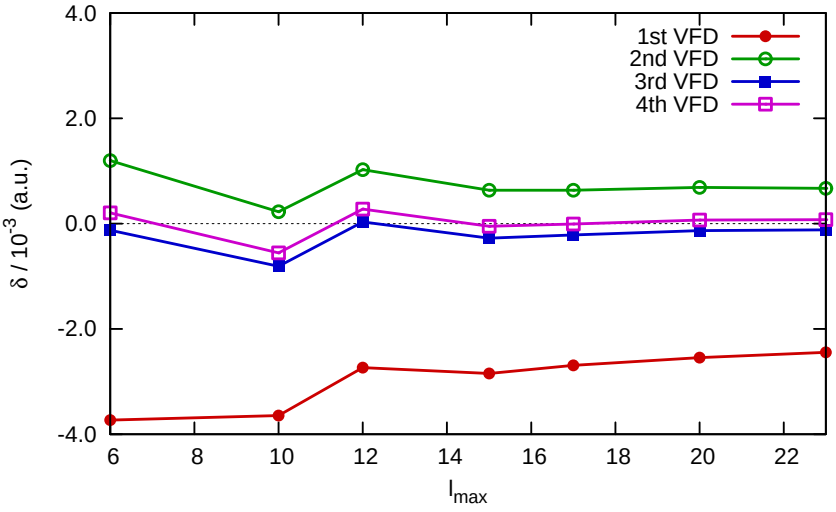

(b) Convergence as $l_{\max}$ increases (N_r=50)

Figure 2.8: Accuracy on the ground-state energies of H_2^+ computed by high-order VFD.

order derivative needs to be examined. Second, the Laplacian matrix is not symmetric any more. Third, the scheme is not accompanied by high-order accuracy integration. In Section 2.2.3, we have seen that the symmetrization is done with the weight matrix used in integration. In the first-order scheme, it was only the diagonal Voronoi volume matrix. In this manner, we expect there is a close connection between high-order integration and symmetrization. For wide applications of the high-order VFD scheme, these points need to be further investigated.

Chapter 3

Time-dependent Voronoi-cell finite difference method for probing multiphoton electron dynamics of polyatomic molecules

We first develop a new grid-based time-dependent method to investigate strong-field multiphoton processes of polyatomic molecules in intense ultrashort laser fields. The electronic structure of polyatomic molecules is treated by the density-functional theory (DFT) with proper long-range potential and the Kohn–Sham equation is accurately solved by means of the Voronoi-cell finite difference method on nonuniform and highly adaptive multicenter molecular grids. This method is generalized to the time-dependent problems with the split-operator time-propagation technique in the energy representation, allowing accurate and efficient non-perturbative treatment of attosecond electronic dynamics in strong fields. The new procedure is applied to the study of multiphoton ionization (MPI), photoelectron angular distribution (PAD), and high-order harmonic generation (HHG) of several polyatomic molecules in intense linearly-polarized and ultrashort laser fields with arbitrary field–molecule orientation.

Our results demonstrate the importance of the symmetries and dynamics of all contributing molecular orbitals, not only the highest-occupied molecular orbital (HOMO) but also inner valence orbitals. This feature suggests a new way to selectively probe individual orbitals in strong-field electronic dynamics.

3.1 Molecules in strong laser fields: molecular alignment and multielectron effects

The study of molecules in intense laser fields is a subject of much current significance in atomic, molecular, and optical physics [29]. Recent advances of laser technology enable us to align ensembles of molecules periodically by creating a coherent superposition of rotational states [159, 160]. This laser-induced molecular alignment capability has significant impact on strong-field molecular physics, leading to impressive applications such as tomographic imaging of molecular orbitals [25], quantum interference [161] and multiple orbital contribution [162] in high harmonic generation (HHG), and time-resolved photoelectron angular distribution (PAD) [163]. It also has been possible to measure multiphoton ionization (MPI) [164, 165], HHG [166], and PAD [167] as a function of the angle between the polarization of linearly-polarized laser field and the orientation of aligned linear molecules. In particular, the field–molecule orientation dependence of MPI has attracted much attention because not only the ionization mechanism plays a fundamental role in strong-field processes but also the molecular alignment may offer additional degree of freedom to control molecular processes. Also the orientation-resolved HHG of aligned molecules has attracted much current interests related to molecular imaging [26], which

allows for probing the electronic structures and dynamics, for example, the tomographic picture of molecular orbitals [25].

Most of the recent theoretical studies of MPI are based on approximated models such as the molecular Ammosov–Delone–Krainov (ADK) [168] and Keldysh–Faisal–Reiss [169] models, which usually consider only the highest-occupied molecular orbital (HOMO) contribution and neglect the multielectron dynamics from multiple orbitals. However, there have been several recent experimental studies showing significant discrepancies between experimental observations and approximated models, for examples, the non-suppression of F_2 MPI [170, 171] and the orientation dependence of CO_2 MPI [164, 165], etc. More recently, the importance of contribution to HHG and MPI from the inner orbital just below HOMO has been experimentally demonstrated in N_2 [162], N_2O_4 [172], and CO_2 [173] which cannot be explained by the approximated models. Thus, it is an important and timely task to develop more comprehensive and accurate theoretical description of strong-field electronic dynamics including electron correlation and multielectron responses. Along this direction, we note that the self-interaction-free time-dependent density-functional theory (TDDFT) has been recently developed and successfully applied to a number of studies of atomic and diatomic molecular processes in intense laser fields [49, 147, 174, 175, 176], with results in good agreement with experiments. Here we present TDDFT studies of polyatomic molecular processes in intense laser fields for the first time by new development of a grid-based time-dependent method.

3.2 Time-dependent Voronoi-cell finite difference method

We develop a time-dependent Voronoi-cell finite difference (TDVFD) method as an extension of VFD to the time domain, incorporating with the second-order split-operator technique in the energy representation [41, 50]. Let us consider the time-dependent Schrödinger equation with a time-dependent potential $u(\mathbf{r}, t)$,

$$i\frac{\partial}{\partial t}\psi(\mathbf{r}, t) = \hat{H}(\mathbf{r}, t)\psi(\mathbf{r}, t), \tag{3.1}$$

where $\hat{H}(\mathbf{r}, t) = -\frac{1}{2}\boldsymbol{\nabla}^2 + u(\mathbf{r}, t)$. For a numerical time-propagation of Eq. (3.1), $\hat{H}(\mathbf{r}, t)$ can be split into two parts as

$$\hat{H}(\mathbf{r}, t) = \hat{H}_0(\mathbf{r}) + \hat{U}(\mathbf{r}, t), \tag{3.2}$$

where

$$\hat{H}_0(\mathbf{r}) = -\frac{1}{2}\boldsymbol{\nabla}^2 + u(\mathbf{r}, 0), \tag{3.3}$$

$$\hat{U}(\mathbf{r}, t) = u(\mathbf{r}, t) - u(\mathbf{r}, 0). \tag{3.4}$$

The unperturbed Hamiltonian $\hat{H}_0(\mathbf{r})$ is accurately solved by the VFD method and the time-dependent potential $\hat{U}(\mathbf{r}, t)$ is simply given by a diagonal matrix evaluated at each grid in the VFD scheme. Since $\hat{H}_0(\mathbf{r})$ is already represented in 3D real space in VFD, there is no further sophistication needed regarding the molecular symmetry. Then the second-order split-operator technique for the time-propagation yields

$$\psi(t + \Delta t) = e^{-i\hat{U}(t)\frac{\Delta t}{2}} e^{-i\hat{H}_0\Delta t} e^{-i\hat{U}(t)\frac{\Delta t}{2}} \psi(t) + O(\Delta t^3), \tag{3.5}$$

where the coordinate $\mathbf{r}$ is not explicitly expressed for briefness.

In the matrix representation,

$$\mathbf{f}(t+\Delta t) \leftarrow e^{-i\mathbf{U}(t)\frac{\Delta t}{2}} e^{-i\mathbf{H}_0 \Delta t} e^{-i\mathbf{U}(t)\frac{\Delta t}{2}} \mathbf{f}(t), \tag{3.6}$$

where $\mathbf{f}(t)$ is a column vector of the time-dependent wavefunction represented in every grid,

$$\mathbf{f}(t) = (\cdots f_i(t) \cdots)^T; \quad f_i(t) = \psi(\mathbf{r}_i, t). \tag{3.7}$$

The exponential of the diagonal matrix is trivially obtained by exponentiating every entry on the main diagonal. Since $\mathbf{U}(t)$ is given by a diagonal matrix in VFD, $\exp[-i\mathbf{U}(t)\frac{\Delta t}{2}]$ is simply computable. For $\exp[-i\mathbf{H}_0\Delta t]$, one defines an evolution matrix $\mathbf{S}$ with the spectral decomposition of $\mathbf{H}_0 = \mathbf{C}\mathbf{E}\mathbf{C}^{-1}$ where $\mathbf{C}$ is the eigenvector matrix and $\mathbf{E}$ is the diagonal matrix of eigenvalues in Eq. (2.15),

$$\mathbf{S} = e^{-i\mathbf{H}_0\Delta t} = \mathbf{C} e^{-i\mathbf{E}\Delta t} \mathbf{C}^{-1}, \tag{3.8}$$

where $\exp[-i\mathbf{E}\Delta t]$ is easily computable with the eigenstate energies in the diagonal matrix $\mathbf{E}$.

For the symmetric Hamiltonian $\tilde{\mathbf{H}}_0$ in Eq. (2.20), the symmetric version is expressed by

$$\tilde{\mathbf{S}} = e^{-i\tilde{\mathbf{H}}_0\Delta t} = \tilde{\mathbf{C}} e^{-i\mathbf{E}\Delta t} \tilde{\mathbf{C}}^T, \tag{3.9}$$

and then the time-propagation is performed by

$$\tilde{\mathbf{f}}(t+\Delta t) = \mathbf{W}(t) \cdot \tilde{\mathbf{S}} \cdot \mathbf{W}(t) \cdot \tilde{\mathbf{f}}(t), \tag{3.10}$$

where $\tilde{\mathbf{f}} = \mathbf{V}^{\frac{1}{2}}\mathbf{f}$ and $\mathbf{W}(t) = \exp[-i\mathbf{U}(t)\frac{\Delta t}{2}]$. All operations here are the matrix–vector multiplication and even $\mathbf{W}(t)$ is a diagonal matrix. So, they can be optimized and parallelized with ease on modern computer architectures, for example, through optimized BLAS libraries [177] for a specific processor. The explicit expressions of the $\tilde{\mathbf{S}}$ elements are

$$\tilde{\mathbf{S}}: \ \tilde{S}_{ij} = \sum_k \tilde{C}_{ik}\tilde{C}_{jk}e^{-i\varepsilon_k \Delta t}, \tag{3.11}$$

where ε_k is the kth eigenstate energy and $\tilde{C}_{ik}$ is a value at the ith grid of the kth eigenvector of $\tilde{\mathbf{H}}$. We emphasize that this $\tilde{\mathbf{S}}$ is a time-independent complex symmetric matrix and it needs to be constructed only once before the time-propagation, which remarkably reduces the computation time.

This TDVFD scheme in the energy representation is different from the conventional split-operator techniques [178, 179] where $\hat{H}_0$ is usually chosen to be the kinetic energy operator solved by the fast Fourier transformation on the uniform grids. The advantages of using our proposed method are (i) highly adaptive molecular grids to solve $\hat{H}_0$ as described in Section 2.2.5, and (ii) elimination of the undesirable fast-oscillating high-energy components in the $\tilde{\mathbf{S}}$ matrix [41, 50]. Both features allow us to reduce the number of spatial grids and to speed up the time-propagation considerably. Furthermore, this scheme inherits unconditionally numerical stability and conservation of probability from the original split-operator technique due to the unitary evolution operator [178]. Thus it conserves the norm of the wavefunctions during the time-propagation (for example, errors of the norm are about 10^{-10} in the field-free case), ensuring the numerical accuracy of ionization probabilities computed from the norm of the wavefunctions in Section 3.3.

3.3 Application to time-dependent density-functional theory

We now consider the solution of a set of time-dependent Kohn–Sham equations for N-electron systems in the time-dependent density-functional theory (TDDFT) framework [180],

$$i\frac{\partial}{\partial t}\psi_{i\sigma}(\mathbf{r},t) = \left[-\frac{1}{2}\boldsymbol{\nabla}^2 + u_{\mathrm{eff},\sigma}(\mathbf{r},t)\right]\psi_{i\sigma}(\mathbf{r},t), \quad (i = 1,2,...,N_\sigma), \tag{3.12}$$

where the time-dependent effective potential is expressed by

$$u_{\mathrm{eff},\sigma}(\mathbf{r},t) = u_{\mathrm{ne}}(\mathbf{r}) + u_{\mathrm{h}}(\mathbf{r},t) + u_{\mathrm{xc},\sigma}(\mathbf{r},t) + \mathbf{F}(t)\cdot\mathbf{r}. \tag{3.13}$$

The time-dependent Hartree potential is

$$u_{\mathrm{h}}(\mathbf{r},t) = \int \frac{\rho(\mathbf{r}',t)}{|\mathbf{r}-\mathbf{r}'|}d\mathbf{r}', \tag{3.14}$$

and for the time-dependent exchange–correlation potential we use the adiabatic approximation [174] with the LBα potential in Eq. (2.45),

$$u_{\mathrm{xc},\sigma}(\mathbf{r},t) = u^{\mathrm{LB}\alpha}_{\mathrm{xc},\sigma}[\rho_\uparrow,\rho_\downarrow]\Big|_{\rho_\sigma=\rho_\sigma(\mathbf{r},t)}. \tag{3.15}$$

The correct long-range asymptotic behavior of the LBα potential is crucial for proper DFT treatment of molecular excited and continuum states in strong-field electronic dynamics [49, 147, 175, 176]. The last term $\mathbf{F}(t)\cdot\mathbf{r}$ is the interaction of an electron with a linearly-polarized external laser field.

To solve Eq. (3.12), we use the TDVFD method described in Section 3.2. In the split-operator technique, $\hat{H}_0(\mathbf{r})$ and $\hat{U}(\mathbf{r},t)$ are given by

$$\hat{H}_0(\mathbf{r}) = -\tfrac{1}{2}\boldsymbol{\nabla}^2 + u_{\mathrm{eff},\sigma}(\mathbf{r},0), \tag{3.16}$$

$$\hat{U}(\mathbf{r},t) = \mathbf{F}(t)\cdot\mathbf{r} + \left[u_{\mathrm{xc},\sigma}(\mathbf{r},t) - u_{\mathrm{xc},\sigma}(\mathbf{r},0)\right] + \left[u_{\mathrm{h}}(\mathbf{r},t) - u_{\mathrm{h}}(\mathbf{r},0)\right], \tag{3.17}$$

and the time-dependent wavefunction for each spin-orbital is propagated by Eq. (3.5). Through the TDDFT formulation solved by the TDVFD method, we can now explore strong-field electronic dynamics including all molecular spin-orbitals and continuum states.

From the TDDFT solutions, one can compute the time-dependent ionization probability of an individual spin-orbital by

$$P_{i\sigma}(t) = 1 - n_{i\sigma}(t), \tag{3.18}$$

where

$$n_{i\sigma}(t) = \langle\psi_{i\sigma}(\mathbf{r},t)|\psi_{i\sigma}(\mathbf{r},t)\rangle \tag{3.19}$$

is the population or survival probability of the spin-orbital, which is the norm of the time-dependent wavefunction decreasing as a function of t due to the absorber [41] to prevent spurious reflections at radial boundary and to filter out the ionized wave packet. The time-dependent total survival probability is given by multiplication of all spin-orbital survival probabilities,

$$n_{\mathrm{total}}(t) = \prod_{i\sigma} n_{i\sigma}(t) = \prod_{i\sigma}\left[1 - P_{i\sigma}(t)\right], \tag{3.20}$$

and the time-dependent total ionization probability is given by

$$P(t) = 1 - n_{\text{total}}(t). \tag{3.21}$$

Then, the total ionization probability P after one pulse (at $t = T$) can be calculated by

$$P = 1 - \prod_{i\sigma} \left[1 - P_{i\sigma}(T)\right]. \tag{3.22}$$

In the limit of small $P_{i\sigma}(T)$, Eq. (3.22) is reduced to the sum of individual ionization probabilities,

$$P \approx \sum_{i\sigma} P_{i\sigma}(T). \tag{3.23}$$

To calculate HHG spectra, one can compute the time-dependent dipole moment from the TDDFT solutions,

$$\mathbf{D}(t) = \sum_{i\sigma} \langle \psi_{i\sigma}(\mathbf{r}, t) | \mathbf{r} | \psi_{i\sigma}(\mathbf{r}, t) \rangle, \tag{3.24}$$

and then the spectral density $S(\omega)$ of the radiation energy emitted for all the time for the laser pulses is given by [67, 181]

$$S(\omega) = \frac{4\omega^4}{6\pi c^3} |\tilde{\mathbf{D}}(\omega)|^2, \tag{3.25}$$

where c is the velocity of light and $\tilde{\mathbf{D}}(\omega)$ is the Fourier transform of the time-dependent dipole moment,

$$\tilde{\mathbf{D}}(\omega) = \int_{\infty}^{\infty} \mathbf{D}(t) e^{-i\omega t} dt. \tag{3.26}$$

The plot of $S(\omega)$ as a function of ω forms the HHG spectrum.

3.4 Orientation dependence of multiphoton ionization of N_2

We perform TDDFT calculations of N_2 with arbitrary field–molecule orientation by means of the TDVFD method. The ground-state electronic configuration of N_2 is

$$[\text{core}](2\sigma_g)^2(2\sigma_u)^2(1\pi_u)^4(3\sigma_g)^2,$$

where [core] is $(1\sigma_g)^2(1\sigma_u)^2$ that corresponds to 1s orbitals of two N's. All orbitals except the core orbitals participate in the time-propagation.

For time-dependent solutions with the TDVFD method, the most time consuming part is Eq. (3.10), involving the matrix–vector multiplication. In the VFD and TDVFD schemes, the matrix size is identical to the total number of grid points. Table 3.1 shows LBα orbital binding energies of N_2 with smaller number of grids than one used in Table 2.6: N_r=80, L=2 a.u., r_{max}=40 a.u., and l_{max}=12 with the Womersley grids, corresponding to the total number of grids N_{total}=21,164. For the LBα parameters in this case, α=1.24 is used to obtain better agreement with experiments. One can see that the LBα orbital energies with a small number of grids still reproduce the electronic structure of N_2 in comparison with experimental vertical ionization potentials [148]. Based on this electronic structure with the matrix size of N_{total}=21,164, we are able to carry out time-dependent calculations within a reasonable computation time.

In order to examine electronic dynamics as a function of the angle between the polarization of the laser field and the orientation of aligned N_2, we define the orientation angle as shown in Fig. 3.1(a). Without loss of generality, we assume that the molecular axis coincides with the z-axis and the polarization

Table 3.1: Orbital binding energies (in eV) of N_2 computed by VFD with a small number of grids.

Orbital	VFD/LBα	EXP [Ref.]
$3\sigma_g$(HOMO)	15.5	15.5 [148]
$1\pi_u$(HOMO$-$1)	17.0	16.8 [148]
$2\sigma_u$(HOMO$-$2)	19.0	18.6 [148]
$2\sigma_g$	33.3	37.3 [148]
$1\sigma_u$	410.8	409.9 [148]
$1\sigma_g$	410.8	409.9 [148]

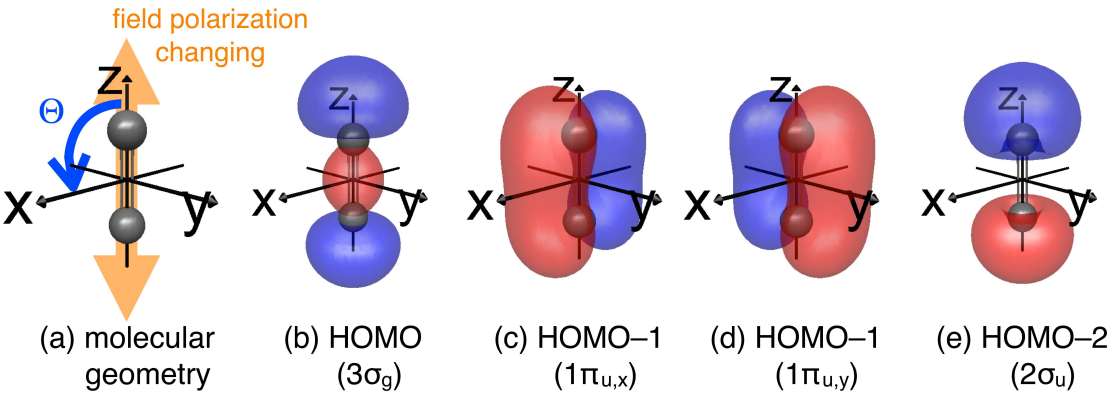

Figure 3.1: Molecular geometry and molecular orbital pictures of N_2. The principal axis is the z-axis and the molecular geometry is fixed. Two nitrogen atoms (gray ball) are located in the z-axis. The field polarization axis with respect to the principal axis changes toward the x-axis (Θ).

vector of the external field lies in the xz-plane, then $\mathbf{F}(t) \cdot \mathbf{r}$ is given by

$$\mathbf{F}(t) \cdot \mathbf{r} = F(t)(x \sin\Theta + z \cos\Theta), \tag{3.27}$$

where Θ is the orientation angle between the molecular axis and the field polarization axis.

For the sine-squared pulse envelope, we use

$$F(t) = F_0 \sin^2\left(\frac{\pi t}{T}\right) \sin\omega t, \tag{3.28}$$

where F_0 is the peak field amplitude, ω is the carrier frequency, and T is the pulse duration. During the time-propagation, we use the radial-based absorber function [41] as

$$w(r_c) = \cos^{\frac{1}{4}}\left[\frac{\pi(r_c - r_0)}{2(r_1 - r_0)}\right] \quad \text{for } r_0 \le r_c \le r_1, \tag{3.29}$$

where r_c is a radial distance from the closest nucleus. For laser parameters, we use ω=0.0556 a.u. corresponding to the wavelength 800 nm and T=20 optical cycles (o.c.). For computational parameters of time-dependent problems, we use r_0=15 a.u., r_1=25 a.u., and Δt=0.001 o.c. corresponding to 2.67 attoseconds. For an one-point calculation of N_{total}=21,164 and T=20 o.c. (20,000 time iterations in total), the computation time takes about 10.5 hours on the lab workstation equipped with two Intel Xeon X5355 (quad core, 2.66GHz) CPUs.

Figures 3.1(b)–(e) illustrate individual orbital pictures of N_2 obtained by GAMESS [132] and MACMOLPLT [182]. HOMO ($3\sigma_g$) and HOMO-2 ($2\sigma_u$) lie along with the z-axis and two degenerate HOMO-1 ($1\pi_{u,x}$ and $1\pi_{u,y}$) lie in the xz- and yz-planes. Energetically, the orbital of less ionization potential tends

to be more ionized. Thus HOMO is usually expected to be the most dominant portion in the total ionization probability. However, the ionization process is also related to the molecular orbital symmetry [67, 147, 183]. When the linearly-polarized laser field is applied to the z-axis (parallel, Θ=0°), HOMO and HOMO-2 can be more perturbed and ionized than other orbitals because the induced dipole change of σ-symmetry is preferable along with this field polarization parallel to the molecular axis [162]. On the other hand, when the field is applied to the x-axis (perpendicular, Θ=90°), HOMO-1 (only $1\pi_{u,x}$ in this case) symmetry is along with the field polarization. Therefore, we expect that the orientation dependence of MPI is reflected by individual orbital symmetries.

In Fig. 3.2, we plot the time-dependent electron population $n_{i\sigma}(t)$ of individual spin-orbitals of N_2 in the parallel [Figs. 3.2(a)–(c)] and perpendicular [Figs. 3.2(d)–(f)] cases. We use 20-optical-cycle $\sin^2$-envelope laser pulses with the wavelength 800 nm. The peak intensities are 10^{14} W/cm^2 in Figs. 3.2(a) and (d); 3×10^{14} W/cm^2 in Figs. 3.2(b) and (e); and 5×10^{14} W/cm^2 in Figs. 3.2(c) and (f). In the parallel case (Θ=0°), HOMO exhibits the most dominant contribution to the total ionization and HOMO-2 contribution is also increasing as the intensity increases. On the other hand, HOMO-1 contribution is increasing as the intensity increases in the perpendicular case (Θ=90°) due to the orbital symmetry of π_u. Note that HOMO contribution is still dominant in both cases.

Figure 3.3 shows the orientation dependence of ionization probabilities of N_2 with 800 nm and 2×10^{14} W/cm^2 as a function of the field–molecule orientation angle. Note that larger angular grids are used ($l_{\max}$=15) in calculations to plot individual orbital ionization probabilities in Fig. 3.3 because of a possible resonance between HOMO and HOMO-1. The total ionization

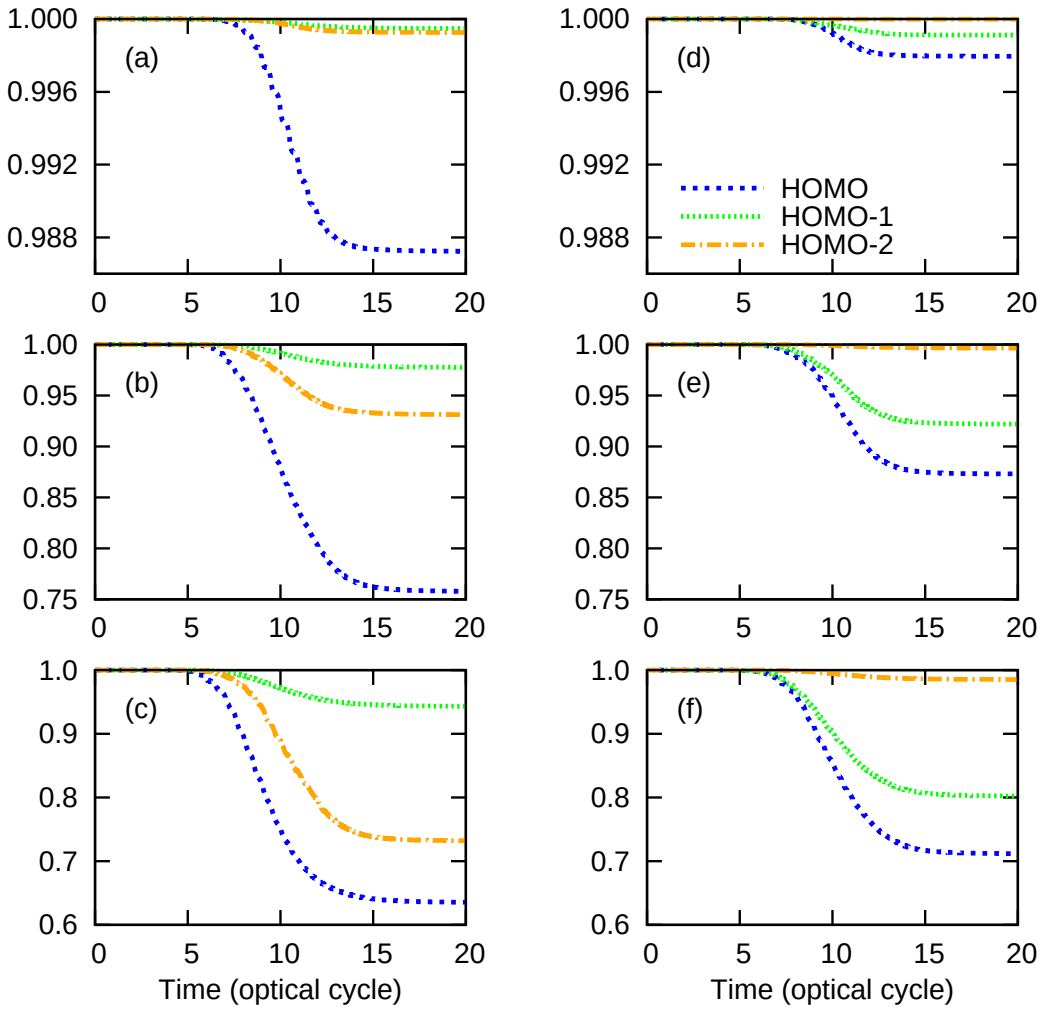

Figure 3.2: Plots of the time-dependent electron population $N_{i\sigma}(t)$ of individual spin-orbitals of N_2. The laser peak intensities are 10^{14} W/cm^2 in (a) and (d), 3×10^{14} W/cm^2 in (b) and (e), and 5×10^{14} W/cm^2 in (c) and (f). The field–molecule orientation angles are Θ=0° for (a)–(c) and Θ=90° for (d)–(f). The legend in (d) is for all plots.

probability in the polar plot (left panel) looks like a dumbbell shape in accord with experiments [164]. The ionization probabilities of individual orbitals (right panel) illustrates importance of multielectron effects between HOMO and HOMO-1. For Θ=15–40°, HOMO-1 contribution is larger than HOMO contribution. Thus, both HOMO and HOMO-1 contribute to this dumbbell shape of the orientation dependent plot of the total ionization probability. These comparable contributions from HOMO and HOMO-1 are explained by a small orbital energy difference and a strong coupling between HOMO and HOMO-1. In Table 3.1, calculated difference between HOMO and HOMO-1 is only 1.5 eV, which is relatively small in comparison with other molecules in Tables 2.6 and 2.7. Moreover, this energy gap is very close to the photon energy (1.55 eV) corresponding to the carrier wavelength of 800 nm. A transition between HOMO ($3\sigma_g$) and HOMO-1 ($1\pi_u$) is forbidden in the parallel case (Θ=0°) but allowed in other angles, so it leads to a possible one-photon resonance between HOMO and HOMO-1. This phenomenon is also theoretically predicted in MPI and HHG of N_2 in the 800 nm laser field [184].

Next, we consider effects of laser intensity on the orientation dependent patterns in Fig. 3.4. The peak intensity of laser pulses is varying from 10^{14} to 5×10^{14} W/cm^2, and the wavelength is fixed at 800 nm. All data sets are normalized to their maximum value. As the intensity increases, the polar plot becomes less anisotropic [147] because at higher intensity all orbitals participate in the ionization process, thus losing a characteristic pattern of each orbital.

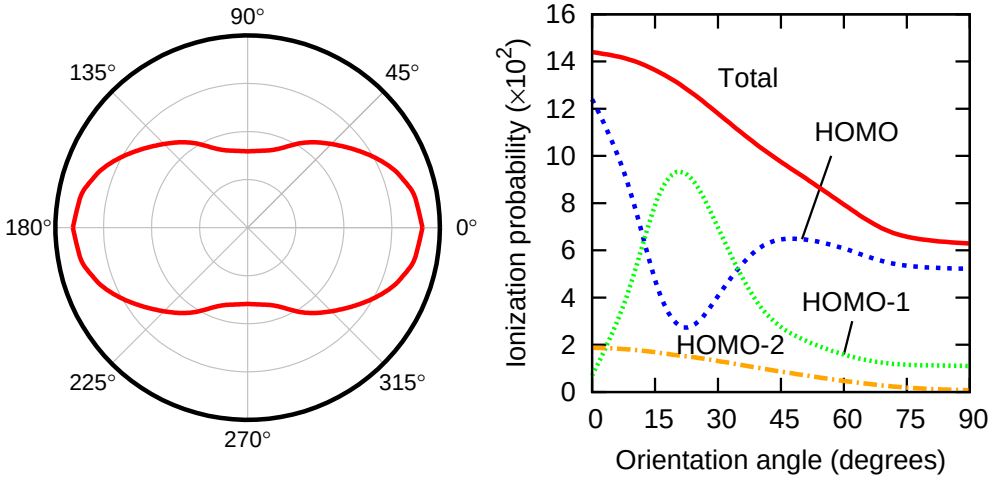

Figure 3.3: Orientation dependence of total ionization probability (left panel) and individual ionization probability of multiple orbitals (right panel) of N_2 with 800 nm and 2×10^{14} W/cm^2.

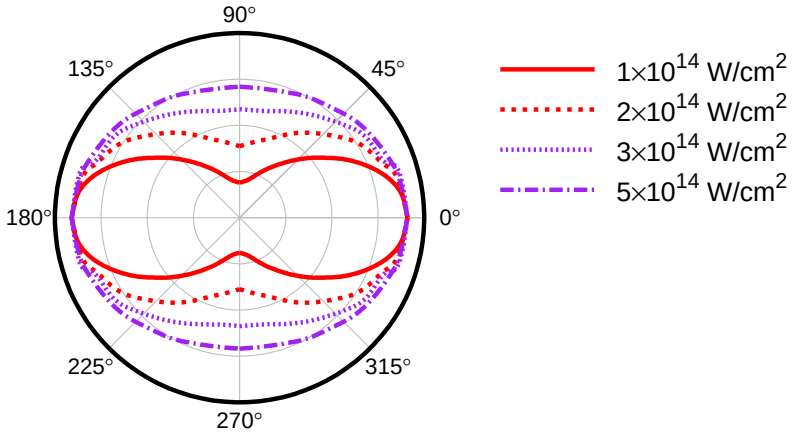

Figure 3.4: Effects of laser intensity on the orientation dependence of total ionization probability of N_2.

3.5 Orientation dependence of multiphoton ionization of H_2O

We perform TDDFT calculations of H_2O with arbitrary field–molecule orientation by means of the TDVFD method. The ground-state electronic configuration of H_2O is

$$[\text{core}](2a_1)^2(1b_2)^2(3a_1)^2(1b_1)^2,$$

where [core] is $(1a_1)^2$ that corresponds to O 1s orbital. All orbitals except the core orbital participate in the time-propagation. Table 3.2 lists LBα orbital binding energies with a small number of grids in comparison with experiments [148, 152] and α=1.21 is used to compensate for inaccuracy in orbital energies. The grid parameters are N_r=80, L=2 a.u., $r_{\max}$=40 a.u., and $l_{\max}$=10 with the Womersley grids, which provide N_{total}=20,022 for the triatomic H_2O molecule. For the time-propagation with N_{total}=20,022 and 20,000 time iterations, the computation time is about 9 hours on the same workstation mentioned in Section 3.4.

Figure 3.5 depicts orbital pictures of H_2O with the molecular geometry. The principal axis is the z-axis and the molecular geometry is fixed. All atoms of H_2O are contained in the yz-plane. HOMO ($1b_1$), HOMO-1 ($3a_1$), and HOMO-2 ($1b_2$) have atomic p-orbital-like characters along with the x-, z-, and

Table 3.2: Orbital binding energies (in eV) of H_2O computed by VFD with a small number of grids.

Orbital	VFD/LBα	EXP [Ref.]
$1b_1$(HOMO)	12.6	12.6 [152]
$3a_1$(HOMO-1)	14.6	14.8 [152]
$1b_2$(HOMO-2)	18.2	18.7 [152]
$2a_1$	30.5	32.4 [152]
$1a_1$	540.5	539.7 [148]

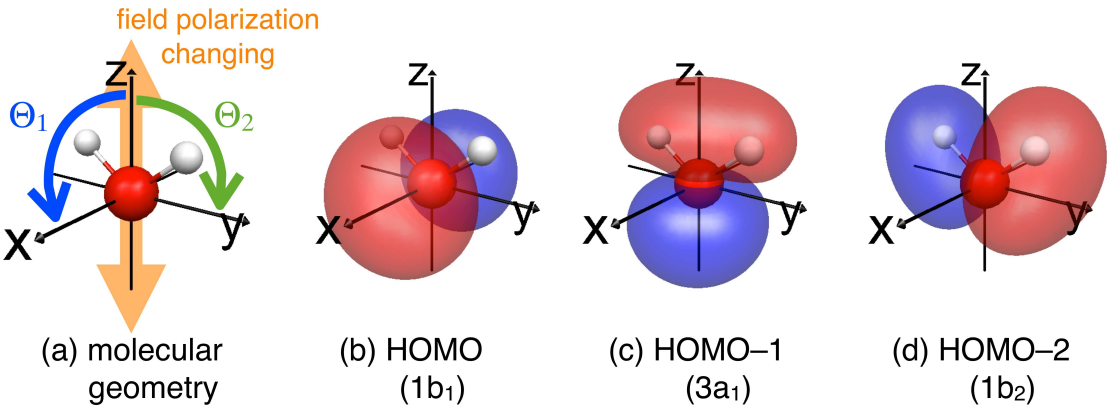

Figure 3.5: Molecular geometry and molecular orbital pictures of H_2O. The principal axis is the z-axis and the molecular geometry is fixed. An oxygen atom (red ball) and two hydrogen atoms (white ball) are contained in the yz-plane. The field polarization axis with respect to the principal axis changes toward the x-axis (Θ_1) or the y-axis (Θ_2).

y-axis, respectively. With respect to the fixed molecular frame of H_2O, the field polarization direction can change in two different ways as shown in Fig. 3.5(a). First, the angle changes from the z-axis toward the x-axis (denoted by Θ_1). The interaction between the electron and the field is given by

$$\mathbf{F}(t) \cdot \mathbf{r} = F(t)(x \sin\Theta_1 + z \cos\Theta_1). \tag{3.30}$$

Second, the angle changes from the z-axis toward the y-axis (denoted by Θ_2). Then,

$$\mathbf{F}(t) \cdot \mathbf{r} = F(t)(y \sin\Theta_2 + z \cos\Theta_2). \tag{3.31}$$

According to orbital pictures in Figs. 3.5(b)–(d), there is no orientation dependence when the field polarization varies within the nodal plane of each orbital, while the orientation dependence maximizes when the field polarization approaches the p-orbital-like polarization of each orbital. In other words, incre-

ment of Θ_1 triggers to maximize HOMO ionization, to minimize HOMO$-$1 ionization, and no effects on HOMO$-$2 ionization. On the other hand, increment of Θ_2 causes no effects on HOMO ionization, to minimize HOMO$-$1 ionization, and to maximize HOMO$-$2 ionization. Consequently, it provides feasibility to selectively probe the MPI processes of individual orbitals in aligned H_2O.

Figure 3.6 shows the orientation dependence of total ionization probability of H_2O with 800 nm and 5×10^{13} W/cm^2 as a function of (a) Θ_1 and (b) Θ_2. The pulse shape is sin^2-envelope with the 20-o.c. pulse length. When Θ_1 changes, the orientation dependence of total ionization probability mostly follows the pattern of HOMO as shown in Fig. 3.6(a). On the other side, the appearance of the orientation dependence is dramatically changed when Θ_2 changes. Since HOMO has the nodal plane of the yz-plane, the change of Θ_2 in the yz-plane does not affect HOMO ionization. Thus the overall pattern of the orientation dependence of total ionization probability is dominantly determined by HOMO$-$1 as shown in Fig. 3.6(b). To our knowledge, this is the first prediction of the dominant contribution from HOMO$-$1 to the overall orientation dependent pattern of MPI.

3.6 Orientation dependence of multiphoton ionization of CO_2

We perform TDDFT calculations of CO_2 with arbitrary field–molecule orientation by means of the TDVFD method. The ground-state electronic configuration of CO_2 is

$$[\text{core}](3\sigma_g)^2(2\sigma_u)^2(4\sigma_g)^2(3\sigma_u)^2(1\pi_u)^4(1\pi_g)^4,$$

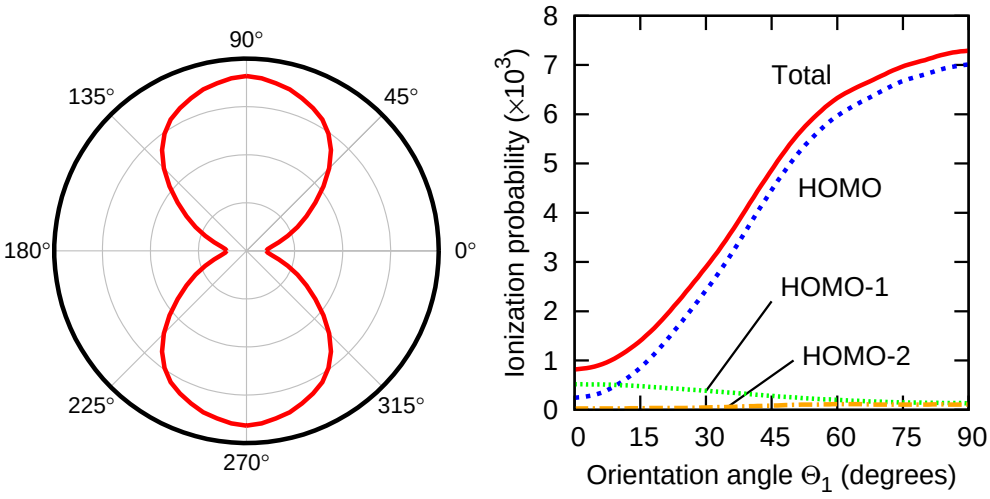

(a) Orientation changes of Θ_1

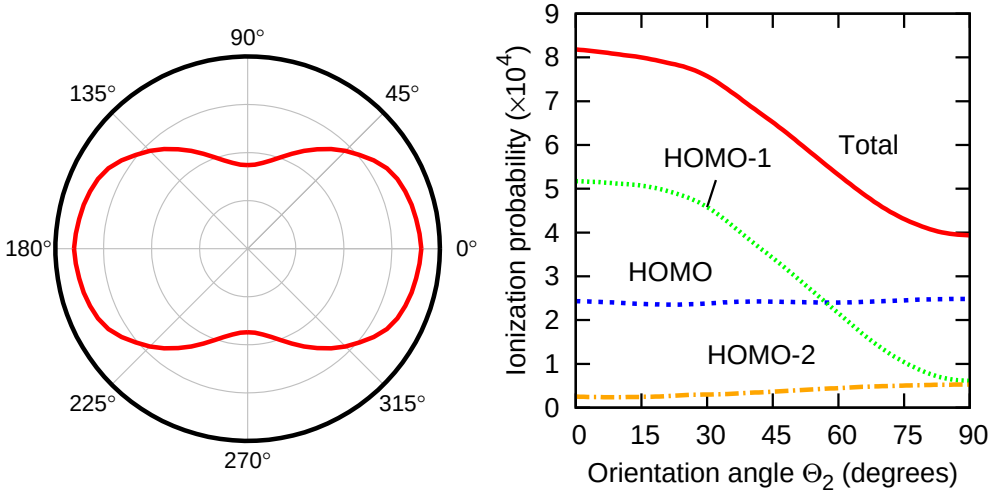

(b) Orientation changes of Θ_2

Figure 3.6: Orientation dependence of total ionization probability (left panel) and individual ionization probability of multiple orbitals (right panel) of H_2O with 800 nm and 5×10^{13} W/cm^2.

Table 3.3: Orbital binding energies (in eV) of CO_2 computed by VFD with a small number of grids.

Orbital	VFD/LBα	EXP [Ref.]
$1\pi_g$ (HOMO)	13.9	13.8 [150]
$1\pi_u$ (HOMO$-$1)	17.5	17.6 [150]
$3\sigma_u$ (HOMO$-$2)	17.2	18.1 [150]
$4\sigma_g$	18.5	19.4 [150]
$2\sigma_u$	32.4	36.9 [151]
$3\sigma_g$	33.5	38.0 [151]
$2\sigma_g$	293.2	297.5 [148]
$1\sigma_u$	540.2	540.8 [148]
$1\sigma_g$	540.2	540.8 [148]

where [core] indicates $1s$ orbitals of C and two O's. All orbitals except the core orbital participate in the time-propagation. Table 3.3 compares experimental vertical ionization potentials [148, 150, 151] of CO_2 and absolute values of orbital binding energies computed with LBα. We use α=1.16 for the LBα parameter. The grid parameters are the same as ones used in the H_2O calculations in Section 3.5.

Figure 3.7 is a molecular orbital diagram for CO_2 showing how to construct CO_2 molecular orbitals from atomic orbitals of one C atom and two O atoms in the molecular orbital theory [185], based on experimental energy levels and GAMESS calculations [132]. HOMO ($1\pi_g$) is a non-bonding character and mainly constructed from two O $2p_x$ orbitals with opposite phases, so it can be approximated by

$$\psi_{\mathrm{HOMO}} \approx \phi_{\mathrm{O}_A 2p_x} - \phi_{\mathrm{O}_B 2p_x}, \tag{3.32}$$

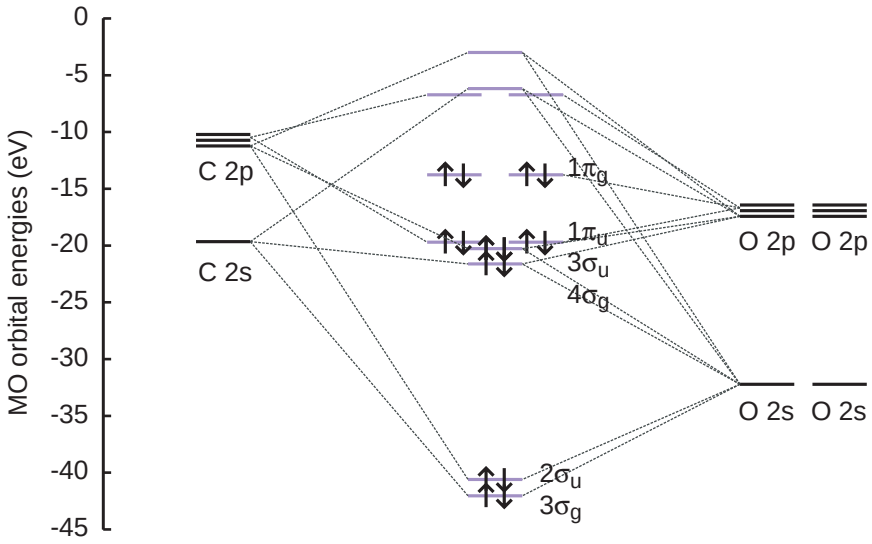

Figure 3.7: Molecular orbital diagram for CO_2.

where O_A and O_B indicate the oxygen atom in the left- and right-hand side of the carbon atom. Thus HOMO of CO_2 is the antisymmetric combination with respect to the phase of two atomic p orbitals.

Figure 3.8 displays orbital pictures of CO_2 with the molecular geometry. The molecular axis coincides with the z-axis and the field polarization lies in the xz-plane. Since CO_2 is a linear molecule, the orientation angle Θ is defined in the same way as N_2 in Eq. (3.27). Note that the z-axis direction is rotated from one in Figs. 3.1 and 3.5 for better representation.

Figure 3.9 shows the orientation dependence of the total ionization probability calculated by Eq. (3.22) as a function of Θ. We used the 20-optical-cycle $\sin^2$-envelope laser pulses with two different sets of the wavelength and the peak intensity: (a) 820 nm and 1.1×10^{14} W/cm^2, and (b) 800 nm and 5×10^{13} W/cm^2. For comparison, Fig. 3.9 includes experimental measurements of Pavičić et al. [164] and Thomann et al. [165], and MO–ADK results [164, 186] with corresponding wavelength and peak intensity. All data sets are normal-

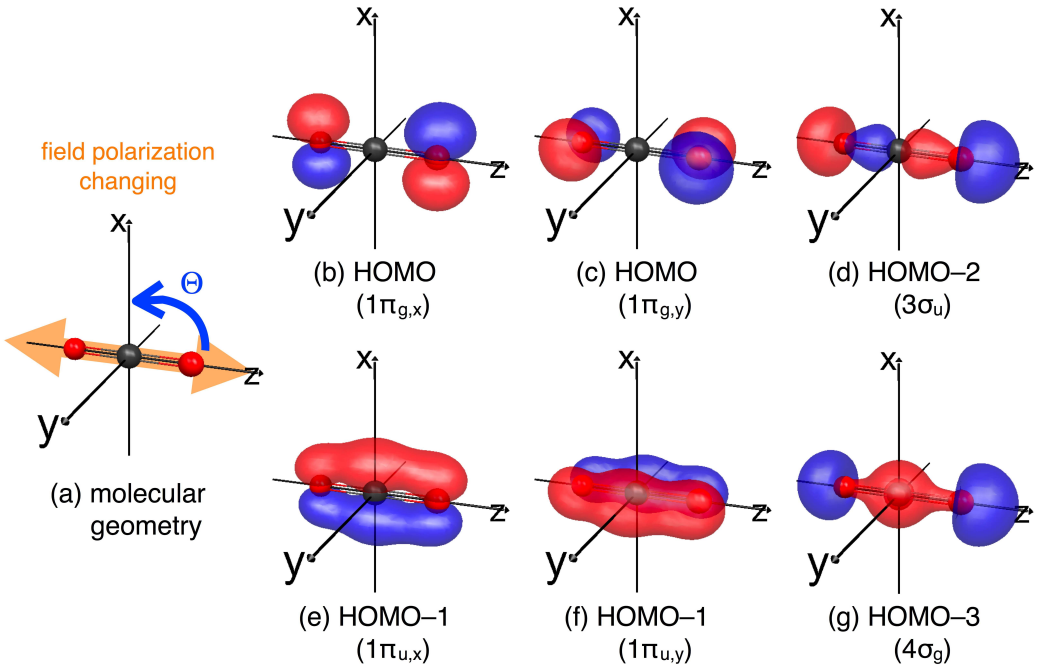

Figure 3.8: Molecular geometry and molecular orbital pictures of CO_2. The principal axis is the z-axis and the molecular geometry is fixed. One carbon atom (black ball) and two oxygen atoms (red ball) are located in the z-axis. The field polarization axis with respect to the principal axis changes toward the x-axis (Θ).

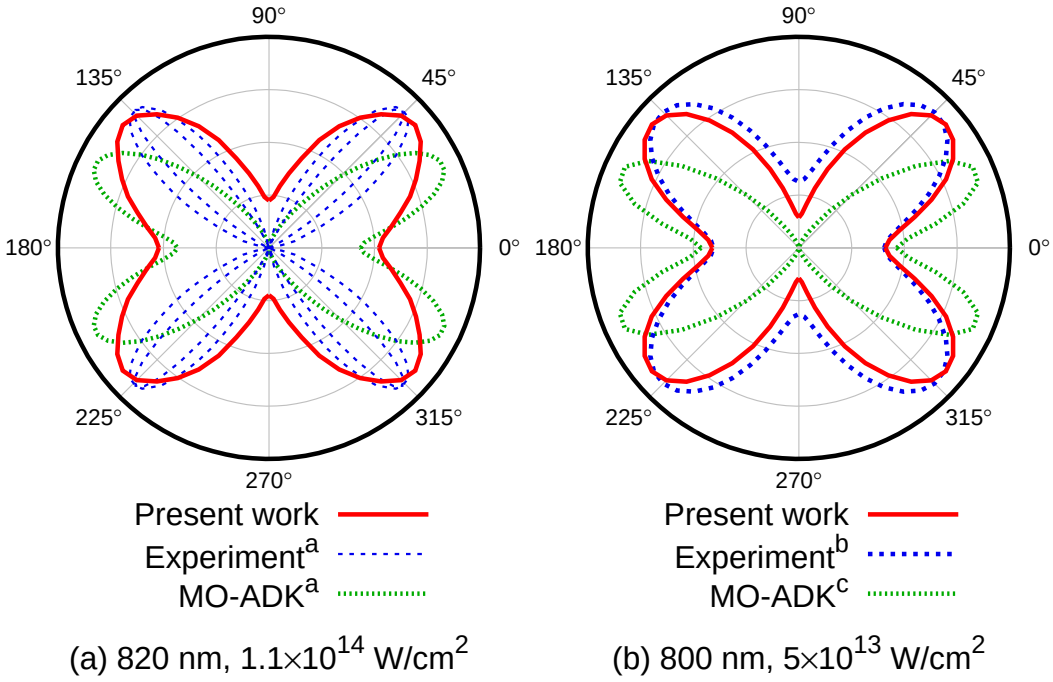

Figure 3.9: Orientation dependence of total ionization probability of CO_2. [a]Pavičić et al. [164]; [b]Thomann et al. [165]; [c]Le et al. [186].

ized to their maximum value. In Fig. 3.9(a), two dashed lines of experiment are due to uncertainty of the measured alignment distribution [164]. The total ionization probability computed from TDDFT manifests the center-fat propeller shape with the maximum peak at 40°, which agrees well with both experimental data of 45°-peak [164, 165]. As for the broadness of the central pattern, our results are in good agreement with the data of Thomann et al. [165] but different from the data of Pavičić et al. [164], the latter showing a narrower pattern. The cause of this discrepancy is unknown but might be related to the experimental uncertainty in the molecular alignment processes. On the other side, the MO–ADK model predicts the 25°-peak butterfly shape for both cases [164, 186]. We note that the strong-field approximation model predicts that the peak maximum occurs at 37° [187] and a recent simulation of the time-dependent Schrödinger equation within the single-active electron approximation predicts a 45°-peak [188].

We now examine contributions of individual orbitals on the total ionization probability. The total ionization probability in Eq. (3.22) can be approximately reduced to the summation of those individual probabilities in the limit of small $P_{i\sigma}(T)$, i.e., $P \approx \sum_{i\sigma} P_{i\sigma}(T)$. Figure 3.10 contains individual ionization probabilities $P_{i\sigma}(T)$ of multiple orbitals with 820 nm and 1.1×10^{14} W/cm^2. HOMO ($1\pi_g$) is dominant in the total ionization and others ($1\pi_u$, $3\sigma_u$, and $4\sigma_g$) are scaled by ten times. Contributions of $2\sigma_u$ and $3\sigma_g$ are negligible. In fact, the unperturbed π orbitals are degenerate: one lies on the xz-plane ($1\pi_{g,x}$ and $1\pi_{u,x}$) and the other lies on the yz-plane ($1\pi_{g,y}$ and $1\pi_{u,y}$). As the field whose polarization vector varies in the xz-plane is applied to the molecule, $1\pi_{g,x}$ provides the most dominant contribution to the orientation dependence of the total ionization probability, which has the 45°-peak maximum. $1\pi_{g,y}$ shows a dumbbell

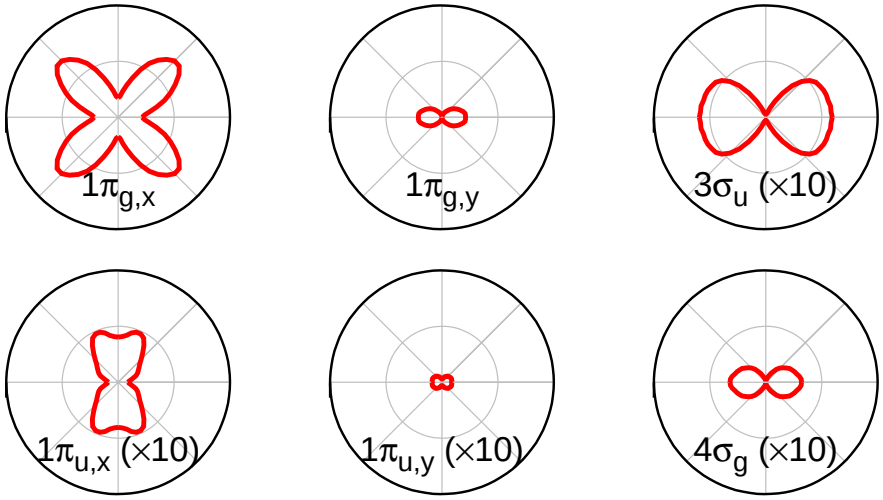

Figure 3.10: Orientation dependence of individual ionization probability of multiple orbitals with 820 nm and 1.1×10^{14} W/cm^2.

shape with the same probability as $1\pi_{g,x}$ at $\Theta = 0°$. Thus, the center-fat propeller shape of the total ionization probability in Fig. 3.9 is mostly reflected by contributions of two HOMOs ($1\pi_{g,x}$ and $1\pi_{g,y}$).

This prediction is particularly different from the MO–ADK butterfly pattern based on the structure and symmetry of the ground state of HOMO [186, 189]. In MO–ADK, it is understood that the peak angle for CO_2 becomes lower than for O_2, despite their same HOMO symmetry, because the internuclear distance between two O's in CO_2 (d=4.392 a.u.) is longer than in O_2 (d=2.287 a.u.) [189]. In contrast, our TDDFT results incorporating multielectron effects reveal that the orientation dependence of the ionization probability of HOMO peaks at 45°, similar to the predicted pattern for O_2 and F_2 that have the same HOMO symmetry [147]. Our all-electron TDDFT study demonstrates the importance of including the electron correlation and all the valence orbitals in the study of strong-field ionization mechanism, even when HOMO is dominant in the ionization process.

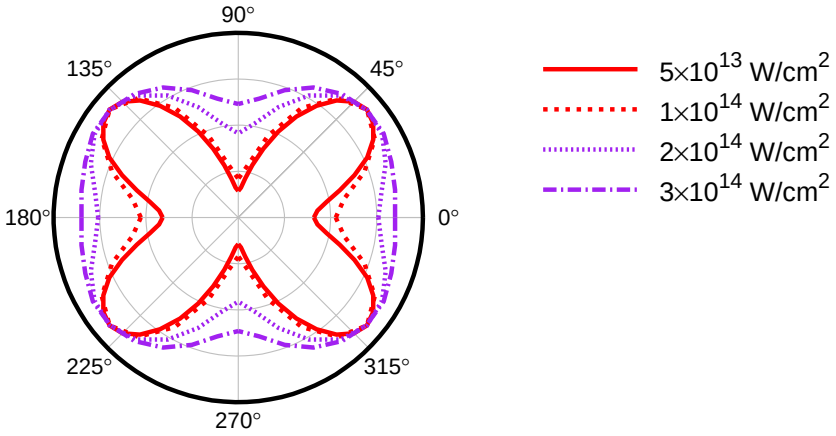

Figure 3.11: Effects of laser intensity on the orientation dependence of total ionization probability of CO_2.

Next, we consider effects of laser intensity on the orientation dependent patterns in Fig. 3.11. The peak intensity of laser pulses is varying from 5×10^{13} to 3×10^{14} W/cm^2, and the wavelength is fixed at 800 nm. All data sets are normalized to their maximum value. As the intensity increases, the polar plot becomes less anisotropic as we observed in the N_2 case in Section 3.4.

3.7 Photoelectron angular distribution of aligned CO_2

To explore the orientation dependence of MPI and its relation to molecular orbital symmetry further, we examine the photoelectron angular distribution (PAD) to visualize where the electron is ionized in the strong field as the field–molecule orientation changes. From the flux analysis of the TDDFT solutions, we can retrieve the information of where the density flows in and out. Then we define an alternative ionization probability and its angular differential form for the complete PAD picture.

From the continuity equation, one can compute the ionization probability rate at time t,

$$\dot{P}_{i\sigma}(t) = -\frac{\partial}{\partial t}\int_V \rho_{i\sigma}(\mathbf{r},t)dV = \int_V \boldsymbol{\nabla}\cdot\mathbf{j}_{i\sigma}(\mathbf{r},t)\,dV, \tag{3.33}$$

where $\rho_{i\sigma}$ is the spin-orbital density, $\rho_{i\sigma}(\mathbf{r},t) = \psi^*_{i\sigma}(\mathbf{r},t)\psi_{i\sigma}(\mathbf{r},t)$, and $\mathbf{j}_{i\sigma}$ is its current density,

$$\begin{aligned}\mathbf{j}_{i\sigma}(\mathbf{r},t) &= \frac{1}{2i}\left[\psi^*_{i\sigma}(\mathbf{r},t)\boldsymbol{\nabla}\psi_{i\sigma}(\mathbf{r},t) - \psi_{i\sigma}(\mathbf{r},t)\boldsymbol{\nabla}\psi^*_{i\sigma}(\mathbf{r},t)\right] \\ &= \mathrm{Im}[\psi^*_{i\sigma}(\mathbf{r},t)\boldsymbol{\nabla}\psi_{i\sigma}(\mathbf{r},t)]\,.\end{aligned} \tag{3.34}$$

From the Gauss' theorem, Eq. (3.33) yields to

$$\dot{P}_{i\sigma}(t) = \int_V \boldsymbol{\nabla}\cdot\mathbf{j}_{i\sigma}(\mathbf{r},t)\,dV = \int_S \mathbf{j}_{i\sigma}(\mathbf{r},t)\cdot\mathbf{n}\,dS. \tag{3.35}$$

In general, V is given by the spherical volume and S is the spherical surface with a large-distance boundary radius. The normal component of the current density on the spherical surface is

$$\mathbf{j}_{i\sigma}(\mathbf{r},t)\cdot\mathbf{n} = \mathrm{Im}\left[\psi^*_{i\sigma}(\mathbf{r},t)\frac{\partial}{\partial r}\psi_{i\sigma}(\mathbf{r},t)\right]. \tag{3.36}$$

Then the time-dependent photoelectron angular distribution is given by

$$\frac{\partial\dot{P}_{i\sigma}(t)}{\partial\Omega} = r_b^2\,\mathrm{Im}\left[\psi^*_{i\sigma}(\mathbf{r},t)\frac{\partial}{\partial r}\psi_{i\sigma}(\mathbf{r},t)\right]_{r=r_b}. \tag{3.37}$$

This expression indicates the rate of the spin-orbital density flowing in and out at time t and at boundary radius r_b that is be chosen to be less than the absorber position r_0 in Eq. (3.29). If the right-hand side of Eq. (3.37) > 0, the electron

density is flowing out of the sphere of the radius r_b. If the right-hand side of Eq. (3.37) < 0, the electron density is flowing into the sphere.

After one pulse (t=T) where T is a pulse duration, one can define the angular differential ionization probability (ADIP) by integrating Eq. (3.37) over t,

$$\frac{\partial P_{i\sigma}}{\partial \Omega} = \int_0^T \frac{\partial \dot{P}_{i\sigma}(t)}{\partial \Omega} dt = \int_0^T r_b^2 \, \mathrm{Im}\left[\psi_{i\sigma}^*(\mathbf{r},t)\frac{\partial}{\partial r}\psi_{i\sigma}(\mathbf{r},t)\right]_{r=r_b} dt. \tag{3.38}$$

Note that in TDVFD calculations the normal component of the current density in Eq. (3.38) is directly calculated by the VFD gradient of the wavefunction and the inner product, $\left\{\mathrm{Im}\left[\psi_{i\sigma}^*(\mathbf{r},t)\boldsymbol{\nabla}\psi_{i\sigma}(\mathbf{r},t)\right]\cdot\mathbf{n}\right\}$, rather than Eq. (3.38) involving $\partial/\partial r$. Any quantity at r_b is evaluated by the VFD interpolation that is simply given by the value of the Voronoi cell encapsulating a given position. The temporal integral is computed over equal-spaced temporal grids. Then the total ADIP is calculated in the same way as in Eq. (3.22),

$$\frac{\partial P}{\partial \Omega} = 1 - \prod_{i\sigma}\left(1 - \frac{\partial P_{i\sigma}}{\partial \Omega}\right). \tag{3.39}$$

Based on this density flux analysis, we can alternatively define the total ionization probability. From Eqs. (3.38) and (3.39), the total ionization probability can be computed by integrating over angles,

$$P_{\mathrm{alt}} = \int_0^{2\pi}\int_0^{\pi} \frac{\partial P}{\partial \Omega} \sin\theta \, d\theta \, d\phi, \tag{3.40}$$

Table 3.4: Comparison of different definitions of the total ionization probability of CO_2.

Angle(°)	P_{conv}	P_{alt}
0	2.62×10^{-2}	2.53×10^{-2}
15	3.24×10^{-2}	3.17×10^{-2}
30	4.14×10^{-2}	4.15×10^{-2}
45	4.45×10^{-2}	4.52×10^{-2}
60	3.34×10^{-2}	3.41×10^{-2}
75	1.83×10^{-2}	1.88×10^{-2}
90	1.13×10^{-2}	1.13×10^{-2}

which is comparable with the conventional definition in Eqs. (3.18)–(3.22) based on the norm of the wavefunction,

$$P_{\text{conv}} = 1 - \prod_{i\sigma} \langle \psi_{i\sigma}(\mathbf{r}, T) | \psi_{i\sigma}(\mathbf{r}, T) \rangle. \tag{3.41}$$

Table 3.4 compares the total ionization probabilities of CO_2 computed by two different definitions, P_{conv} and P_{alt}, at several orientation angles. The wavelength is 820 nm and the peak intensity is 1.1×10^{14} W/cm^2, and other parameters are the same ones used in Fig. 3.9(a). This comparison confirms that the alternative definition by the flux analysis can correctly represent the ionization probability as the conventional one by the norm analysis. Moreover, the alternative ionization probability is more robust than the conventional one because it can resolve angular distribution of the ionization probability.

Now we examine the total ADIP, which is the angular-resolved total ionization probability for the complete PAD picture. Figure 3.12 displays PAD of CO_2 at several field–molecule orientation angles from Θ=0° to Θ=90°, showing a topological transform from a donut shape to a dumbbell shape. Laser param-

eters are the same ones used in Fig. 3.9(a), and 256 angular grids ($l_{\max}$=15) are used for each atom to get higher angular resolution. The orientation dependence of MPI has the maximum peak at Θ=40°, so other angles except Θ=45° are scaled by some factors for better representation. The top and middle panels show contour maps of $\partial P/\partial\Omega$ as a function of Ω on the unit sphere in 3D. In Fig. 3.12, the PAD contour maps exhibit characteristic features of the perturbed HOMO symmetry, because HOMO dominantly contributes to the total ionization. At Θ=0°, PAD forms the donut shape with a nodal point at the center, which is equally from two HOMOs ($1\pi_{g,x}$ and $1\pi_{g,y}$), indicating the retained axial symmetry and degeneracy. At Θ=90°, PAD forms the dumbbell shape with a nodal plane, which is mostly from one HOMO ($1\pi_{g,x}$). Because of the nodal spot and plane at the field polarization axis, the total ionization is suppressed at these orientation angles. On the other hand, PAD at Θ=45°shows a peak spot coincided with the field polarization axis, thus enhancing the total ionization in this direction. It strongly supports the maximum peak of the orientation dependence near this angle.

To closely observe PAD with respect to the field polarization axis, the polar angle θ and the azimuth angle ϕ are defined with respect to the field polarization axis, and then the polar plot as a function of θ is obtained by $\partial P/\partial\theta = \int_0^{2\pi}(\partial P/\partial\Omega)d\phi$. The bottom panels in Fig. 3.12 represent $\partial P/\partial\theta$ at corresponding orientation angles. These plots are comparable with conventional PAD 2D polar plots [167, 190]. Our results indicate the significant advantage of using the 3D PAD visualization, since it provides new dynamical information not realizable by the conventional 2D polar plot. For example, while the patterns of the bottom panels at Θ=0° and Θ=90° look alike, the corresponding 3D patterns are completely different.

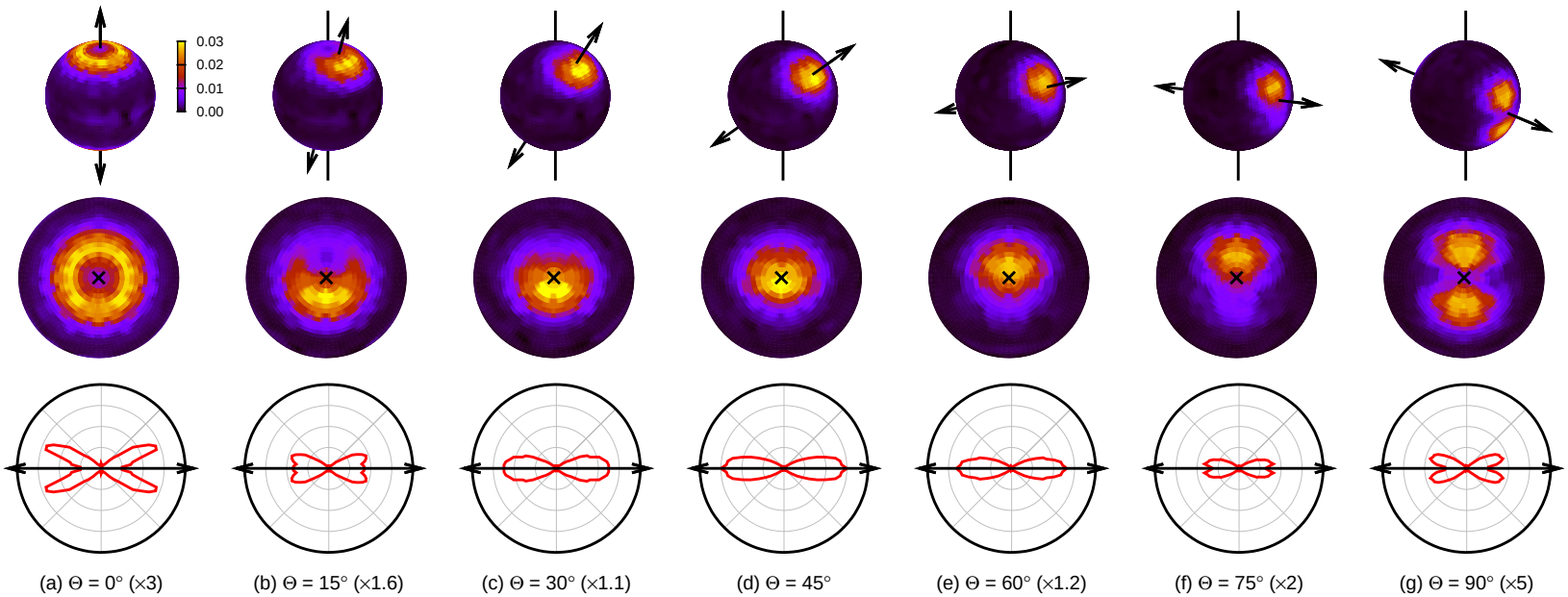

Figure 3.12: 3D contour maps of photoelectron angular distribution at several orientation angles. The top panels display contour maps of $\partial P/\partial\Omega$ on the unit sphere with a vertical line of the molecular axis and an arrow line of the field polarization axis. The middle panels show the same spherical contour maps in different views that the field polarization axis is perpendicular to the paper. The bottom panels represent polar plots of $\partial P/\partial\theta$ with a horizontal arrow line of the field polarization axis.

3.8 High-order harmonic generation of aligned CO_2

We perform HHG calculations for CO_2 with arbitrary field–molecule orientation by means of TDDFT and TDVFD. Figure 3.13 shows the HHG spectrum $S(\omega)$ for CO_2 with the wavelength 800 nm and the peak intensity 1×10^{14} W/cm^2 at two orientation angles Θ=0° and Θ=90°. Other laser parameters are the same as ones used in Section 3.6. Since the HHG calculations require very accurate wavefunctions especially for the long range, the high-order scheme would be preferable. However, the high-order VFD scheme currently described in Section 2.7 has a few drawbacks to be extended for TDDFT calculations. For this reason, we use the first-order VFD method with a large number of grid points for the HHG calculations. We found that the Lebedev scheme for angular grids is suitable for the HHG calculations because its intrinsic symmetry property provides more accurate results for dipole moment calculations. Also a larger mapping parameter L for radial grids is more desirable to achieve better accuracy for higher harmonics. But too large L yields inaccurate core orbitals, thus resulting a collapse of wavefunctions after a few optical cycle of the time propagation. Therefore, L=4–5 a.u. is appropriately recommended with N_r=100 and more for the HHG calculations. In the present calculations, we use N_r=100, L=5 a.u., $r_{\max}$=40 a.u., and $l_{\max}$=10 with the Lebedev grids.

According to the semiclassical model [191, 192], the HHG spectra has a plateau ending at the cut-off energy estimated by $I_p + 3.17U_p$ where I_p is the ionization potential and U_p is the ponderomotive energy that is given by $U_p = E^2/4\omega^2$ where E is the field strength and ω is the field frequency. For the system and field parameters used in our calculations, the cut-off position from the model, $(I_p + 3.17U_p)/\omega$, is expected to be around 21st harmonic order, which

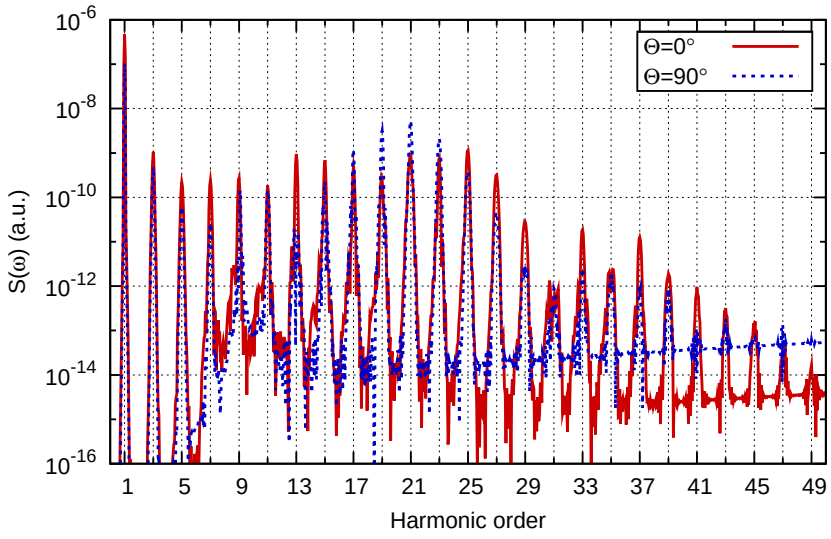

Figure 3.13: HHG spectrum of CO_2 with 800 nm and 1×10^{14} W/cm^2 at the orientation angles Θ=0° (red solid line) and Θ=90° (blue dashed line).

is in fair agreement with our computed data as shown in Fig. 3.13. Molecular HHG spectra demonstrate another hump after the cut-off position, which has been debated regarding to multiple orbital contributions [173]. Also HHG spectra of N_2 and F_2 and its orientation dependence are explained by the multi-electron effects such as interferences among multiple orbital contributions and a resonance between adjacent molecular orbitals [184].

Next we explore the field–molecule orientation dependence of CO_2 HHG. HHG mechanism is well explained by the following three stages [191, 193]: i) an electron is detached from atoms or molecules by multiphoton or tunneling ionization; ii) the electron goes away and comes back influenced by the oscillating field, acquiring a kinetic energy; and iii) a harmonic photon is emitted when the returning electron recombines with the parent core. According to this three-step model, the orientation dependence of HHG can be reflected by two factors: the ionization process and the recombination process. First, the har-

monic generation is enhanced when the ionization probability is maximized and suppressed when it is minimized. Second, quantum interference among different centers may occur in the recombination process. Especially for the diatomic molecules, there are two centers in the parent core, so that two different pathways in recombination lead to quantum interference, which is simply formulated in the two-center interference model [194, 195]. If we assume that all the return kinetic energy of the electron is converted into the harmonic energy, we have the following condition for the interference minima or maxima in the orientation dependence of the harmonic spectra,

$$\cos\Theta = \frac{\pi}{R\sqrt{2n\omega}}, \tag{3.42}$$

where Θ is the orientation angle, R is the distance between two centers, n is the harmonic order, and ω is the incident field frequency. If the molecular orbital responsible for the harmonic emission mechanism is the symmetric combination of atomic orbitals, i.e., the phases of two-center emitters are the same, the condition in Eq. (3.42) gives the minima due to destructive interference. On the other hand, if the molecular orbital is the antisymmetric combination (the opposite phases), Eq. (3.42) yields the maxima due to constructive interference. Even though CO_2 is not a diatomic molecule, it is also subject to the two-center interference model because HOMO of CO_2 is mainly constructed from two atomic p orbitals of oxygen. Indeed, CO_2 has been widely investigated as a testbed for the two-center interference model [161, 196, 197]. HOMO of CO_2 is the antisymmetric combination in Eq. (3.32), so we expect the maximum positions in the orientation dependence.

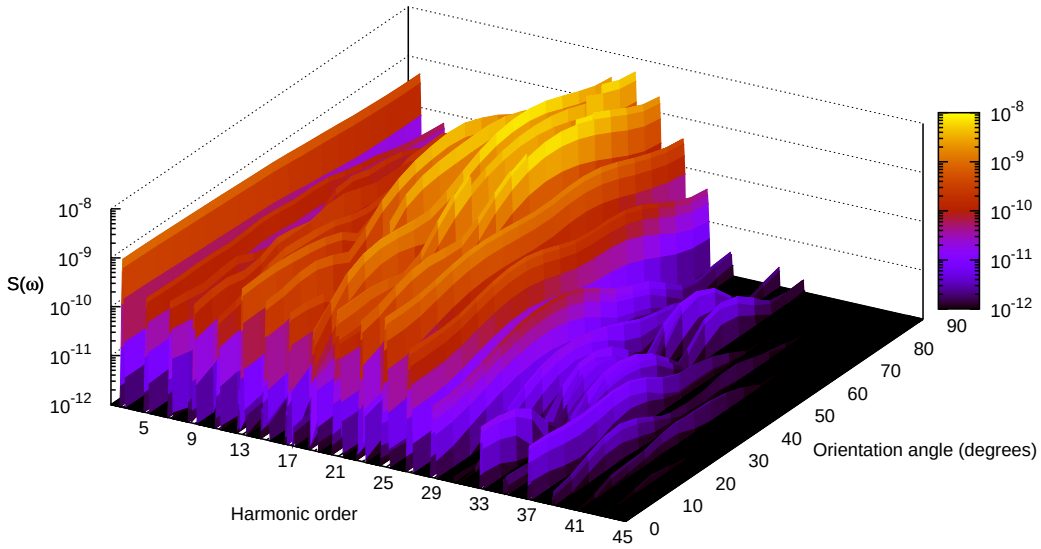

Figure 3.14: Harmonic spectra of CO_2 as a function of the harmonic order and the orientation angle with 800 nm and 1×10^{14} W/cm^2.

Figure 3.14 shows harmonic spectra of CO_2 as a function of the harmonic order n and the orientation angle Θ. Laser parameters are the same as ones used in Fig. 3.13. Overall pattern is that the harmonic spectra have the minimum around Θ=0° and Θ=90° due to the suppression of the ionization process at this angle. Also the harmonic spectra have the maximum around Θ=50–70° for near the cut-off position (n=15–23), rather than around Θ=40° that is the peak angle in the ionization probability as we have seen in Section 3.6. These maximum positions may be explained by the two-center interference. The present harmonic spectra of CO_2 in Fig. 3.14 are in fair agreement with a recent experimental and theoretical results [173].

To see the two-center interference effect in detail, we plot normalized harmonic spectra as a function of Θ for a few harmonics in Fig. 3.15. All data are normalized to the maximum value for each harmonic. As one can see clearly,

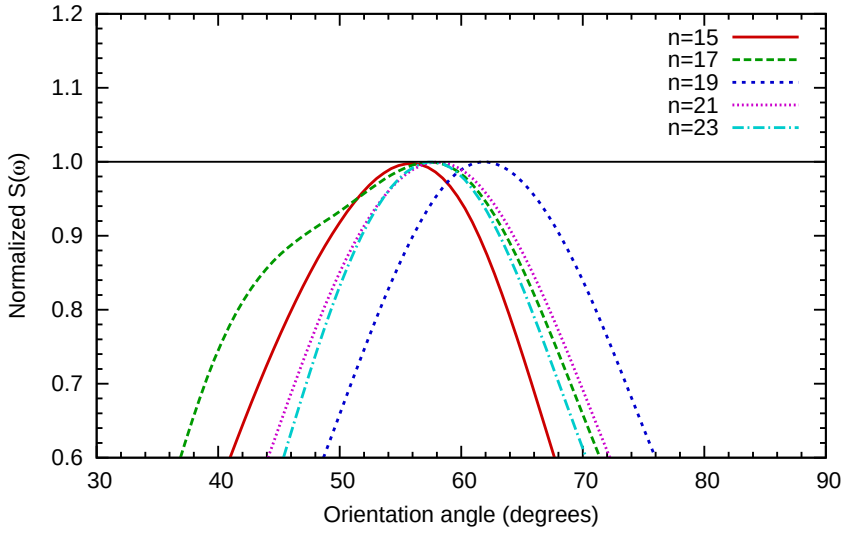

Figure 3.15: Normalized harmonic spectra of CO_2 as a function of the orientation angle with 800 nm and 1×10^{14} W/cm^2.

Table 3.5: Orientation angles of the interference maxima for several harmonics in the HHG spectra of CO_2 with 800 nm and 1×10^{14} W/cm^2.

Harmonic order	15	17	19	21	23
Two-center model	57	59	61	62	64
Present work	56	57	62	58	58

there are the maximum positions in the orientation dependence of the harmonic spectra. In Table 3.5, we compare orientation angles of the interference maxima for several harmonics in the HHG spectra of CO_2, computed by our TDDFT results and the two-center interference model in Eq. (3.42). d=4.392 a.u. is given by the distance between two oxygen atoms. For the harmonic orders less than the cut-off, the maximum positions predicted by the model are in fair agreement with our TDDFT calculations, but agreement is not good after the cut-off position ($n \geq 21$). Also it might be responsible for this disagreement that the simple semiclassical model is not justifiable for weaker intensity [67].

Chapter 4

Many-mode Floquet approach for the study of coherent control of multiphoton processes in frequency-comb laser fields

We extend the many-mode Floquet theorem (MMFT) for the investigation of multiphoton resonance dynamics driven by intense frequency-comb laser fields. The frequency comb structure generated by a train of short laser pulses can be exactly represented by a combination of the main frequency and the repetition frequency. MMFT allows non-perturbative and exact treatment of the interaction of a quantum system with the frequency-comb laser fields. We observe simultaneous multiphoton resonance processes between a two-level system and frequency-comb laser. The multiphoton processes can be coherently controlled by tuning the laser parameters such as the carrier-envelope phase (CEP) shift. High-order harmonic generation (HHG) driven by intense frequency-comb laser has a nested comb structure with the same repetition frequency and different offset for each harmonic. Moreover, HHG driven by intense frequency-comb laser shows immense enhancement by tuning the CEP

shift due to simultaneous multiphoton resonance among all the comb frequencies.

4.1 Frequency-comb laser fields

Frequency-comb laser generated from the mode-locked short-pulse laser has been leading advances in high-precision spectroscopy and ultrafast science [198, 199]. Recent progress of mode-locked laser has allowed to stabilize optical frequency combs by precise control of the absolute comb position and comb spacing [199, 200, 201, 202]. The frequency-comb laser technology has remarkably impacted on high-precision optical frequency measurement and synthesis [203, 204, 205, 206], optical atomic clock [198, 207, 208], as well as high sensitive molecular detection [209, 210].

More recently, the feasibility of the extension of the frequency comb structure and coherence into vuv–xuv regimes via HHG has attracted considerable attention [211, 212, 213, 214]. It is speculated that the frequency comb structure may be retained in each of the higher harmonics. However, currently the experimental realization of the comb structure in higher harmonics has not yet been achieved due to some experimental resolution problems, with the exception of the third harmonic [212] and the 7–13th harmonics [215]. It is also not clear whether the frequency comb structure and coherence can survive in very high-order harmonics and in the situation where substantial ionization occurs in the presence of high intensity laser fields. To advance this field, we have recently presented *ab initio* theoretical exploration of the frequency comb structure and coherence in the vuv–xuv regimes via HHG from the hydrogen atom by propagating the time-dependent Schrödinger equation [55] and from the he-

lium atom by using time-dependent density-functional theory [216]. We found that each harmonic (from the first harmonic all the way to the cutoff) has a nested comb structure and this global pattern persists regardless of the time interval and the number of pulses, even in the presence of appreciable ionization. We also showed that the comb structure of the harmonics originates from quantum interferences among induced dipole moment pulses by use of the spectral phase analysis [55].

4.2 Field expressions in the time and frequency domains

We derive field expressions of frequency-comb laser in the frequency domain and in the time domain, and then make an explicit connection between them to be suitable for the Floquet formalism in Section 4.3. Basically, frequency-comb laser consists of spectral comb lines in the frequency domain [199, 201],

$$\omega_m = m\omega_r + \omega_\delta \tag{4.1}$$

where ω_r is the repetition angular frequency, m is an integer index, and ω_δ is the offset angular frequency $(0 \leq \omega_\delta < \omega_r)$. This frequency-comb laser can be generated by a temporal train of short laser pulses which have the carrier (fundamental) angular frequency ω_c and the time interval τ between pulses. Because the time period $(=2\pi/\omega_c)$ of the carrier wave and the time duration $\tau(=2\pi/\omega_r)$ of the pulse envelope are often incommensurate, there is the carrier-envelope phase (CEP) after each pulse: $\phi = \omega_c\tau$. Current mode-locking laser technique allows us to precisely control the CEP by including the pulse-to-pulse CEP shift $\Delta\phi$ that plays a key role in stabilizing of the comb structure [200]. The CEP shift

$\Delta\phi$ determines all absolute positions of frequencies in the comb structure by setting the offset frequency $\omega_\delta = \Delta\phi/\tau$.

The electric field for a train of pulses with the CEP shift in the time domain [201] is expressed by

$$E(t) = \sum_{n=1}^{N_p} f(t - n\tau) e^{i(\omega_c t - n\omega_c \tau + n\Delta\phi)}, \tag{4.2}$$

where N_p is the number of pulses and $f(t)$ is the envelope function for one pulse in the time domain. After the Fourier transform, the electric field in the frequency domain [201] is given by

$$\tilde{E}(\omega) = \tilde{f}(\omega - \omega_c) \sum_{n=1}^{N_p} e^{-in(\omega\tau - \Delta\phi)}, \tag{4.3}$$

where $\tilde{f}(\omega) = \int f(t) e^{-i\omega t} dt$ determines the field strength in the spectrum as the envelope function in the frequency domain. The summation of the exponentials generates frequency comb structure because they are added up with constructive interferences only at $\omega\tau - \Delta\phi = 2\pi m$ with an arbitrary integer m [200]. In other words, the summation becomes a series of frequency lines at $\omega = \omega_m$ such that

$$\omega_m = \frac{2\pi m}{\tau} + \frac{\Delta\phi}{\tau} = m\omega_r + \omega_\delta, \tag{4.4}$$

which is shown as the comb frequency expression in Eq. (4.1). Without loss of generality, we can rewrite these comb frequencies with a main angular frequency ω_0,

$$\omega_k = \omega_0 + k\omega_r, \tag{4.5}$$

where k is an integer index and ω_0 is the main angular frequency defined to be the frequency in $\{\omega_m\}$ whose field amplitude is the maximum in the frequency domain. In other words, ω_0 is the closest frequency to ω_c among all the comb frequencies. The relation between ω_0 and ω_c is given by

$$\omega_0 = \left[\frac{\omega_c - \omega_\delta}{\omega_r}\right]\omega_r + \omega_\delta, \tag{4.6}$$

where [ ] is the round function. Note that the fundamental frequency ω_c is not necessarily one of the comb frequencies nor does it equal ω_0 in general. But if we choose $\omega_c = \omega_0$ or $\omega_c \in \{\omega_k\}$, then ω_δ will be a reminder of ω_c divided by ω_r.

When the number of pulses increases, the spectral width of each frequency comb becomes narrower due to quantum interference [55, 205]. In the ideal case that an infinite number of pulses are added up, the summation part in Eq. (4.3) yields a series of delta functions centered at each ω_k,

$$\lim_{N_p\to\infty}\sum_{n=1}^{N_p} e^{-in(\omega\tau-\Delta\phi)} = \frac{2\pi}{\tau}\sum_{k=-\infty}^{\infty}\delta(\omega-\omega_k). \tag{4.7}$$

Thus, the ideal comb laser field in the frequency domain can be represented by

$$\tilde{E}^{\circ}(\omega) = \tilde{f}(\omega-\omega_c)\omega_r\sum_{k=-\infty}^{\infty}\delta(\omega-\omega_k), \tag{4.8}$$

where $^\circ$ denotes the ideal case. After applying the inverse Fourier transform to $\tilde{E}^{\circ}(\omega)$, we obtain a time-domain expression for the electric field of the ideal

comb laser,

$$E^{\circ}(t) = \frac{\omega_r}{2\pi} \sum_{k=-\infty}^{\infty} \int_{-\infty}^{\infty} \delta(\omega - \omega_k) \tilde{f}(\omega - \omega_c) e^{i\omega t} d\omega = \sum_{k=-\infty}^{\infty} E_k e^{i\omega_k t}, \tag{4.9}$$

where $E_k = \tilde{f}(\omega_k - \omega_c)\omega_r/2\pi$ represents the field amplitude of ω_k. This summation of exponentials of the angular frequencies $\{\omega_k\}$ with their field amplitudes $\{E_k\}$ is coherently added up and then generates the ideal comb structure in the frequency domain. Inversely, this expression plots an infinite number of train pulses in the time domain, i.e., Eq. (4.9) is identical to Eq. (4.2) if N_p goes to infinity.

If the envelope function $f(t)$ is given by a Gaussian form, then the infinite summation in Eq. (4.9) will reduce to the finite summation, and the field amplitudes can be explicitly determined. Let $f(t) = f_0 e^{-t^2/2\sigma^2}$ where f_0 is the peak field amplitude at $t = 0$ and σ is the standard deviation of the Gaussian function. An integer number N is chosen such that $E_k \approx 0$ when $|k| > N$. As a result, the electric field of $(2N + 1)$ comb frequencies is given by

$$E(t) = \sum_{k=-N}^{N} E_k e^{i\omega_k t}, \tag{4.10}$$

where the field amplitude E_k corresponding to ω_k is explicitly derived as,

$$E_k = \frac{\omega_r}{2\pi} \int_{-\infty}^{\infty} f_0 e^{-t'^2/2\sigma^2} e^{-i(\omega_k - \omega_c)t'} dt' = \frac{f_0 \sigma \omega_r}{\sqrt{2\pi}} e^{-\sigma^2(\omega_0 - \omega_c + k\omega_r)^2/2}. \tag{4.11}$$

Note that the standard deviation σ of the Gaussian function is related to full width at half maximum (FWHM $= 2\sigma\sqrt{2\ln 2}$).

To investigate the interaction of an atomic or molecular system with the comb laser generated by a finite number of pulses, Eq. (4.2) has been employed

for solving the time-dependent Schrödinger equation in the time domain [55]. On the other hand, for the ideal comb laser generated by an infinite number of pulses, Eq. (4.10) is more preferable to use, but it may require infinite duration time for the time propagation. Consequently, in order to consider the interaction with the ideal comb laser, it is more expedient to avoid the time propagation of wavefunctions.

4.3 Many-mode Floquet theoretical treatment for the interaction of a quantum system with frequency-comb laser

The many-mode Floquet theory (MMFT) [28, 217, 218, 219, 220] can be applied to the solution of the polychromatic or quasi-periodic time-dependent Schrödinger equation without the time propagation of wavefunctions. Let us now consider the interaction of an atomic or molecular system with a linearly polarized frequency-comb laser parallel to the z-axis. The corresponding Hamiltonian including $(2N+1)$ comb frequencies is given by,

$$\begin{aligned} H(\mathbf{r},t) &= \hat{H}_0(\mathbf{r}) - \sum_{k=-N}^{N} \boldsymbol{\mu}(\mathbf{r}) \cdot \mathbf{E}_k \,\mathrm{Re}\left[e^{i\omega_k t}\right] \\ &= \hat{H}_0(\mathbf{r}) - \sum_{k=-N}^{N} \hat{z} E_k \cos\omega_k t \\ &= \hat{H}_0(\mathbf{r}) - \sum_{k=-N}^{N} \tfrac{1}{2}\hat{z} E_k \left[e^{i(\omega_0+k\omega_r)t} + e^{-i(\omega_0+k\omega_r)t}\right], \end{aligned} \tag{4.12}$$

where $\hat{H}_0(\mathbf{r})$ is the unperturbed Hamiltonian of the system and $\boldsymbol{\mu}(\mathbf{r})$ is the electric dipole moment operator.

The MMFT states that any polychromatic (multi-color laser-field) problem has the exact solution in terms of the generalized many-mode quasienergy

eigenvalues and eigenfunctions [28, 217]. Because all the comb frequencies can be represented by two variables, ω_0 and ω_r, we can employ the two-mode Floquet theory with double Fourier components,

$$|\alpha nm\rangle = |\alpha\rangle \otimes |n\rangle \otimes |m\rangle, \tag{4.13}$$

where α is the system index, and n and m are Fourier components of ω_0 and ω_r, respectively. Then, the Hamiltonian can be expanded with double Fourier components of n and m,

$$H(\mathbf{r}, t) = \sum_{n,m} H^{[n,m]}(\mathbf{r}) e^{-i(n\omega_0 + m\omega_r)t}, \tag{4.14}$$

where

$$\begin{aligned}
H^{[0,0]} &= \hat{H}_0, \\
H^{[-1,0]} &= H^{[+1,0]} = -\tfrac{1}{2}\hat{z}E_0, \\
H^{[-1,-1]} = H^{[+1,+1]} &= -\tfrac{1}{2}\hat{z}E_1, \quad H^{[-1,+1]} = H^{[+1,-1]} = -\tfrac{1}{2}\hat{z}E_{-1}, \\
H^{[-1,-2]} = H^{[+1,+2]} &= -\tfrac{1}{2}\hat{z}E_2, \quad H^{[-1,+2]} = H^{[+1,-2]} = -\tfrac{1}{2}\hat{z}E_{-2}, \\
&\vdots \qquad\qquad\qquad \vdots \\
H^{[-1,-N]} = H^{[+1,+N]} &= -\tfrac{1}{2}\hat{z}E_N, \quad H^{[-1,+N]} = H^{[+1,-N]} = -\tfrac{1}{2}\hat{z}E_{-N}.
\end{aligned} \tag{4.15}$$

The MMFT allows the exact transformation of the time-dependent problem into an equivalent time-independent infinite-dimensional generalized Floquet matrix eigenvalue problem,

$$\sum_{\beta}\sum_{n'}\sum_{m'} \langle \alpha nm|H_F|\beta n'm'\rangle\langle \beta n'm'|\lambda\rangle = \lambda\langle \alpha nm|\lambda\rangle, \tag{4.16}$$

where λ is the quasienergy eigenvalue and $|\lambda\rangle$ is the corresponding eigenvector. The two-mode Floquet matrix H_F is constructed by

$$\langle \alpha n m | H_F | \beta n' m' \rangle = H_{\alpha\beta}^{[n-n',m-m']} + (n\omega_0 + m\omega_r)\delta_{\alpha,\beta}\delta_{n,n'}\delta_{m,m'}, \tag{4.17}$$

where

$$\begin{aligned} H_{\alpha\beta}^{[n-n',m-m']} &= \langle \alpha | H^{[n-n',m-m']} | \beta \rangle \\ &= \varepsilon_\alpha \delta_{\alpha,\beta}\delta_{n,n'}\delta_{m,m'} + \sum_{k=-N}^{N} V_{\alpha\beta}^{(k)} \left(\delta_{n+1,n'}\delta_{m+k,m'} + \delta_{n-1,n'}\delta_{m-k,m'} \right), \\ \varepsilon_\alpha &= \langle \alpha | \hat{H}_0 | \alpha \rangle \quad \text{and} \quad V_{\alpha\beta}^{(k)} = -\tfrac{1}{2} E_k \langle \alpha | \hat{z} | \beta \rangle. \end{aligned} \tag{4.18}$$

The H_F matrix has a block band-diagonal structure with infinite-dimensional diagonal blocks and subdiagonal blocks corresponding to interactions between the quantum system and the $(2N+1)$ comb frequencies. The structure of H_F for the linearly polarized case is as follows,

$$H_F = \begin{pmatrix} \ddots & & & & & \vdots & \\ & A + 2\omega_r I & B_1 & B_2 & B_3 & B_4 & \cdots \\ & B_1^T & A + \omega_r I & B_1 & B_2 & B_3 & \\ & B_2^T & B_1^T & A & B_1 & B_2 & \\ & B_3^T & B_2^T & B_1^T & A - \omega_r I & B_1 & \\ \cdots & B_4^T & B_3^T & B_2^T & B_1^T & A - 2\omega_r I & \\ & \vdots & & & & & \ddots \end{pmatrix}, \tag{4.19}$$

where A is a block tridiagonal matrix and B_k is a block off-diagonal matrix.

$$A = \begin{pmatrix} \ddots & & & & & \vdots & \\ & Z+2\omega_0 I & X & 0 & 0 & 0 & \cdots \\ & X & Z+\omega_0 I & X & 0 & 0 & \\ & 0 & X & Z & X & 0 & \\ & 0 & 0 & X & Z-\omega_0 I & X & \\ \cdots & 0 & 0 & 0 & X & Z-2\omega_0 I & \\ & \vdots & & & & & \ddots \end{pmatrix}, \tag{4.20}$$

$$B_k = \begin{pmatrix} \ddots & & & & \vdots & \\ & 0 & Y_k & 0 & 0 & 0 & \cdots \\ & Y_{-k} & 0 & Y_k & 0 & 0 & \\ & 0 & Y_{-k} & 0 & Y_k & 0 & \\ & 0 & 0 & Y_{-k} & 0 & Y_k & \\ \cdots & 0 & 0 & 0 & Y_{-k} & 0 & \\ & \vdots & & & & & \ddots \end{pmatrix}. \tag{4.21}$$

The matrices of X, Y_k, and Z which form blocks in A and B have the following forms,

$$X = \begin{pmatrix} 0 & V^{(0)}_{\alpha\beta} & V^{(0)}_{\alpha\gamma} & \cdots \\ V^{(0)}_{\beta\alpha} & 0 & V^{(0)}_{\beta\gamma} & \\ V^{(0)}_{\gamma\alpha} & V^{(0)}_{\gamma\beta} & 0 & \\ \vdots & & & \ddots \end{pmatrix}, \quad Y_k = \begin{pmatrix} 0 & V^{(k)}_{\alpha\beta} & V^{(k)}_{\alpha\gamma} & \cdots \\ V^{(k)}_{\beta\alpha} & 0 & V^{(k)}_{\beta\gamma} & \\ V^{(k)}_{\gamma\alpha} & V^{(k)}_{\gamma\beta} & 0 & \\ \vdots & & & \ddots \end{pmatrix},$$
$$Z = \begin{pmatrix} \varepsilon_\alpha & 0 & 0 & \cdots \\ 0 & \varepsilon_\beta & 0 & \\ 0 & 0 & \varepsilon_\gamma & \\ \vdots & & & \ddots \end{pmatrix}. \tag{4.22}$$

After solving the eigenvalue problem of the generalized Floquet matrix, the time-averaged transition probability can be computed from the quasienergy eigenvectors [217],

$$\bar{P}_{\alpha\to\beta} = \sum_{n,m} \sum_{\gamma,n',m'} \left| \langle \beta n m | \lambda_{\gamma n' m'} \rangle \langle \lambda_{\gamma n' m'} | \alpha 00 \rangle \right|^2, \tag{4.23}$$

which has the maximum value of $\frac{1}{2}$ at avoided crossings of quasienergies associated with multiphoton resonance transitions [218]. The induced dipole moment can be likewise expanded in double Fourier series,

$$\mathbf{d}(t) = \sum_{n,m} \mathbf{d}_{n,m} e^{-i(n\omega_0 + m\omega_r)t}. \tag{4.24}$$

If n and m are given, the angular frequency ω is determined by $\omega = n\omega_0 + m\omega_r$. The HHG power spectra in the length form can be expressed by [45]

$$P(n\omega_0 + m\omega_r) = |\mathbf{d}_{n,m}|^2 = \left| \sum_{n',m'} \langle \lambda_{\beta,n'-n,m'-m} | \hat{z} | \lambda_{\alpha,n',m'} \rangle \right|^2 . \tag{4.25}$$

Here harmonic order is defined by ω/ω_c and can be a fractional number because of the comb structure of frequencies.

4.4 Coherent control of multiphoton resonance dynamics of a two-level system

In this section, we present a case study of the multiphoton resonance enhancement of a two-level system driven by frequency-comb laser fields. The laser parameters used are peak intensity 2.5×10^{15} W/cm^2, carrier frequency 563.5 THz (corresponding to $\omega_c = 0.0856454$ a.u. and wavelength 532 nm), and repetition frequency 10 THz (corresponding to $\omega_r = 1.51983 \times 10^{-3}$ a.u. and pulse separation $\tau = 0.1$ ps) generated from a train of Gaussian pulses with 20 fs FWHM. The main frequency ω_0 is set to be the carrier frequency ω_c, so that the offset angular frequency ω_δ is chosen to be a reminder of ω_c divided by ω_r. For the two-level system, the transition dipole moment $\langle \alpha | \hat{z} | \beta \rangle = 0.1$ a.u. is used. Fig. 4.1(a) shows the two-mode quasienergies, and Fig. 4.1(b) shows the time-averaged transition probabilities as a function of energy separation of the two-level system, $\hbar\omega_{\alpha\beta} = \varepsilon_\beta - \varepsilon_\alpha$, varying from 0.0 to 0.5 a.u. Multiphoton resonances are found near odd numbers of ω_c similar to the one-mode Floquet calculation [221]. However, a cluster of resonances are observed in the vicinity of resonance positions due to the comb structure of frequencies. The

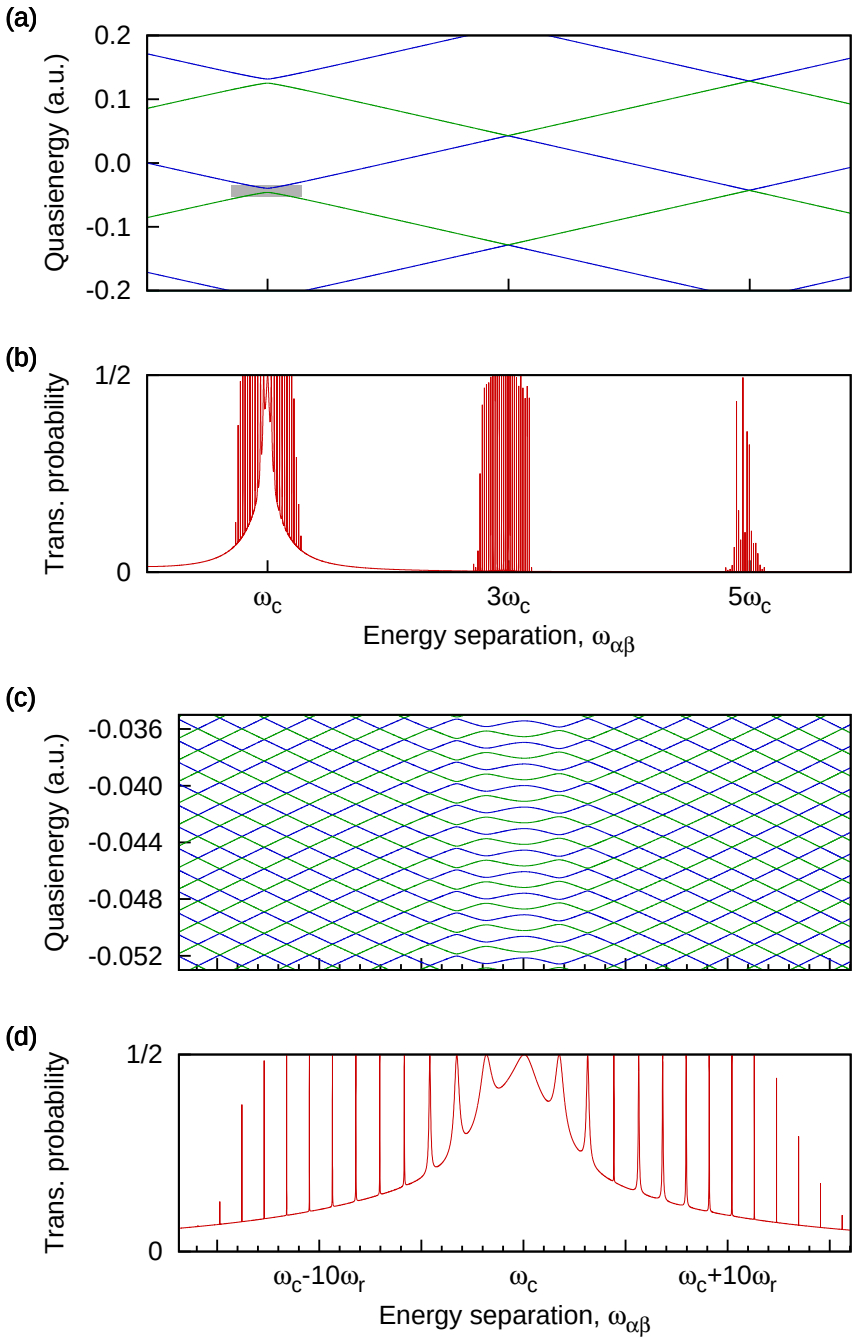

Figure 4.1: (a) Quasienergies and (b) time-averaged transition probabilities as a function of the energy separation, for the two-level system driven by frequency-comb laser fields with peak intensity 2.5×10^{15} W/cm^2, carrier frequency 563.5 THz, and repetition frequency 10 THz of 20 fs FWHM Gaussian pulses. (c) Enlarged quasienergy plots in the one-photon resonance regime corresponding to the gray box in (a). (d) The corresponding time-averaged transition probabilities.

quasi-periodic structure of the quasienergies can be represented by [217, 218],

$$\lambda_{\gamma nm} = \lambda_\gamma + n\omega_0 + m\omega_r, \tag{4.26}$$

where n is an even integer when $\gamma = \alpha$ and an odd integer when $\gamma = \beta$ due to parity consideration. Because of multiples of ω_r, the quasienergy plot becomes more complicated with avoided crossings as shown in Fig. 4.1(c), where the one-photon dominant resonance pattern is enlarged from the gray box in (a). The corresponding transition probabilities are shown in Fig. 4.1(d).

Many features of the frequency-comb structure can be explained by simultaneous multiphoton resonances that occur due to the multitude of frequencies at the same time. Let us consider an n-photon resonance condition of a monochromatic frequency ω,

$$\omega_{\text{res}} = n\omega, \tag{4.27}$$

where ω_{res} is the resonance frequency. On the other side, when one comb frequency ω is on n-photon resonance, many combinations of comb frequencies can simultaneously contribute to that multiphoton resonance. For example, if $\omega_{\text{res}} = n\omega$ where $\omega \in \{m\omega_r + \omega_\delta\}$, then a combination of $(n-2)\omega$, $\omega - \omega_r$, and $\omega + \omega_r$ is also on resonance with ω_{res}. Thus, all combinations of ω with $\pm l\omega_r (l : \text{integer})$ are also contributed to the resonance. Consequently, the n-photon resonance condition with frequency combs can be expressed by the congruence relation of real numbers,

$$\omega_{\text{res}} \equiv n\omega \pmod{\omega_r}. \tag{4.28}$$

Eq. (4.28) means the reminders of ω_{res} and $n\omega$ are the same when divided by ω_r.

Now, we explore the optimization of the multiphoton resonance processes by tuning the CEP shift $\Delta\phi$. We note that changing the CEP shift, the resonance processes can be easily achieved because $\Delta\phi$ determines absolute comb positions more precisely than ω_c and even ω_r ($\omega_\delta = \omega_r \Delta\phi/2\pi$). For example, with the laser parameters used in Fig. 4.1, 1% variation on $\Delta\phi$ yields 0.018% changes on frequencies, which emphasizes the control of the CEP shift in comb laser is much easier than the control of the carrier frequency in one-mode (monochromatic) laser to reach the resonance frequency. Also the resonance position will be retained when the phases vary because the pulse energy is conserved. Moreover, when the CEP shift is varied, it is possible to achieve n times of n-photon resonance, where n is an odd number. If comb frequencies with the offset ω_δ are n-photon resonant with ω_{res},

$$\begin{aligned} \omega_{\text{res}} &\equiv n(m\omega_r + \omega_\delta) \pmod{\omega_r} \\ &\equiv n\omega_\delta \pmod{\omega_r}, \end{aligned} \tag{4.29}$$

then $\omega_\delta + \frac{j}{n}\omega_r$ (j: integer, $0 \leq j < n$) are also n-photon resonant with ω_{res}, leading to simultaneous multiphoton resonances, because

$$n\left(m\omega_r + \omega_\delta + \frac{j}{n}\omega_r\right) \equiv n\omega_\delta \pmod{\omega_r}. \tag{4.30}$$

Eqs. (4.29) and (4.30) show that comb frequencies with ω_δ and with $\omega_\delta + \frac{j}{n}\omega_r$ have the same reminder as ω_{res} when divided by ω_r. The CEP shifts of comb

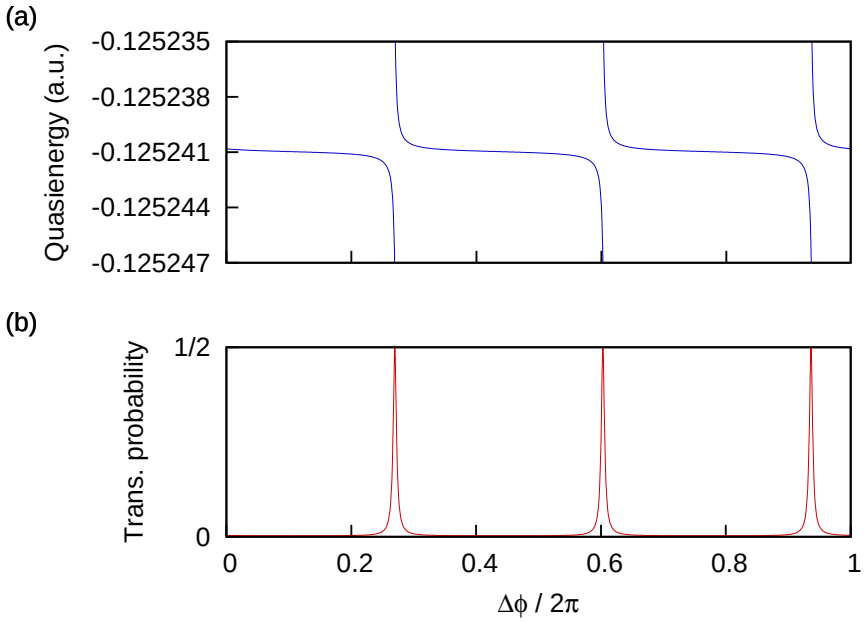

Figure 4.2: (a) Quasienergies and (b) time-averaged transition probabilities as a function of the CEP shift $\Delta\phi$. It shows three resonance positions separated by $2\pi/3$ due to three-photon dominant resonance.

frequencies with the offset $\omega_\delta + \frac{j}{n}\omega_r$ are given by

$$\Delta\phi_j = 2\pi\left(\frac{\omega_\delta}{\omega_r} + \frac{j}{n}\right) \quad (0 \leq j < n), \tag{4.31}$$

so that resonance peak positions of $\Delta\phi_j$ are separated by $2\pi/n$. Fig. 4.2 shows (a) the quasienergies and (b) the time-averaged transition probabilities as a function of the CEP shift. The energy separation is fixed at $\omega_{\alpha\beta} = 0.25$ a.u. which corresponds to the three-photon dominant resonance regime ($3\omega_c \approx \omega_{\alpha\beta}$), and $\Delta\phi$ is varied ($0 \leq \Delta\phi < 2\pi$). Other laser parameters are the same as those in Fig. 4.1. Shown in Fig. 4.2 is the case of three-photon dominant resonance. Here the resonance can be achieved three times by varying the CEP shift, and these three peaks are separated by $2\pi/3$ exactly.

4.5 Enhancement of high-order harmonic generation

In Fig. 4.3, we present the HHG power spectrum of two-level systems driven by frequency-comb laser. The laser parameters are the same as those in Fig. 4.1 and the energy separation is fixed at $\omega_{\alpha\beta} = 0.25$ a.u. For comparison, HHG driven by one-mode laser with the same carrier frequency and the corresponding root-mean-square field strength is plotted with the dots in Fig. 4.3, computed by one-mode Floquet calculation. Note that HHG spectrum driven by comb laser is orders of magnitude higher than that by one-mode laser. In addition, HHG driven by comb laser forms a nested comb structure within each of the harmonics, due to the constructive interferences among the sequence of induced dipoles generated by the incident sequence of laser pulses [55]. For instance, the comb structure within the fifth-order harmonic is shown in the inset in Fig. 4.3. Each of the harmonic orders has the same repetition angular frequency ω_r and the offset angular frequency $n\omega_\delta$ for the nth-order harmonic. The frequency comb spectrum for the nth-order harmonic can be expressed with ω_0,

$$\omega'_k = n\omega_0 + k\omega_r, \tag{4.32}$$

or expressed with ω_δ,

$$\omega'_m = n\omega_\delta + m\omega_r, \tag{4.33}$$

where m and k are an integer index.

Finally, we investigate the coherent control and enhancement of the HHG power spectra by tuning the CEP shift to achieve multiphoton resonances. Figure 4.4 shows the enhancement of HHG by varying the CEP shift, $\Delta\phi/2\pi$=0.1 (off-resonance), 0.168, and 0.168295 (near-resonance) with peak intensity $1 \times$

10^{14} W/cm^2. Other parameters for comb laser and the system are the same as those in Fig. 4.3. Table 4.1 lists the power spectrum values of the maximum peak for the near- and off-resonance cases with several peak intensities. Figure 4.4 and Table 4.1 show that HHG peaks can be dramatically enhanced by varying the CEP shift due to simultaneous multiphoton resonances. In the case of n-photon resonance processes, the system can easily reach the excited state by the absorption of n photons and the higher-order ($>n$) harmonic spectra can be also enhanced. The power spectra of I=1 $\times$ 10^{14} W/cm^2 are enhanced by about 10^8 times. For the case of I=1 $\times$ 10^{15} W/cm^2, an enhancement factor is about 10^5 times, while for the case of I=2.5 $\times$ 10^{15} W/cm^2, it is about 10^3 times. Note that similar enhancement is observed at other resonance positions of the CEP shift. For example, Fig. 4.2(b) indicates three different resonance positions of $\Delta\phi$ at I=2.5 $\times$ 10^{15} W/cm^2. The enhancement factors of the HHG power spectrum with $\Delta\phi/2\pi$=0.2697, or $0.2697 + 1/3$, or $0.2697 + 2/3$ are all the same about 10^3 times.

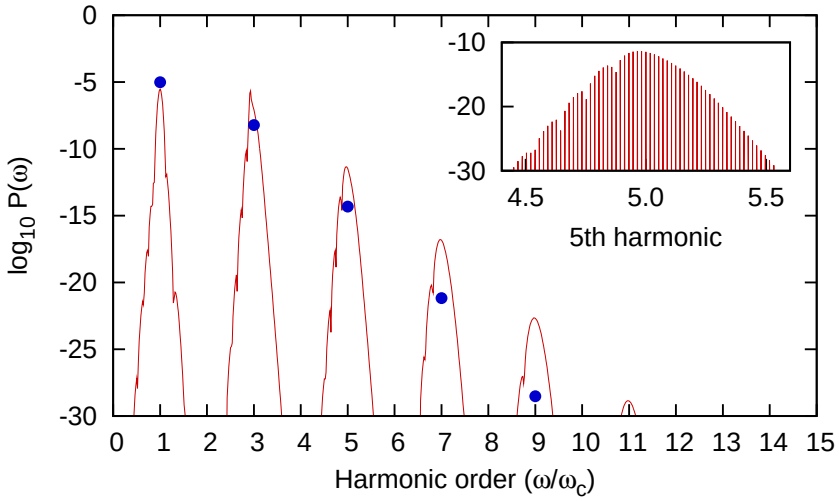

Figure 4.3: HHG power spectrum of two-level systems driven by frequency-comb laser. Each harmonic has a nested comb structure as clearly shown in the inset for the fifth harmonic. For clarity, all comb peaks are connected by a line. The laser parameters are the same as those in Fig. 4.1. Dots represent HHG spectra driven by the corresponding one-mode laser.

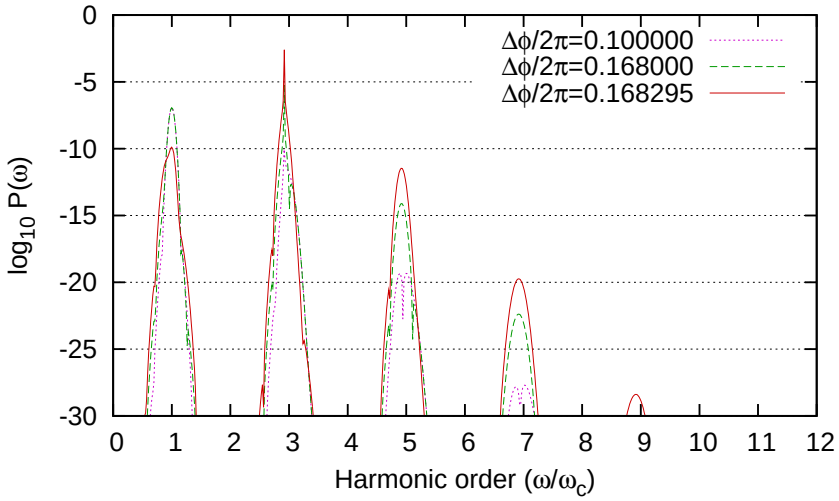

Figure 4.4: Enhancement of HHG by tuning the CEP shift with peak intensity 1×10^{14} W/cm^2. For clarity, HHG peaks of the comb structure are connected by a line.

Table 4.1: Effects on the power spectra by varying the CEP shift $\Delta\phi$. q is the harmonic order of the maximum peak for each harmonic and $P(q\omega_c)$ is the corresponding to power spectrum at $\omega = q\omega_c$. The label A indicates $\Delta\phi/2\pi = 0.1$ that shows off-resonance cases, while B indicates the near-resonance cases: $\Delta\phi/2\pi = 0.168295$, 0.20653, and 0.2697 for 1×10^{14}, 1×10^{15}, and 2.5×10^{15} W/cm^2, respectively. The number in brackets indicates the power of 10.

	A		B	
Intensity (W/cm^2)	q	$P(q\omega_c)$	q	$P(q\omega_c)$
1×10^{14}	2.92	9.15[−11]	2.92	2.50[−3]
	5.00	4.53[−20]	4.91	3.42[−12]
	7.02	1.99[−28]	6.92	1.83[−20]
	9.03	5.58[−37]	8.92	4.07[−29]
1×10^{15}	2.92	7.07[−8]	2.92	2.41[−3]
	5.00	6.62[−15]	4.93	3.39[−10]
	7.00	3.10[−21]	6.93	1.82[−16]
	9.01	6.00[−28]	8.92	3.99[−23]
	11.02	5.45[−35]	10.92	4.04[−30]
2.5×10^{15}	2.92	1.33[−6]	2.92	2.01[−3]
	5.00	1.28[−12]	4.94	2.07[−9]
	7.00	4.13[−18]	6.95	6.82[−15]
	9.01	5.30[−24]	8.95	9.40[−21]
	11.00	3.14[−30]	10.95	5.95[−27]
	13.03	1.05[−36]	12.95	1.96[−33]

Chapter 5

Generalized Floquet approach for the exploration of multiphoton quantum interference in a superconducting qubit driven by intense ac fields

We present a Floquet treatment of multiphoton phenomena in a strongly driven superconducting flux qubit. The periodically time-dependent Schrödinger equation can be reduced to an equivalent time-independent infinite-dimensional Floquet matrix eigenvalue problem. For resonant or nearly resonant multiphoton transitions, we extend the generalized Van Vleck (GVV) nearly degenerate high-order perturbation theory for the treatment of the Floquet Hamiltonian. The GVV approach allows accurate treatment of ac Stark shift, power broadening, time-dependent and time-averaged transition probability, etc., well beyond the rotating wave approximation. We extend the Floquet and GVV approaches for numerical and analytical studies of the multiphoton resonance

processes and quantum interference phenomena for the superconducting flux qubit system driven by intense ac fields.

5.1 Superconducting flux qubit

Superconducting flux qubit [222] is a promising candidate for quantum computing [4]. When the superconducting flux qubit is driven by an oscillating field, it involves plentiful dynamics of macroscopic quantum states such as Rabi oscillations and coherent control [223, 224, 225]. Recently, Oliver and colleagues experimentally demonstrated multiphoton resonance and quantum interference in a strongly driven flux qubit as an analogue of Mach–Zehnder interferometry [226, 227]. The peaks in the transition probability between two qubit states form fringe patterns around multiphoton resonance positions. This is explained by the phase differences of the qubit states after they are swept by a strong driving field [226]. Since the strongly driven qubit can be modeled by a two-level system interacting with the strong oscillating field, the development of an analytical approach for a time-dependent problem is desirable to explore the rich dynamics of the two-level system. Understanding dynamics of strongly driven two-level systems is important to superconducting approach of quantum computation.

The two-level system interacting with the external field through off-diagonal time-dependent couplings (transverse couplings) has been extensively studied in the framework of the Floquet theory [28, 221, 228]. On the contrary, the qubit that is the two-level system interacting through diagonal couplings (longitudinal couplings) with driving fields has been investigated only within the rotating wave approximation (RWA) [226, 229]. RWA includes only one resonant

term, whereas the generalized Van Vleck (GVV) nearly degenerate perturbation theory [230, 231, 232] includes all leading terms that result in the ac Stark level shift and power broadening of multiphoton resonance positions [220, 228]. Recently, Ashhab et al. [233] have studied the two-level system within RWA and the transfer-matrix approach, and Greenberg [234] and Wilson et al. [235] have studied the qubit using the dressed-state approach. However, to the best of our knowledge, the ac Stark level shift for multiphoton resonance processes which appears beyond RWA has not been considered so far for this qubit system. As to be shown later, the consideration of level shift and power broadening is significant for quantitative exploration of multiphoton quantum interference phenomena in the superconducting qubit. We extend the Floquet theory for a comprehensive investigation of the strongly driven qubit system and provide insightful GVV analytic solutions to better understand multiphoton resonance condition including the level shift and coherent quantum interference patterns.

The superconducting flux qubit discussed here is a compound Josephson junction (CJJ) radio-frequency superconducting quantum interference device (rf SQUID) [236], which consists of a main loop and a CJJ loop subjected to external flux biases Φ_x and Φ_x^{CJJ}, respectively, as shown in Fig. 5.1. The Hamiltonian of the CJJ rf SQUID can be approximated by a double-well potential as a function of the total flux threading the main loop. Two logical qubit states are assigned to the opposite circulation direction of persistent currents in the loop. The clockwise current corresponds to $|\alpha\rangle$, while the counterclockwise to $|\beta\rangle$. If the temperature is much less than the small oscillation frequency (i.e., the plasma frequency) at the bottom of the double-well potential, the superconduct-

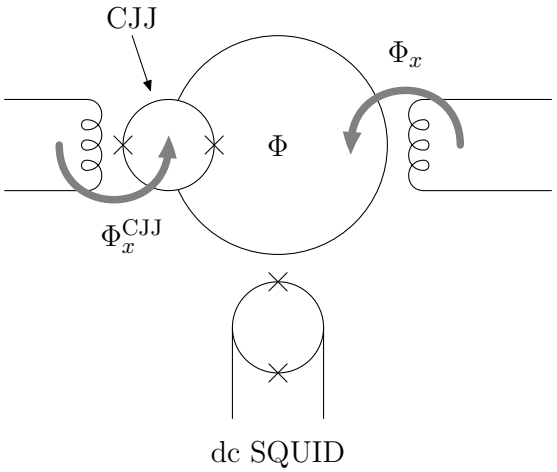

Figure 5.1: Schematic diagram for a combined Josephson junction rf SQUID.

ing flux qubit can be described by a 2×2 effective Hamiltonian matrix [237],

$$H_0 = -\frac{1}{2}\begin{pmatrix} \varepsilon_0 & \Delta \\ \Delta & -\varepsilon_0 \end{pmatrix}, \tag{5.1}$$

where Δ is called the tunnel splitting and ε_0 is the detuning energy proportional to both the persistent current and the flux detuning from the external flux bias. Note that Eq. (5.1) is obtained using the two logic states of the qubit, $|\alpha\rangle = (\ 1\ 0\ )^T$ and $|\beta\rangle = (\ 0\ 1\ )^T$, as the bases. Figure 5.2 shows the eigenvalues of Eq. (5.1), $E = \pm\sqrt{\varepsilon_0^2 + \Delta^2}/2$, as a function of the detuning energy ε_0. A positive slope of the dispersion curve corresponds to $|\beta\rangle$ (counterclockwise), while a negative slope to $|\alpha\rangle$ (clockwise). These two states are coupled through the tunneling strength Δ and show the avoided crossing at $\varepsilon_0 = 0$ as shown in Fig. 5.2. Thus, Δ is given by the energy separation of two eigenstates of H_0 at $\varepsilon_0 = 0$ which are $(|\alpha\rangle - |\beta\rangle)/\sqrt{2}$ and $(|\alpha\rangle + |\beta\rangle)/\sqrt{2}$. Both the persistent current and the tunneling strength are controlling parameters of the qubit states. When the qubit becomes localized in $|\alpha\rangle$ or $|\beta\rangle$, the persistent current generates

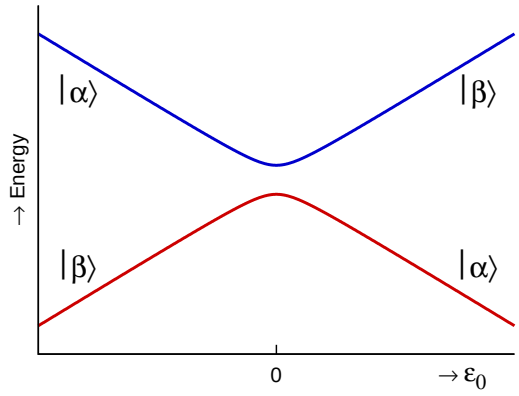

Figure 5.2: Energy diagram for a superconducting flux qubit.

a magnetic flux that can be detected by an inductively coupled dc SQUID as described in Ref. [236].

5.2 Floquet formulation for the superconducting flux qubit

The generalized Floquet formalisms [28] have been developed and applied to a number of time-dependent problems: from monochromatic to polychromatic [217] and frequency-comb laser fields [54], and from two-level models to realistic atomic and molecular systems [28, 32, 238, 239] and the electron transport of nanoscale systems [240]. It provides a non-perturbative and accurate treatment of the interaction of a quantum system with intense time-dependent fields.

When the superconducting flux qubit is driven by a strong ac field, the time-dependent Hamiltonian [226] is given as

$$H(t) = -\frac{1}{2}\begin{pmatrix} \varepsilon(t) & \Delta \\ \Delta & -\varepsilon(t) \end{pmatrix}, \tag{5.2}$$

where $\varepsilon(t) = \varepsilon_0 + A\cos\omega t$. Note that for typical superconducting flux qubits the longitudinal coupling is more commonly used than the transverse coupling. ω is the angular frequency of the driving ac field and A is its amplitude that is parametrized in the energy unit and proportional to ac flux bias [227]. Note that this Hamiltonian generally describes the two-level system interacting through the longitudinal coupling and is directly applicable to other qubit systems. For example, in Cooper-pair box qubits [235] the electrostatic energy and the Josephson coupling energy directly correspond to ε_0 and Δ in Eq. (5.2), respectively.

The generalized Floquet theory [28] provides an exact formulation of time-periodic problems and a combined picture of the N-level system and electromagnetic fields by the use of quasienergy states. According to the Floquet theorem [241], the time-dependent Schrödinger equation with a given time-periodic Hamiltonian,

$$i\hbar\frac{\partial}{\partial t}\psi(t) = H(t)\psi(t), \tag{5.3}$$

has a solution that can be written as

$$\psi(t) = e^{-iqt/\hbar}\phi(t), \tag{5.4}$$

where $\phi(t)$ is periodic in time and q is called the quasienergy. When Eq. (5.4) is substituted into Eq. (5.3), we obtain an eigenvalue equation for the quasienergy,

$$\left[H(t) - i\hbar\frac{\partial}{\partial t}\right]\phi(t) = q\phi(t). \tag{5.5}$$

The periodically time-dependent problem can be transformed into an equivalent time-independent infinite-dimensional generalized Floquet matrix eigen-

value problem [28, 221]. The temporal part of the Hamiltonian $H(t)$ and the quasi-energy eigenfunction $\phi(t)$ is expanded with the Fourier components of ω,

$$H(t) = \sum_n H^{[n]} e^{-in\omega t}, \tag{5.6}$$

$$\phi(t) = \sum_n \phi^{[n]} e^{-in\omega t}, \tag{5.7}$$

where $H^{[n]}$ and $\phi^{[n]}$ are spanned by any orthonormal basis set. We can employ the Floquet-state nomenclature [28],

$$|\alpha n\rangle = |\alpha\rangle \otimes |n\rangle, \tag{5.8}$$

where α is the system index and n is the Fourier index that runs from $-\infty$ to ∞. Note that in the generalized Floquet formalism α can be the N-level system index, but for the effective Hamiltonian of Eq. (5.2) it is restricted to the qubit state (N=2). Substituting Eqs. (5.6) and (5.7) into Eq. (5.5) and employing Eq. (5.8), we obtain the following time-independent Floquet matrix eigenvalue equation,

$$\sum_\beta \sum_m \langle \alpha n|H_F|\beta m\rangle \langle \beta m|q_{\gamma l}\rangle = q_{\gamma l}\langle \alpha n|q_{\gamma l}\rangle, \tag{5.9}$$

where $q_{\gamma l}$ is the quasienergy eigenvalue and $|q_{\gamma l}\rangle$ is the corresponding eigenvector, $\langle \alpha n|q_{\gamma l}\rangle = \phi_{\alpha\gamma}^{[n-l]}$. Here, H_F is the time-independent Floquet Hamiltonian defined by

$$\langle \alpha n|H_F|\beta m\rangle = H_{\alpha\beta}^{[n-m]} + n\hbar\omega\delta_{\alpha\beta}\delta_{nm}. \tag{5.10}$$

For simplicity, we set $\hbar = 1$ hereafter.

The time-dependent Hamiltonian for the superconducting flux qubit in Eq. (5.2) is expanded with the Fourier components of ω,

$$H(t) = H_0 - \frac{A\cos\omega t}{2}\begin{pmatrix} 1 & 0 \\ 0 & -1 \end{pmatrix} = H_0 - \frac{A(e^{i\omega t} + e^{-i\omega t})}{4}\begin{pmatrix} 1 & 0 \\ 0 & -1 \end{pmatrix}. \quad (5.11)$$

By comparing Eq. (5.6), there are only three non-vanishing Fourier components:

$$H^{[0]} = -\frac{1}{2}\begin{pmatrix} \varepsilon_0 & \Delta \\ \Delta & -\varepsilon_0 \end{pmatrix},\ H^{[+1]} = -\frac{A}{4}\begin{pmatrix} 1 & 0 \\ 0 & -1 \end{pmatrix},\ \text{and } H^{[-1]} = -\frac{A}{4}\begin{pmatrix} 1 & 0 \\ 0 & -1 \end{pmatrix}, \quad (5.12)$$

where $H^{[n-m]} + n\omega\delta_{nm}I$ (I: 2×2 identity matrix) forms the nth column and the mth row of the Floquet blocks.

Here we employ the Floquet-state nomenclature in Eq. (5.8),

$$|\alpha n\rangle = |\alpha\rangle \otimes |n\rangle, \quad (5.13)$$

where α is the system index (α or β) and n is the Fourier index ($-\infty < n < \infty$). Then we construct the matrix eigenvalue equation,

$$\sum_{\beta}\sum_{m}\langle \alpha n|H_F|\beta m\rangle\langle \beta m|q_{\gamma l}\rangle = q_{\gamma l}\langle \alpha n|q_{\gamma l}\rangle, \quad (5.14)$$

where H_F is the time-independent Floquet matrix, $q_{\gamma l}$ is the quasienergy eigenvalue, and $|q_{\gamma l}\rangle$ is the corresponding eigenvector.

The Floquet matrix H_F for the qubit represented by bases of $|\alpha n\rangle$ and $|\beta m\rangle$ according to Eq. (5.10) is given as follows:

$$
H_F = \begin{pmatrix}
\ddots & & & & & & & & & & \\
 & -\frac{\varepsilon_0}{2}-2\omega & -\frac{\Delta}{2} & -\frac{A}{4} & 0 & 0 & 0 & 0 & 0 & 0 & \leftarrow |\alpha,-2\rangle \\
 & -\frac{\Delta}{2} & \frac{\varepsilon_0}{2}-2\omega & 0 & \frac{A}{4} & 0 & 0 & 0 & 0 & 0 & \leftarrow |\beta,-2\rangle \\
 & -\frac{A}{4} & 0 & -\frac{\varepsilon_0}{2}-\omega & -\frac{\Delta}{2} & -\frac{A}{4} & 0 & 0 & 0 & 0 & \leftarrow |\alpha,-1\rangle \\
 & 0 & \frac{A}{4} & -\frac{\Delta}{2} & \frac{\varepsilon_0}{2}-\omega & 0 & \frac{A}{4} & 0 & 0 & 0 & 0 & \leftarrow |\beta,-1\rangle \\
\cdots & 0 & 0 & -\frac{A}{4} & 0 & -\frac{\varepsilon_0}{2} & -\frac{\Delta}{2} & -\frac{A}{4} & 0 & 0 & 0 & \cdots & \leftarrow |\alpha,0\rangle \\
 & 0 & 0 & 0 & \frac{A}{4} & -\frac{\Delta}{2} & \frac{\varepsilon_0}{2} & 0 & \frac{A}{4} & 0 & 0 & & \leftarrow |\beta,0\rangle \\
 & 0 & 0 & 0 & 0 & -\frac{A}{4} & 0 & -\frac{\varepsilon_0}{2}+\omega & -\frac{\Delta}{2} & -\frac{A}{4} & 0 & & \leftarrow |\alpha,+1\rangle \\
 & 0 & 0 & 0 & 0 & 0 & \frac{A}{4} & -\frac{\Delta}{2} & \frac{\varepsilon_0}{2}+\omega & 0 & \frac{A}{4} & & \leftarrow |\beta,+1\rangle \\
 & 0 & 0 & 0 & 0 & 0 & 0 & -\frac{A}{4} & 0 & -\frac{\varepsilon_0}{2}+2\omega & -\frac{\Delta}{2} & & \leftarrow |\alpha,+2\rangle \\
 & 0 & 0 & 0 & 0 & 0 & 0 & 0 & \frac{A}{4} & -\frac{\Delta}{2} & \frac{\varepsilon_0}{2}+2\omega & & \leftarrow |\beta,+2\rangle \\
 & & & & & & & & & & \ddots &
\end{pmatrix}
$$

$$
\begin{array}{cccccccccc}
\uparrow & \uparrow & \uparrow & \uparrow & \uparrow & \uparrow & \uparrow & \uparrow & \uparrow & \uparrow \\
|\alpha,-2\rangle & |\beta,-2\rangle & |\alpha,-1\rangle & |\beta,-1\rangle & |\alpha,0\rangle & |\beta,0\rangle & |\alpha,+1\rangle & |\beta,+1\rangle & |\alpha,+2\rangle & |\beta,+2\rangle
\end{array}
\tag{5.15}
$$

Eigenvalues of this Floquet matrix are numerically solved by truncating the number of the Floquet blocks. For numerical solutions in Section 5.4, 101 Floquet blocks ($n = -50 \sim 50$) are included to be sufficiently converged for multiphoton processes. It is worthwhile to note that there has been no approximation made in Eq. (5.15) to solve the time-dependent Hamiltonian of Eq. (5.2). Therefore, Eq. (5.15) can be applied for all parameter regimes.

After solving eigenvectors of the Floquet matrix, the time-averaged transition probability between $|\alpha\rangle$ and $|\beta\rangle$ can be computed by

$$\bar{P}_{\alpha\to\beta} = \sum_{n}\sum_{\gamma l} \left|\langle \beta n|q_{\gamma l}\rangle\langle q_{\gamma l}|\alpha 0\rangle\right|^2, \tag{5.16}$$

which is corresponding to the probability of finding the excited state of the qubit in experiment.

5.3 Analytic solution of the Floquet matrix for the driven qubit

To solve the Floquet matrix of Eq. (5.15) analytically, we employ the generalized Van Vleck (GVV) nearly degenerate perturbation theory [230, 231, 232]. By introducing a perturbation parameter, $\lambda = -\Delta/2$, the Floquet matrix can be divided into unperturbed and perturbed parts,

$$H_F = H_0 + \lambda V, \tag{5.17}$$

where H_0 has the following matrix structure,

$$
H_0 = \begin{pmatrix}
\ddots & & & & \vdots & & & & & \\
 & -\frac{\varepsilon_0}{2}-2\omega & 0 & -\frac{A}{4} & 0 & 0 & 0 & 0 & 0 & 0 \\
 & 0 & \frac{\varepsilon_0}{2}-2\omega & 0 & \frac{A}{4} & 0 & 0 & 0 & 0 & 0 \\
 & -\frac{A}{4} & 0 & -\frac{\varepsilon_0}{2}-\omega & 0 & -\frac{A}{4} & 0 & 0 & 0 & 0 \\
 & 0 & \frac{A}{4} & 0 & \frac{\varepsilon_0}{2}-\omega & 0 & \frac{A}{4} & 0 & 0 & 0 \\
\cdots & 0 & 0 & -\frac{A}{4} & 0 & -\frac{\varepsilon_0}{2} & 0 & -\frac{A}{4} & 0 & 0 \\
 & 0 & 0 & 0 & \frac{A}{4} & 0 & \frac{\varepsilon_0}{2} & 0 & \frac{A}{4} & 0 \\
 & 0 & 0 & 0 & 0 & -\frac{A}{4} & 0 & -\frac{\varepsilon_0}{2}+\omega & 0 & -\frac{A}{4} \\
 & 0 & 0 & 0 & 0 & 0 & \frac{A}{4} & 0 & \frac{\varepsilon_0}{2}+\omega & 0 \\
 & 0 & 0 & 0 & 0 & 0 & 0 & -\frac{A}{4} & 0 & -\frac{\varepsilon_0}{2}+2\omega \\
 & 0 & 0 & 0 & 0 & 0 & 0 & 0 & \frac{A}{4} & 0 \\
 & & & & \vdots & & & & & \ddots
\end{pmatrix}
\begin{matrix}
 \\
\leftarrow |\alpha,-2\rangle \\
\leftarrow |\beta,-2\rangle \\
\leftarrow |\alpha,-1\rangle \\
\leftarrow |\beta,-1\rangle \\
\leftarrow |\alpha,0\rangle \\
\leftarrow |\beta,0\rangle \\
\leftarrow |\alpha,+1\rangle \\
\leftarrow |\beta,+1\rangle \\
\leftarrow |\alpha,+2\rangle \\
\leftarrow |\beta,+2\rangle \\

\end{matrix}
\begin{matrix}
 \\
 \\
 \\
 \\
 \\
\cdots \\
 \\
 \\
 \\
 \\
 \\

\end{matrix}
.
$$

$$
\begin{matrix}
\uparrow & \uparrow & \uparrow & \uparrow & \uparrow & \uparrow & \uparrow & \uparrow & \uparrow & \uparrow \\
|\alpha,-2\rangle & |\beta,-2\rangle & |\alpha,-1\rangle & |\beta,-1\rangle & |\alpha,0\rangle & |\beta,0\rangle & |\alpha,+1\rangle & |\beta,+1\rangle & |\alpha,+2\rangle & |\beta,+2\rangle
\end{matrix}
$$

(5.18)

To obtain the eigenstates of H_0, Eq. (5.18) can be separated into two segments because all off-diagonals are zero in each 2×2 block, i.e., $|\alpha\rangle$ and $|\beta\rangle$ are decoupled in H_0,

$$H_0(\alpha \text{ or } \beta) = \begin{pmatrix} \ddots & & & \vdots & & & \\ & b-2\omega & a & 0 & 0 & 0 & \\ & a & b-\omega & a & 0 & 0 & \\ \cdots & 0 & a & b & a & 0 & \cdots \\ & 0 & 0 & a & b+\omega & a & \\ & 0 & 0 & 0 & a & b+2\omega & \\ & & & \vdots & & & \ddots \end{pmatrix}, \tag{5.19}$$

where $b = -\varepsilon_0/2$ and $a = -A/4$ for the state of $|\alpha\rangle$, and $b = +\varepsilon_0/2$ and $a = +A/4$ for $|\beta\rangle$. Eigenvalues and eigenvectors of Eq. (5.19) can be analytically solved in terms of Bessel functions $J_k(x)$ as follows.

The infinite-dimensional tridiagonal matrix in Eq. (5.19) can be considered as a Floquet matrix transformed from a function $h(t) = b + 2a\cos\omega t$ with Fourier bases of $|k\rangle$ (k is an integer), where a and b are given numbers. After an inverse transformation, the original equation to be solved is the following eigenvalue problem,

$$\left[h(t) - i\frac{\partial}{\partial t}\right]\phi(t) = \lambda\phi(t). \tag{5.20}$$

A trivial solution is $\lambda = b$. Its eigenfunction is given by a Fourier expansion with Bessel functions [242],

$$\phi(t) = e^{-i\frac{2a}{\omega}\sin\omega t} = \sum_{k=-\infty}^{\infty} J_k\left(-\frac{2a}{\omega}\right)e^{ik\omega t}. \tag{5.21}$$

For eigenvalues of $\lambda_n = b + n\omega$ (n is an integer), $\phi_n(t)$ is solved as

$$\phi_n(t) = e^{in\omega t} e^{-i\frac{2a}{\omega}\sin\omega t} = \sum_{k=-\infty}^{\infty} J_k\left(-\frac{2a}{\omega}\right) e^{i(n+k)\omega t} = \sum_{k=-\infty}^{\infty} J_{k-n}\left(-\frac{2a}{\omega}\right) e^{ik\omega t}. \tag{5.22}$$

To summarize, eigenvalues and eigenvectors of Eq. (5.19) are

$$\text{Eigenvalues: } b + n\omega \quad (n\text{: any integer}), \tag{5.23a}$$

$$\text{Eigenvectors: } \phi_n = \sum_{k=-\infty}^{\infty} J_{k-n}\left(-\frac{2a}{\omega}\right) |k\rangle. \tag{5.23b}$$

Therefore, the eigenstates of H_0 in Eq. (5.18) are represented as follows,

$$|\alpha', n\rangle = \sum_{k=-\infty}^{\infty} J_{k-n}\left(\frac{A}{2\omega}\right) |\alpha k\rangle, \tag{5.24a}$$

$$|\beta', m\rangle = \sum_{k=-\infty}^{\infty} J_{k-m}\left(-\frac{A}{2\omega}\right) |\beta k\rangle. \tag{5.24b}$$

Since the GVV method requires the eigenstates for the unperturbed Hamiltonian, the Floquet matrix H_F in Eq. (5.15) needs to be rewritten in terms of the bases of $|\alpha', n\rangle$ and $|\beta', m\rangle$. Let $z = A/2\omega$ and $J'_k = J_k(A/\omega)$. From $\langle \alpha k|H_F|\beta l\rangle = -\frac{\Delta}{2}\delta_{kl}$ in Eq. (5.15) and the addition theorem for Bessel function $J_n(y+z) = \sum_m J_m(y) J_{n-m}(z)$ for any integer n [242], one can obtain

$$\begin{aligned}\langle \alpha', n|H_F|\beta', m\rangle &= \sum_{k=-\infty}^{\infty}\sum_{l=-\infty}^{\infty} J_{k-n}(z) J_{l-m}(-z) \langle \alpha k|H_F|\beta l\rangle \\ &= -\frac{\Delta}{2}\sum_{k=-\infty}^{\infty} J_{k-n}(z) J_{-k+m}(z) = -\frac{\Delta}{2} J_{m-n}(2z),\end{aligned} \tag{5.25}$$

$$\begin{aligned}\langle \beta', n|H_F|\alpha', m\rangle &= \sum_{k=-\infty}^{\infty}\sum_{l=-\infty}^{\infty} J_{k-n}(-z) J_{l-m}(z) \langle \beta k|H_F|\alpha l\rangle \\ &= -\frac{\Delta}{2}\sum_{k=-\infty}^{\infty} J_{-k+n}(z) J_{k-m}(z) = -\frac{\Delta}{2} J_{n-m}(2z).\end{aligned} \tag{5.26}$$

From $\langle \alpha k|H_F|\alpha l\rangle = \left(-\frac{\varepsilon_0}{2}+k\omega\right)\delta_{kl} - \frac{A}{4}\left(\delta_{k,l+1}+\delta_{k,l-1}\right)$ in Eq. (5.15), a recursive relation for Bessel function $J_{n-1}(z)+J_{n+1}(z) = \frac{2n}{z}J_n(z)$ [242], and summation of $\sum_m J_m(z)J_{m-n}(z) = \sum_m J_m(z)J_{-m+n}(-z) = J_n(0) = \delta_{n0}$ for any integer n, one can obtain

$$\begin{aligned}
\langle \alpha', n|H_F|\alpha', m\rangle &= \sum_{k=-\infty}^{\infty}\sum_{l=-\infty}^{\infty} J_{k-n}(z)J_{l-m}(z)\langle \alpha k|H_F|\alpha l\rangle \\
&= \sum_{k=-\infty}^{\infty} J_{k-n}(z)\left[\left(-\frac{\varepsilon_0}{2}+k\omega\right)J_{k-m}(z) - \frac{A}{4}\left\{J_{k-m-1}(z)+J_{k-m+1}(z)\right\}\right] \\
&= \sum_{k=-\infty}^{\infty} J_{k-n}(z)\left[-\frac{\varepsilon_0}{2}+k\omega-(k-m)\omega\right]J_{k-m}(z) \\
&= \left(-\frac{\varepsilon_0}{2}+m\omega\right)\sum_{k=-\infty}^{\infty} J_{k-n}(z)J_{k-m}(z) \\
&= \left(-\frac{\varepsilon_0}{2}+n\omega\right)\delta_{nm}. \qquad (5.27)
\end{aligned}$$

Likewise, from $\langle \beta k|H_F|\beta l\rangle = \left(\frac{\varepsilon_0}{2}+k\omega\right)\delta_{kl} + \frac{A}{4}\left(\delta_{k,l+1}+\delta_{k,l-1}\right)$,

$$\langle \beta', n|H_F|\beta', m\rangle = \left(\frac{\varepsilon_0}{2}+n\omega\right)\delta_{nm}. \qquad (5.28)$$

Therefore, with equations from (5.25) to (5.28) the Floquet matrix is now represented by the bases of $|\alpha', n\rangle$ and $|\beta', m\rangle$ as follows:

$$
H'_F = \begin{pmatrix}
\ddots & & \vdots & & & & & & & & \iddots \\
 & -\frac{\varepsilon_0}{2}-2\omega & -\frac{\Delta}{2}J'_0 & 0 & -\frac{\Delta}{2}J'_1 & 0 & -\frac{\Delta}{2}J'_2 & 0 & -\frac{\Delta}{2}J'_3 & 0 & -\frac{\Delta}{2}J'_4 & \leftarrow & |\alpha',-2\rangle \\
 & -\frac{\Delta}{2}J'_0 & \frac{\varepsilon_0}{2}-2\omega & -\frac{\Delta}{2}J'_{-1} & 0 & -\frac{\Delta}{2}J'_{-2} & 0 & -\frac{\Delta}{2}J'_{-3} & 0 & -\frac{\Delta}{2}J'_{-4} & 0 & \leftarrow & |\beta',-2\rangle \\
\hline
 & 0 & -\frac{\Delta}{2}J'_{-1} & -\frac{\varepsilon_0}{2}-\omega & -\frac{\Delta}{2}J'_0 & 0 & -\frac{\Delta}{2}J'_1 & 0 & -\frac{\Delta}{2}J'_2 & 0 & -\frac{\Delta}{2}J'_3 & \leftarrow & |\alpha',-1\rangle \\
 & -\frac{\Delta}{2}J'_1 & 0 & -\frac{\Delta}{2}J'_0 & \frac{\varepsilon_0}{2}-\omega & -\frac{\Delta}{2}J'_{-1} & 0 & -\frac{\Delta}{2}J'_{-2} & 0 & -\frac{\Delta}{2}J'_{-3} & 0 & \leftarrow & |\beta',-1\rangle \\
\hline
 & 0 & -\frac{\Delta}{2}J'_{-2} & 0 & -\frac{\Delta}{2}J'_{-1} & -\frac{\varepsilon_0}{2} & -\frac{\Delta}{2}J'_0 & 0 & -\frac{\Delta}{2}J'_1 & 0 & -\frac{\Delta}{2}J'_2 & \leftarrow & |\alpha',0\rangle \\
\cdots & -\frac{\Delta}{2}J'_2 & 0 & -\frac{\Delta}{2}J'_1 & 0 & -\frac{\Delta}{2}J'_0 & \frac{\varepsilon_0}{2} & -\frac{\Delta}{2}J'_{-1} & 0 & -\frac{\Delta}{2}J'_{-2} & 0 & \leftarrow & |\beta',0\rangle \\
\hline
 & 0 & -\frac{\Delta}{2}J'_{-3} & 0 & -\frac{\Delta}{2}J'_{-2} & 0 & -\frac{\Delta}{2}J'_{-1} & -\frac{\varepsilon_0}{2}+\omega & -\frac{\Delta}{2}J'_0 & 0 & -\frac{\Delta}{2}J'_1 & \leftarrow & |\alpha',+1\rangle \\
 & -\frac{\Delta}{2}J'_3 & 0 & -\frac{\Delta}{2}J'_2 & 0 & -\frac{\Delta}{2}J'_1 & 0 & -\frac{\Delta}{2}J'_0 & \frac{\varepsilon_0}{2}+\omega & -\frac{\Delta}{2}J'_{-1} & 0 & \leftarrow & |\beta',+1\rangle \\
\hline
 & 0 & -\frac{\Delta}{2}J'_{-4} & 0 & -\frac{\Delta}{2}J'_{-3} & 0 & -\frac{\Delta}{2}J'_{-2} & 0 & -\frac{\Delta}{2}J'_{-1} & -\frac{\varepsilon_0}{2}+2\omega & -\frac{\Delta}{2}J'_0 & \leftarrow & |\alpha',+2\rangle \\
 & -\frac{\Delta}{2}J'_4 & 0 & -\frac{\Delta}{2}J'_3 & 0 & -\frac{\Delta}{2}J'_2 & 0 & -\frac{\Delta}{2}J'_1 & 0 & -\frac{\Delta}{2}J'_0 & \frac{\varepsilon_0}{2}+2\omega & \leftarrow & |\beta',+2\rangle \\
\iddots & & \vdots & & & & & & & & \ddots & &
\end{pmatrix}
$$

$$
\begin{array}{cccccccccc}
\uparrow & \uparrow & \uparrow & \uparrow & \uparrow & \uparrow & \uparrow & \uparrow & \uparrow & \uparrow \\
|\alpha',-2\rangle & |\beta',-2\rangle & |\alpha',-1\rangle & |\beta',-1\rangle & |\alpha',0\rangle & |\beta',0\rangle & |\alpha',+1\rangle & |\beta',+1\rangle & |\alpha',+2\rangle & |\beta',+2\rangle
\end{array}
$$

(5.29)

From the matrix structure of Eq. (5.29), one can see that $|\alpha', 0\rangle$ is coupled to $|\beta', -n\rangle$ throughout an off-diagonal term of $-\frac{\Delta}{2}J'_{-n}$. When the Floquet states $|\alpha', 0\rangle$ and $|\beta', -n\rangle$ are nearly degenerate, namely, $-\varepsilon_0/2 \approx \varepsilon_0/2 - n\omega$, Eq. (5.29) is reduced to a 2×2 matrix by neglecting all other coupling terms except the one between $|\alpha', 0\rangle$ and $|\beta', -n\rangle$,

$$H_{\mathrm{RWA}} = \begin{pmatrix} -\frac{\varepsilon_0}{2} & -\frac{\Delta}{2}J'_{-n} \\ -\frac{\Delta}{2}J'_{-n} & \frac{\varepsilon_0}{2} - n\omega \end{pmatrix}. \tag{5.30}$$

This is equivalent to the rotating wave approximation (RWA), whose form is identical to previous works used for the superconducting qubit subject to the longitudinal coupling [226, 229, 233]. Note that this RWA is different from conventional one subject to the transverse coupling, where RWA breaks down in the strong field [228].

To go beyond RWA, we extend the GVV method allowing the reduction of the infinite-dimensional H'_F into a 2×2 effective Hamiltonian which includes all n-photon coupling channels. With the perturbation parameter $\lambda = -\Delta/2$, the Floquet matrix of Eq. (5.29) is divided into

$$H'_F = H'_0 + \lambda V', \tag{5.31}$$

where

$$H_0' = \left(\begin{array}{cccccc|cccccc|c} \ddots & & & & & & \vdots & & & & & & \\ & -\frac{\varepsilon_0}{2}-\omega & 0 & 0 & 0 & 0 & 0 & & & & & & \\ & 0 & \frac{\varepsilon_0}{2}-\omega & 0 & 0 & 0 & 0 & & & & & & \\ \hline \cdots & 0 & 0 & -\frac{\varepsilon_0}{2} & 0 & 0 & 0 & & & & & & \cdots \\ & 0 & 0 & 0 & \frac{\varepsilon_0}{2} & 0 & 0 & & & & & & \\ \hline & 0 & 0 & 0 & 0 & -\frac{\varepsilon_0}{2}+\omega & 0 & & & & & & \\ & 0 & 0 & 0 & 0 & 0 & \frac{\varepsilon_0}{2}+\omega & & & & & & \\ & & & & & & \vdots & & & & & & \ddots \end{array}\right), \tag{5.32}$$

and

$$V' = \left(\begin{array}{cccccc|cccccc|c} \ddots & & & & & & \vdots & & & & & & \iddots \\ & 0 & J_0' & 0 & J_1' & 0 & J_2' & & & & & & \\ & J_0' & 0 & J_{-1}' & 0 & J_{-2}' & 0 & & & & & & \\ \hline \cdots & 0 & J_{-1}' & 0 & J_0' & 0 & J_1' & & & & & & \cdots \\ & J_1' & 0 & J_0' & 0 & J_{-1}' & 0 & & & & & & \\ \hline & 0 & J_{-2}' & 0 & J_{-1}' & 0 & J_0' & & & & & & \\ & J_2' & 0 & J_1' & 0 & J_0' & 0 & & & & & & \\ \iddots & & & & & & \vdots & & & & & & \ddots \end{array}\right). \tag{5.33}$$

The aim is to reduce the infinite-dimensional Floquet matrix of Eq. (5.29) into the 2×2 matrix. According to the nearly degenerate perturbation formalism in the GVV method [230, 231, 232], the 2×2 matrix $\mathbf{h}$ and its eigenstate solution $\boldsymbol{\phi}$ can be expanded in powers of λ,

$$\mathbf{h} = \sum_{m=0}^{\infty} \lambda^m \mathbf{h}^{(m)}, \tag{5.34}$$

$$\boldsymbol{\phi} = \sum_{m=0}^{\infty} \lambda^m \boldsymbol{\phi}^{(m)}. \tag{5.35}$$

For n-photon resonance, the Floquet states $|\alpha', 0\rangle$ and $|\beta', -n\rangle$ are nearly degenerate. Thus, the zeroth-order $\boldsymbol{\phi}^{(0)} = (\ \phi_-^{(0)}\ \phi_+^{(0)}\ )^T$ is given by

$$\phi_-^{(0)} = |\alpha', 0\rangle \quad \text{and} \quad \phi_+^{(0)} = |\beta', -n\rangle. \tag{5.36}$$

The zeroth-order $\mathbf{h}^{(0)}$ represented by $\phi_-^{(0)}$ and $\phi_+^{(0)}$ is given by

$$\mathbf{h}^{(0)} = \begin{pmatrix} -\frac{\varepsilon_0}{2} & 0 \\ 0 & \frac{\varepsilon_0}{2} - n\omega \end{pmatrix}, \tag{5.37}$$

where two eigenstates are nearly degenerate, i.e., $\varepsilon_0 \approx n\omega$. Following the GVV method, a few high-order terms can be computed as follows:

$$\phi_-^{(1)} = \sum_{\substack{k=-\infty \\ k\neq -n}}^{\infty} \frac{-J'_k}{\varepsilon_0 + k\omega} |\beta', k\rangle, \ \text{ and } \ \phi_+^{(1)} = \sum_{\substack{k=-\infty \\ k\neq -n}}^{\infty} \frac{J'_k}{\varepsilon_0 + k\omega} |\alpha', -n-k\rangle, \tag{5.38}$$

$$\mathbf{h}^{(1)} = \langle \boldsymbol{\phi}^{(0)} | V' | \boldsymbol{\phi}^{(0)} \rangle = J'_{-n} \begin{pmatrix} 0 & 1 \\ 1 & 0 \end{pmatrix}, \tag{5.39}$$

$$\mathbf{h}^{(2)} = \langle \boldsymbol{\phi}^{(0)} | V' | \boldsymbol{\phi}^{(1)} \rangle - \mathbf{h}^{(1)} \langle \boldsymbol{\phi}^{(0)} | \boldsymbol{\phi}^{(1)} \rangle = \sum_{\substack{k=-\infty \\ k\neq -n}}^{\infty} \frac{J'^2_k}{\varepsilon_0 + k\omega} \begin{pmatrix} -1 & 0 \\ 0 & 1 \end{pmatrix}, \tag{5.40}$$

$$\begin{aligned} \mathbf{h}^{(3)} &= \langle \boldsymbol{\phi}^{(1)} | V' | \boldsymbol{\phi}^{(1)} \rangle - \langle \boldsymbol{\phi}^{(1)} | \boldsymbol{\phi}^{(1)} \rangle \mathbf{h}^{(1)} \\ &= -\sum_{\substack{k=-\infty \\ k\neq -n}}^{\infty} \left[\sum_{\substack{l=-\infty \\ l\neq -n}}^{\infty} \frac{J'_k J'_l J'_{k+l+n}}{(\varepsilon_0 + k\omega)(\varepsilon_0 + l\omega)} + \frac{J'^2_k J'_{-n}}{(\varepsilon_0 + k\omega)^2} \right] \begin{pmatrix} 0 & 1 \\ 1 & 0 \end{pmatrix}. \end{aligned} \tag{5.41}$$

After adding these higher-order terms, one can obtain the 2×2 matrix as,

$$H_{\mathrm{GVV}} = \begin{pmatrix} -\frac{\varepsilon_0}{2} + \delta & u \\ u & \frac{\varepsilon_0}{2} - \delta - n\omega \end{pmatrix}, \tag{5.42}$$

where δ is the ac Stark level shift and u is the non-vanishing off-diagonal term which is related to the power broadening of the transition probability peaks,

$$u = J'_{-n}\lambda - \sum_{\substack{k=-\infty \\ k\neq -n}}^{\infty} \left[\sum_{\substack{l=-\infty \\ l\neq -n}}^{\infty} \frac{J'_k J'_l J'_{k+l+n}}{(\varepsilon_0 + k\omega)(\varepsilon_0 + l\omega)} + \frac{J'^2_k J'_{-n}}{(\varepsilon_0 + k\omega)^2} \right] \lambda^3 + O(\lambda^5), \tag{5.43}$$

$$\delta = -\sum_{\substack{k=-\infty \\ k\neq -n}}^{\infty} \frac{J'^2_k}{\varepsilon_0 + k\omega}\lambda^2 + O(\lambda^4). \tag{5.44}$$

The leading term of u comes from the first-order in Eq. (5.39), and the leading term of λ is from the second-order in Eq. (5.40). In other words, most of dominant terms involving all multiphoton resonance processes are taken into account within the second-order perturbation of λ, in contrast to the conventional transverse coupling case that requires the $(2n+1)$th-order perturbation to obtain the non-vanishing terms for n-photon process [228]. If one considers the first-order term only, H_{GVV} is reduced to H_{RWA}. Note that Eqs. (5.42)–(5.44) are valid regardless of the strong or weak driving field amplitude A.

The effective Hamiltonian of Eq. (5.42) has the standard form for the two-level system in an oscillating field beyond RWA [28, 220, 221, 228]. Eigenvalues of Eq. (5.42) are given by

$$q_{\pm} = -\frac{n\omega}{2} \pm p, \tag{5.45}$$

where

$$p^2 = \frac{(n\omega - \varepsilon_0 + 2\delta)^2}{4} + u^2. \tag{5.46}$$

The n-photon time-dependent transition probability from $|\alpha\rangle$ to $|\beta\rangle$ is obtained by

$$P^{(n)}_{\alpha\to\beta}(t) = \frac{u^2}{p^2}\sin^2(pt), \tag{5.47}$$

and the n-photon time-averaged transition probability is obtained by

$$\bar{P}^{(n)}_{\alpha\to\beta} = \lim_{T\to\infty}\frac{1}{T}\int_0^T P^{(n)}_{\alpha\to\beta}(t)dt = \frac{1}{2}\cdot\frac{u^2}{u^2 + (n\omega - \varepsilon_0 + 2\delta)^2/4}. \tag{5.48}$$

With the first-order term only (RWA limit), it yields to

$$\bar{P}^{(n)}_{\alpha\to\beta} = \frac{1}{2}\cdot\frac{(\Delta J'_n)^2}{(\Delta J'_n)^2 + (n\omega - \varepsilon_0)^2}, \tag{5.49}$$

since $J_{-n}(x) = (-1)^n J_n(x)$. This RWA result is identical with previous formulation in Ref. [226]. Note that the first-order expression does not contain the level shift term.

Let us now investigate the behavior of the level shift δ in the weak and strong driving field regimes. The level shift is particularly important in qubit calibration because it determines the accurate positions of resonance peaks. From the second-order GVV in Eq. (5.44), δ is proportional to Δ^2 and given by the series with the Bessel function involving A as its argument. For small arguments ($x \ll 1$), the Bessel function has the following asymptotic form,

$$J_k(x) \approx \frac{1}{k!}\left(\frac{x}{2}\right)^k \quad (k \geq 0), \tag{5.50}$$

where $x = A/\omega$. Thus, in the weak-field regime, J'_0 is dominant over $J'_k(k \neq 0)$. When only J'_0 is included in the sum of Eq. (5.44), δ is approximated as

$$\delta = -\frac{\Delta^2}{4\varepsilon_0} + O(A^2, \Delta^4) \quad (n \geq 1). \tag{5.51}$$

For non-photon-assisted process ($n = 0$), there is no Δ^2 term in δ, i.e., $\delta \approx 0$ because J'_0 is excluded in the sum of Eq. (5.44). If we approximate δ up to $O(A^4)$, $J'_0(\approx 1 - A^2/4\omega^2)$ and $J'_{\pm 1}(\approx \pm A/2\omega)$ can be included in the sum of Eq. (5.44), which yields to

$$\delta = -\frac{A^2\Delta^2\varepsilon_0}{8\omega^2(\varepsilon_0^2 - \omega^2)} + O(A^4, \Delta^4) \qquad (n = 0) \tag{5.52a}$$

$$= -\frac{\Delta^2}{4\varepsilon_0} + \frac{A^2\Delta^2(\varepsilon_0 + 2\omega)}{16\omega^2\varepsilon_0(\varepsilon_0 + \omega)} + O(A^4, \Delta^4) \qquad (n = 1) \tag{5.52b}$$

$$= -\frac{\Delta^2}{4\varepsilon_0} - \frac{\Delta^2 A^2}{8\varepsilon_0(\varepsilon_0^2 - \omega^2)} + O(A^4, \Delta^4). \qquad (n \geq 2) \tag{5.52c}$$

On the other hand, for large arguments ($x \to \infty$), the Bessel function asymptotically becomes

$$J_k(x) \approx \sqrt{\frac{2}{\pi x}} \cos\left(x - \frac{k\pi}{2} - \frac{\pi}{4}\right), \tag{5.53}$$

and then J'^2_k is approximated as

$$J'^2_k \approx \frac{2\omega}{\pi A} \cos^2\left(\frac{A}{\omega} - \frac{k\pi}{2} - \frac{\pi}{4}\right) = \frac{\omega}{\pi A}\left\{1 + \cos\left(\frac{2A}{\omega} - k\pi - \frac{\pi}{2}\right)\right\}$$
$$= \frac{\omega}{\pi A}\left\{1 + (-1)^k \sin\left(\frac{2A}{\omega}\right)\right\}. \tag{5.54}$$

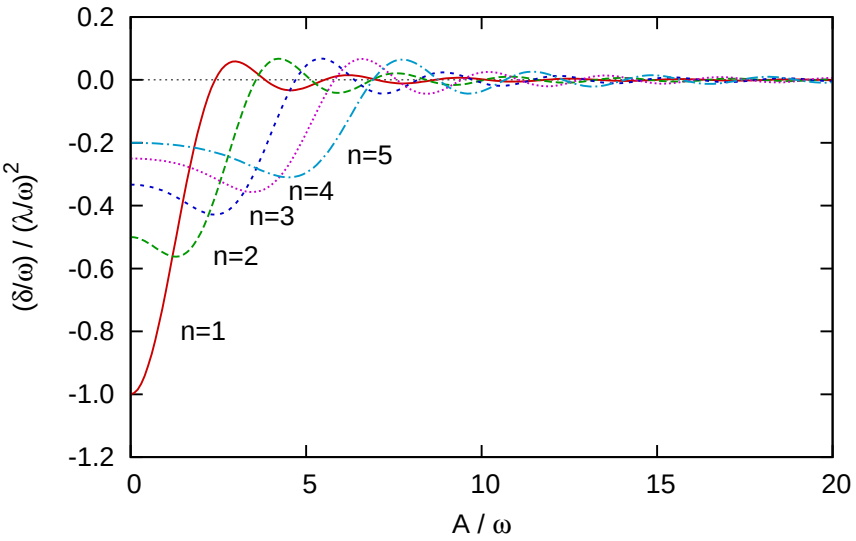

Figure 5.3: Plots of the level shift δ as a function of the field amplitude A.

Thus it yields to $J_k'^2 \approx J_{-k}'^2$. Using this asymptotic expression as well as $\varepsilon_0 \approx n\omega$, δ in the strong-field regime becomes zero as shown below:

$$\begin{aligned}\delta &\approx -\frac{\Delta^2}{4}\sum_{\substack{k=-\infty\\k\neq -n}}^{\infty}\frac{J_k'^2}{(n+k)\omega} = -\frac{\Delta^2}{4}\sum_{\substack{k=-\infty\\k\neq 0}}^{\infty}\frac{J_{k-n}'^2}{k\omega} \\ &= -\frac{\Delta^2}{4}\sum_{k=1}^{\infty}\left[\frac{J_{k-n}'^2}{k\omega} - \frac{J_{-k-n}'^2}{k\omega}\right] \approx 0. \end{aligned} \tag{5.55}$$

This is somewhat surprising because the level shift presumably increases as the field amplitude increases like classical examples of the two-level system [28, 32, 221, 228]. For this superconducting qubit system, however, longitudinal terms driven by the strong ac field show different behavior of the level shift. The two harmonic series with the Bessel functions in Eq. (5.55) are diverged separately but canceled by each other because $J_{k-n}'^2 \approx J_{-k-n}'^2$ for all k. Therefore, the level shift asymptotically diminishes in the strong field regime. However, δ does not monotonously decrease because of the summation with the Bessel functions

in Eq. (5.44). Figure 5.3 shows the change of δ, numerically computed from Eq. (5.44), as a function of the field amplitude A for a few n-photon cases. Due to this level shift δ, the multiphoton resonance condition is not $\varepsilon_0 = n\omega$ as derived from RWA, but shifted to

$$\varepsilon_0 - 2\delta = n\omega \quad (n \geq 1). \tag{5.56}$$

To summarize, the level shift δ appears more vivid in the weak-field regime. Note that the shift δ is most prominent when the number of photons involved is small ($n \gtrsim 1$).

5.4 Multiphoton resonance process and quantum interference

Figure 5.4 shows the quasienergies and corresponding time-averaged transition probabilities as a function of ε_0 with fixed parameters of $\Delta/\omega = 0.5$ and $A/\omega = 5.0$, computed by solving Eq. (5.15). The solid red lines indicate lower Floquet states and dashed blue lines indicate upper Floquet states. Due to the periodicity of the quasienergy, the quasienergy plot has repeating structure by ω with the avoided crossings between the lower and upper Floquet states in the vicinity of $\varepsilon_0 \approx n\omega$ (n is a positive integer). At the avoided crossings, the lower and upper Floquet states are strongly mixed and resonance transitions between $|\alpha\rangle$ and $|\beta\rangle$ occur, as shown in the plot of time-averaged transition probability. Also $\varepsilon_0 \approx n\omega$ indicates that these transitions are multiphoton resonance processes.

To compare the numerical and analytic results, we present the transition probability plots as a function of ε_0 in Fig. 5.5, computed by a numerical solu-

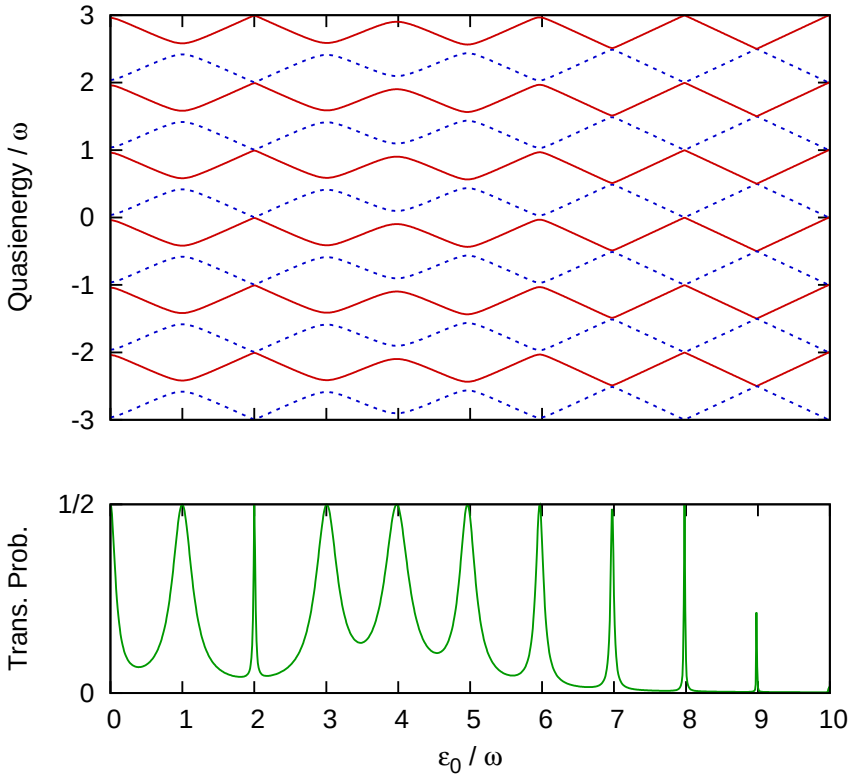

Figure 5.4: Plots of quasienergies and transition probabilities as a function of ε_0. $\Delta/\omega = 0.5$ and $A/\omega = 5.0$ are used.

tion of the full matrix of Eq. (5.15) and analytic solutions of the 2×2 matrices of Eqs. (5.30) and (5.42). Figure 5.5(a) shows the weak-field case of A/ω=0.5 and Fig. 5.5(b) the strong-field case of A/ω=10.0. Δ/ω=0.5 is used for both cases. The solid red line indicates the numerical solution by solving a 202×202 Floquet matrix. The dotted green line is used for the RWA solution, and the dashed blue line for the second-order GVV solution. The third-order GVV result is not shown because it is almost the same as the second-order one in this regime. The analytic GVV expression shows very good agreement with the numerical results near n-photon resonance regions, whereas the RWA results show large deviations in the weak-field case in Fig. 5.5(a). The time-averaged transition probability hits the maximum value of $\frac{1}{2}$ near $\varepsilon_0 \approx n\omega$. Note that in Fig. 5.5(a) those resonance positions of the numerical and GVV solutions are ac Stark shifted due to the level shift δ in the weak-field regime. As ε_0 increases, this shift becomes smaller according to the dominant terms in Eq. (5.52). Since the RWA method does not include the level shift, the dotted green line remains unshifted. On the other hand, in the strong-field case of Fig. 5.5(b), the level shift diminishes and all lines coincide near the multiphoton resonances.

To reveal the dependence of the ac Stark shift upon the field amplitude, Fig. 5.6 plots quasienergies as a function of A. ε_0/ω=4.9 and Δ/ω=0.5 are fixed. For clarity, Fig. 5.6 shows the behavior of the lower quasienergies only. The GVV results (dashed blue line) coincide with the numerical results (solid red line). In contrast, quasienergies computed by the RWA method (dotted green line) deviates from the numerical results in the weak A region and this deviation decreases as A increases. Oscillating patterns as a function of A are mainly due to $|u|$, i.e., the shape of the Bessel function. From Eqs. (5.45) and (5.46), q

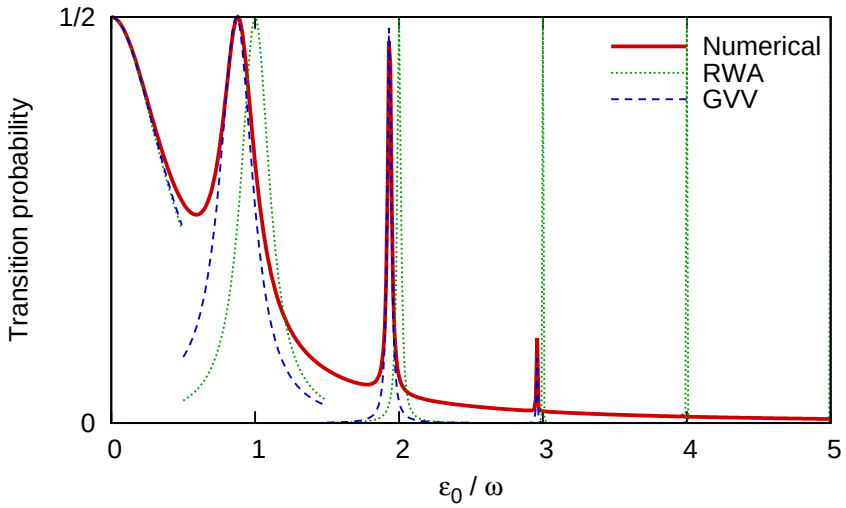

(a) Weak field: $A/\omega = 0.5$

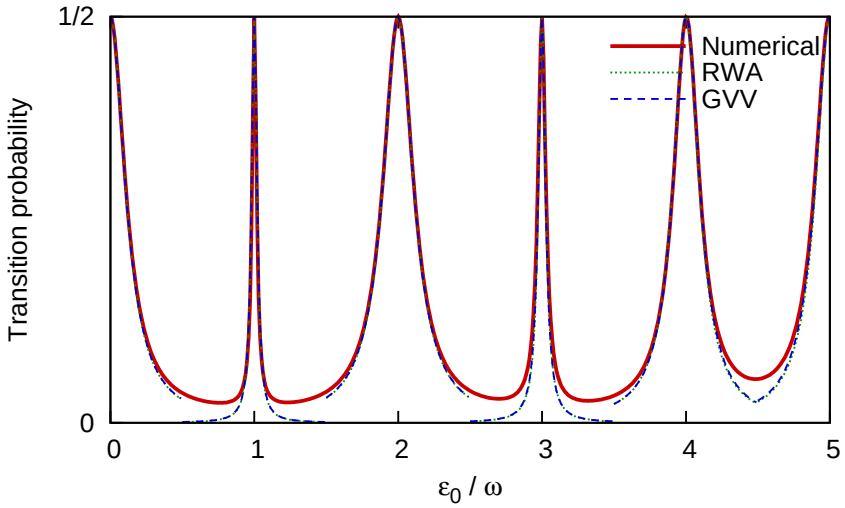

(b) Strong field: $A/\omega = 10.0$

Figure 5.5: Comparison for numerical results and analytic RWA and GVV results by the transition probability plots as a function of ε_0. $\Delta/\omega = 0.5$ is used.

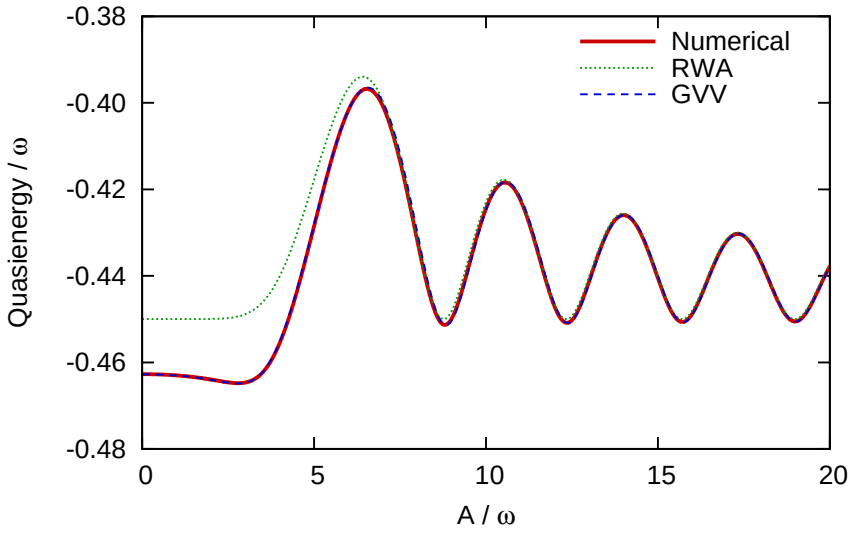

Figure 5.6: Comparison for numerical results and analytic RWA and GVV results by the quasienergy plots as a function of A. $\Delta/\omega = 0.5$ and $\varepsilon_0/\omega = 4.9$ are used.

mainly involves $|J_n(A/\omega)|$ when $\varepsilon_0 - 2\delta \approx n\omega$. For example, in Fig. 5.6, the oscillating patterns follow $|J_5(A/\omega)|$ because $\varepsilon_0/\omega \approx 5$.

In the transition probability plot of Fig. 5.4, one can see that the width of the peaks varies non-monotonically as ε_0 (i.e., n) increases. In fact, these patterns also depend on A. These widths are correlated with the difference between the lower and upper states at the avoided crossings in the quasienergy plot. Figures 5.7(a)–(c) show contour maps of the transition probability computed by Eq. (5.16) as a function of A and ε_0 with Δ/ω=0.1, 0.5, and 1.0, respectively. Multiphoton resonance processes occur near integer numbers closest to ε_0/ω indicated as bright yellow fringes in the plot. Figure 5.7(a) with relatively small Δ agrees well with previous experimental and theoretical results for the superconducting flux qubit [226]. In Figs. 5.7(b) and (c) with large Δ, however, it is clearly shown that the level shift alters multiphoton resonance positions especially in the regime of small ε_0 and weak A. Also for all figures resonance tran-

sitions are suppressed at certain positions of A, which is a phenomenon known as the coherent destruction of tunneling [240, 243]. These positions can be determined by the roots of the Bessel function of order of n that is the nearest integer to ε_0/ω [226, 233]. From the analytic expression of the time-averaged transition probability in Eq. (5.48), we can easily confirm that $\bar{P}^{(n)}_{\alpha\to\beta} \to 0$ as $u \to 0$. When $J_{-n}(A/\omega) = 0$, the first-order of Δ in u in Eq. (5.43) disappears and u is proportional to Δ^3. Thus, the width of the time-averaged transition probability becomes very narrow near the roots of the Bessel function, $J_{-n}(A/\omega)$, which depends on the number of photons $n(\approx \varepsilon_0/\omega)$ and the amplitude A.

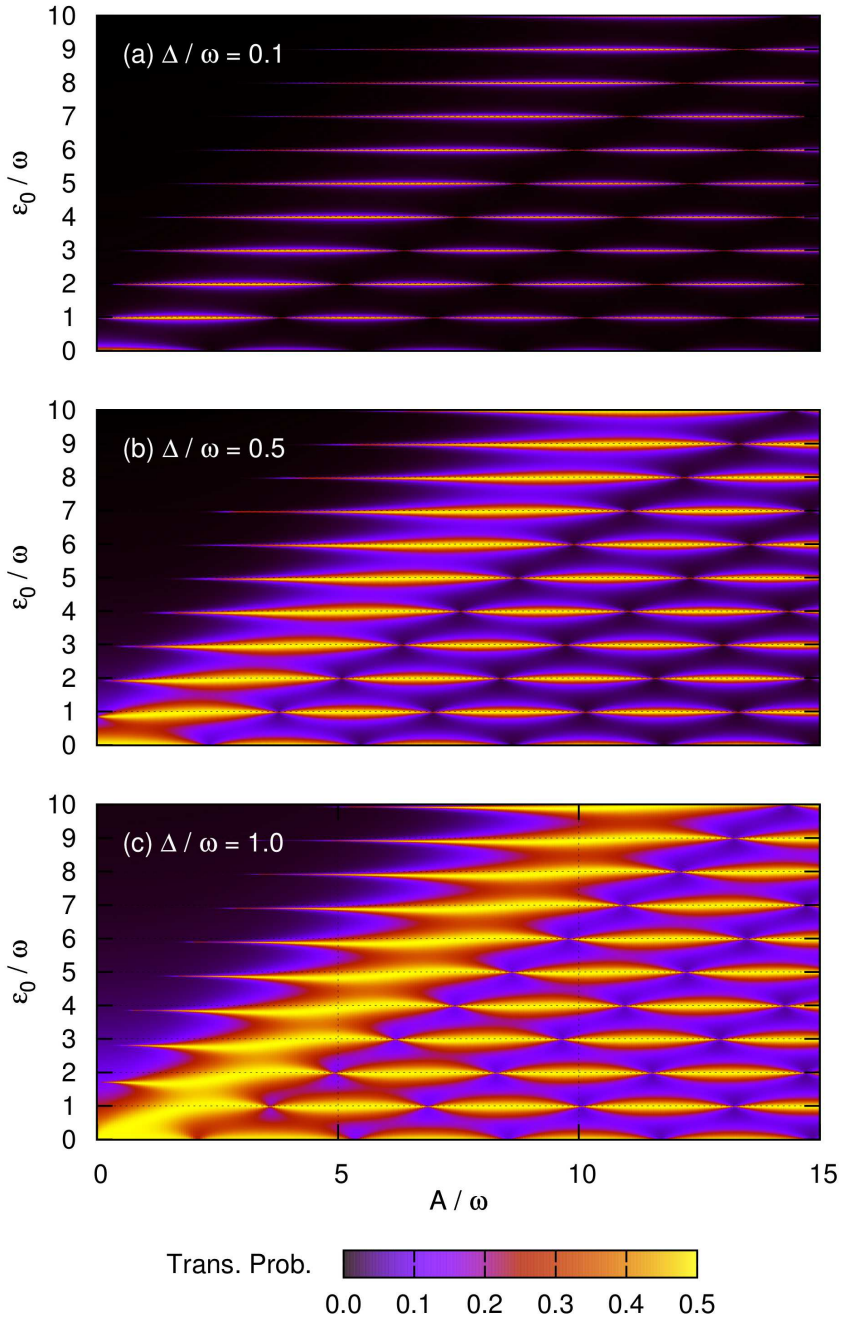

Figure 5.7: Multiphoton quantum interference fringe patterns of the transition probability in the superconducting qubit driven by intense ac fields as a function of A and ε_0 with different values of Δ. (a) $\Delta/\omega = 0.1$, (b) $\Delta/\omega = 0.5$, and (c) $\Delta/\omega = 1.0$.

Chapter 6

Conclusion

We introduce the Voronoi-cell finite difference (VFD) method for accurate electronic structure calculations for the first time. Based on the Voronoi diagram and natural neighboring relations, the method provides simple expressions for the discrete Laplacian and gradient operators on *unstructured* grids. As one of *unstructured* grid distributions, we introduce highly adaptive multicenter molecular grids combining spherical atomic grids centered at nuclear positions. With the VFD method augmented by multicenter molecular grids, the Schrödinger equation for one-electron systems is solved for accuracy assessment, showing systematic improvement by increasing the number of grids. Then VFD is applied to the density-functional calculations for many-electron polyatomic molecules within good precision in comparison with other calculations. Also we propose the high-order VFD scheme that involves further natural neighboring grid points to improve accuracy and efficiency even better.

Next we develop the new time-dependent Voronoi-cell finite difference (TD-VFD) method to investigate strong-field phenomena of polyatomic molecules in intense ultrashort laser fields, combined with the efficient and accurate time-propagation method of the split-operator technique in the energy representa-

tion. The method is applied to solve the self-interaction-free time-dependent density-functional theory equations for strong-field electronic dynamics including all spin-orbitals and continuum states. We present detailed studies of multiphoton ionization (MPI) of N_2, H_2O, and CO_2 in intense ultrashort laser fields with arbitrary orientation, including electron correlation and multielectron responses. Our results show that the orientation dependence of MPI is determined by the symmetries and dynamics of multiple orbitals. For N_2, the orientation dependent pattern of MPI is reflected by contributions from HOMO and HOMO-1. For H_2O, the contribution from HOMO-1 dominates the overall orientation dependent pattern of MPI when the laser field polarization is varied in a specific direction. For CO_2, the maximum peak of MPI is predicted to be at 40° in good agreement with recent experiments, whereas other theoretical models fail to predict the same pattern. The photoelectron angular distribution of CO_2 reveals the delicate relation between the orientation dependence and the molecular orbital symmetry. These features emphasize the importance of multiple orbital contributions to the MPI processes, and enable us to selectively probe individual orbitals in strong-field electronic dynamics. Also we perform high-order harmonic generation (HHG) calculations of CO_2 with arbitrary orientation. Our results show that HHG of CO_2 has the particular orientation dependence influenced by the orientation dependence in the ionization process and the two-center interference in the recombination process.

For the frequency-comb laser, we show that a train of an infinite number of short laser pulses generates spectral combs in the frequency domain, which can be exactly expressed in terms of the main frequency and the repetition frequency. The many-mode Floquet theory utilizing those two frequencies is extended to accurately solve the interaction between the quantum system and

frequency-comb laser. We found that there are simultaneous multiphoton resonance processes between the system and comb laser, and that they can be optimally controlled by tuning the pulse-to-pulse CEP shift. HHG driven by intense frequency-comb laser fields has the comb structure with the same repetition frequency and a different offset for each harmonic. Moreover, HHG can be dramatically enhanced by tuning the CEP shift due to simultaneous multiphoton resonance processes among all the comb frequencies.

Next, we extend the generalized Floquet theory to investigate the superconducting flux qubit driven by a strong ac field. The numerical and analytic solutions of the generalized Floquet formalism are applied to explain multiphoton resonance processes between the qubit and the driving ac field. We compare two analytic solutions: the rotating wave approximation (RWA) and the generalized Van Vleck (GVV) nearly degenerate perturbation theory. It is shown that the GVV approach accurately includes the ac Stark level shift which is completely absent within RWA. The level shifts in resonance positions are significant when the tunnel splitting is large, the field is weak, and a small number of photons are involved. The quasienergy and the time-averaged transition probability from Floquet calculations are plotted showing multiphoton resonance transitions at the avoided crossings. From the transition probability plot as a function of the field amplitude and the detuning energy, we observe the Bessel function-like fringe patterns including the level shift. The general method described here provides a unified theoretical treatment covering a wide range of parameter space. Applications of the Floquet theory to various superconducting qubits lead us to a better understanding of the results of spectroscopy measurement and the dynamics of ac driven qubits which are important to more accurate characterization of and performance improvement of the qubits.

The theoretical and computational methods proposed in this dissertation provide generalized tools to investigate strong-field multiphoton processes. For future works, they can be extended to explore new frontiers of attosecond science, such as molecular attosecond x-ray spectroscopy, attosecond probing and controlling of electron motions in atoms, molecules, and chemical reactions. Also the proposed VFD method on multicenter molecular grids can be employed for advanced quantum chemistry calculations, for examples, basis-set-free Hartree–Fock (HF) and post-HF methods, and grid-based linear-scaling DFT calculations. Since the Voronoi diagram is intrinsically expressed in the multi-dimensional space, it may be possible to extend VFD for a fully *ab initio* method in $3N$-dimensional for N particles, combined with improved high-order scheme. Finally, two approaches explored in this dissertation, VFD and Floquet methods, which have been separately applied for spatial and temporal treatments, can be unified for high-precision atomic and molecular physics.

References

[1] B. Sheehy and L. F. DiMauro, Atomic and molecular dynamics in intense optical fields, *Annu. Rev. Phys. Chem.* **47**, 463–494 (1996).

[2] T. Brabec and F. Krausz, Intense few-cycle laser fields: Frontiers of nonlinear optics, *Rev. Mod. Phys.* **72**, 545–591 (2000).

[3] J. Ye and S. T. Cundiff, *Femtosecond Optical Frequency Comb: Principle, Operation, and Applications* (Springer, New York, 2005).

[4] M. A. Nielsen and I. L. Chuang, *Quantum Computation and Quantum Information* (Cambridge University Press, Cambridge, 2000), 1st ed.

[5] A. Scrinzi, M. Y. Ivanov, R. Kienberger, and D. M. Villeneuve, Attosecond physics, *J. Phys. B: At. Mol. Opt. Phys.* **39**, R1–R37 (2006).

[6] P. B. Corkum and F. Krausz, Attosecond science, *Nature Phys.* **3**, 381–387 (2007).

[7] F. Krausz and M. Ivanov, Attosecond physics, *Rev. Mod. Phys.* **81**, 163–234 (2009).

[8] P. H. Bucksbaum, The future of attosecond spectroscopy, *Science* **317**, 766–769 (2007).

[9] P. Agostini and L. F. DiMauro, The physics of attosecond light pulses, *Rep. Prog. Phys.* **67**, 813–855 (2004).

[10] M. Hentschel, R. Kienberger, C. Spielmann, G. A. Reider, N. Milosevic, T. Brabec, P. Corkum, U. Heinzmann, M. Drescher, and F. Krausz, Attosecond metrology, *Nature* **414**, 509–513 (2001).

[11] M. Drescher, M. Hentschel, R. Kienberger, G. Tempea, C. Spielmann, G. A. Reider, P. B. Corkum, and F. Krausz, X-ray pulses approaching the attosecond frontier, *Science* **291**, 1923–1927 (2001).

[12] P. M. Paul, E. S. Toma, P. Breger, G. Mullot, F. Augé, P. Balcou, H. G. Muller, and P. Agostini, Observation of a train of attosecond pulses from high harmonic generation, *Science* **292**, 1689–1692 (2001).

[13] M. Drescher, M. Hentschel, R. Kienberger, M. Uiberacker, V. Yakovlev, A. Scrinzi, T. Westerwalbesloh, U. Kleineberg, U. Heinzmann, and F. Krausz, Time-resolved atomic inner-shell spectroscopy., *Nature* **419**, 803–807 (2002).

[14] R. Kienberger, M. Hentschel, M. Uiberacker, C. Spielmann, M. Kitzler, A. Scrinzi, M. Wieland, T. Westerwalbesloh, U. Kleineberg, U. Heinzmann, et al., Steering attosecond electron wave packets with light, *Science* **297**, 1144–1148 (2002).

[15] A. Baltuška, T. Udem, M. Uiberacker, M. Hentschel, E. Goulielmakis, C. Gohle, R. Holzwarth, V. S. Yakovlev, A. Scrinzi, T. W. Hänsch, et al., Attosecond control of electronic processes by intense light fields, *Nature* **421**, 611–615 (2003).

[16] M. F. Kling, C. Siedschlag, A. J. Verhoef, J. I. Khan, M. Schultze, T. Uphues, Y. Ni, M. Uiberacker, M. Drescher, F. Krausz, et al., Control of electron localization in molecular dissociation, *Science* **312**, 246–248 (2006).

[17] H. Niikura, F. Légaré, R. Hasbani, M. Y. Ivanov, D. M. Villeneuve, and P. B. Corkum, Probing molecular dynamics with attosecond resolution using correlated wave packet pairs, *Nature* **421**, 826–829 (2003).

[18] S. Baker, J. S. Robinson, C. A. Haworth, H. Teng, R. A. Smith, C. C. Chirilă, M. Lein, J. W. G. Tisch, and J. P. Marangos, Probing proton dynamics in molecules on an attosecond time scale, *Science* **312**, 424–427 (2006).

[19] R. Kienberger, E. Goulielmakis, M. Uiberacker, A. Baltuska, V. Yakovlev, F. Bammer, A. Scrinzi, T. Westerwalbesloh, U. Kleineberg, U. Heinzmann, et al., Atomic transient recorder, *Nature* **427**, 817–821 (2004).

[20] M. Uiberacker, T. Uphues, M. Schultze, A. J. Verhoef, V. Yakovlev, M. F. Kling, J. Rauschenberger, N. M. Kabachnik, H. Schröder, M. Lezius, et al., Attosecond real-time observation of electron tunnelling in atoms, *Nature* **446**, 627–632 (2007).

[21] P. Baum and A. H. Zewail, Attosecond electron pulses for 4D diffraction and microscopy, *Proc. Natl. Acad. Sci. U. S. A.* **104**, 18409–18414 (2007).

[22] M. Meckel, D. Comtois, D. Zeidler, A. Staudte, D. Pavičić, H. C. Bandulet, H. Pépin, J. C. Kieffer, R. Dörner, D. M. Villeneuve, et al., Laser-induced electron tunneling and diffraction, *Science* **320**, 1478–1482 (2008).

[23] E. Goulielmakis, V. S. Yakovlev, A. L. Cavalieri, M. Uiberacker, V. Pervak, A. Apolonski, R. Kienberger, U. Kleineberg, and F. Krausz, Attosecond control and measurement: lightwave electronics, *Science* **317**, 769–775 (2007).

[24] F. Remacle and R. D. Levine, An electronic time scale in chemistry, *Proc. Natl. Acad. Sci. U. S. A.* **103**, 6793–6798 (2006).

[25] J. Itatani, J. Levesque, D. Zeidler, H. Niikura, H. Pepin, J. C. Kieffer, P. B. Corkum, and D. M. Villeneuve, Tomographic imaging of molecular orbitals, *Nature* **432**, 867–871 (2004).

[26] M. Lein, Molecular imaging using recolliding electrons, *J. Phys. B: At. Mol. Opt. Phys.* **40**, R135–R173 (2007).

[27] H. Kapteyn, O. Cohen, I. Christov, and M. Murnane, Harnessing attosecond science in the quest for coherent x-rays, *Science* **317**, 775–778 (2007).

[28] S. I. Chu and D. A. Telnov, Beyond the Floquet theorem: generalized Floquet formalisms and quasienergy methods for atomic and molecular multiphoton processes in intense laser, *Phys. Rep.* **390**, 1–131 (2004).

[29] J. H. Posthumus, The dynamics of small molecules in intense laser fields, *Rep. Prog. Phys.* **67**, 623–665 (2004).

[30] R. Kurzweil, *The Singularity Is Near: When Humans Transcend Biology* (Viking, New York, 2005).

[31] S. I. Chu, J. V. Tietz, and K. K. Datta, Quantum dynamics of molecular multiphoton excitation in intense laser and static electric fields: Floquet theory, quasienergy spectra, and application to the HF molecule, *J. Chem. Phys.* **77**, 2968–2978 (1982).

[32] S. I. Chu and W. P. Reinhardt, Intense field multiphoton ionization via complex dressed states: Application to the H atom, *Phys. Rev. Lett.* **39**, 1195–1198 (1977).

[33] S. I. Chu, Floquet theory and complex quasi-vibrational energy formalism for intense field molecular photodissociation, *J. Chem. Phys.* **75**, 2215–2221 (1981).

[34] P. Agostini, F. Fabre, G. Mainfray, G. Petite, and N. K. Rahman, Free-free transitions following six-photon ionization of xenon atoms, *Phys. Rev. Lett.* **42**, 1127–1130 (1979).

[35] S. I. Chu and J. Cooper, Threshold shift and above-threshold multiphoton ionization of atomic hydrogen in intense laser fields, *Phys. Rev. A* **32**, 2769–2775 (1985).

[36] S. I. Chu, Complex quasivibrational energy formalism for intense-field multiphoton and above-threshold dissociation: Complex-scaling Fourier-grid Hamiltonian method, *J. Chem. Phys.* **94**, 7901–7909 (1991).

[37] D. A. Telnov and S. I. Chu, Theoretical study of the energy spectra of multiphoton above-threshold dissociation of H_2^+ in intense laser fields, *Chem. Phys. Lett.* **255**, 223–231 (1996).

[38] A. McPherson, G. Gibson, H. Jara, U. Johann, T. S. Luk, I. A. McIntyre, K. Boyer, and C. K. Rhodes, Studies of multiphoton production of vacuum-ultraviolet radiation in the rare gases, *J. Opt. Soc. Am. B* **4**, 595–601 (1987).

[39] M. Ferray, A. L'Huillier, X. F. Li, L. A. Lompré, G. Mainfray, and C. Manus, Multiple-harmonic conversion of 1064 nm radiation in rare gases, *J. Phys. B: At. Mol. Opt. Phys.* **21**, L31–L35 (1988).

[40] T. F. Jiang and S. I. Chu, High-order harmonic generation in atomic hydrogen at 248 nm: Dipole-moment versus acceleration spectrum, *Phys. Rev. A* **46**, 7322–7324 (1992).

[41] X. M. Tong and S. I. Chu, Theoretical study of multiple high-order harmonic generation by intense ultrashort pulsed laser fields: A new generalized pseudospectral time-dependent method, *Chem. Phys.* **217**, 119–130 (1997).

[42] T. Seideman, M. Y. Ivanov, and P. B. Corkum, Role of electron localization in intense-field molecular ionization, *Phys. Rev. Lett.* **75**, 2819–2822 (1995).

[43] Z. Y. Zhou and S. I. Chu, Exploration of Coulomb explosion dynamics through excited vibrational states of molecules, *Phys. Rev. A* **71**, 011402(R) (2005).

[44] G. H. Yao and S. I. Chu, Laser-induced molecular stabilization and trapping and chemical bond hardening in intense laser fields, *Chem. Phys. Lett.* **197**, 413–418 (1992).

[45] D. A. Telnov, J. Y. Wang, and S. I. Chu, Two-color phase-control of high-order harmonic-generation in intense laser fields, *Phys. Rev. A* **52**, 3988–3996 (1995).

[46] X. Chu and S. I. Chu, Optimization of high-order harmonic generation by genetic algorithm and wavelet time-frequency analysis of quantum dipole emission, *Phys. Rev. A* **64**, 021403(R) (2001).

[47] K. C. Kulander, K. J. Schafer, and J. L. Krause, in *Atoms in Intense Laser Fields*, edited by M. Gavrila (Academic Press, Boston, 1992), vol. 1 of *Adv. At. Mol. Opt. Phys. Suppl.*, pp. 247–300.

[48] X. Chu, Atomic and molecular multiphoton processes in intense laser fields, Ph.D. thesis, University of Kansas, Lawrence, Kansas (2001).

[49] S. I. Chu, Recent development of self-interaction-free time-dependent density-functional theory for nonperturbative treatment of atomic and molecular multiphoton processes in intense laser fields, *J. Chem. Phys.* **123**, 062207 (2005).

[50] X. Chu and S. I. Chu, Self-interaction-free time-dependent density-functional theory for molecular processes in strong fields: High-order harmonic generation of H_2 in intense laser fields, *Phys. Rev. A* **63**, 023411 (2001).

[51] S.-K. Son, A new 3D grid method for accurate electronic structure calculation of polyatomic molecules: The Voronoi-cell finite difference method (2009), submitted.

[52] S.-K. Son and S. I. Chu, Theoretical study of orientation-dependent multiphoton ionization of polyatomic molecules in intense ultrashort laser fields: A new time-dependent Voronoi-cell finite difference method, *Chem. Phys.* **366**, 91–102 (2009).

[53] S.-K. Son and S. I. Chu, Multielectron effects on the orientation dependence and photoelectron angular distribution of multiphoton ionization of CO_2 in strong laser fields, *Phys. Rev. A* **80**, 011403(R) (2009).

[54] S.-K. Son and S. I. Chu, Many-mode Floquet theoretical approach for coherent control of multiphoton dynamics driven by intense frequency-comb laser fields, *Phys. Rev. A* **77**, 063406 (2008).

[55] J. J. Carrera, S.-K. Son, and S. I. Chu, *Ab initio* theoretical investigation of the frequency comb structure and coherence in the vuv-xuv regimes via high-order harmonic generation, *Phys. Rev. A* **77**, 031401(R) (2008).

[56] S.-K. Son, S. Han, and S. I. Chu, Floquet formulation for the investigation of multiphoton quantum interference in a superconducting qubit driven by a strong ac field, *Phys. Rev. A* **79**, 032301 (2009).

[57] A. Szabo and N. S. Ostlund, *Modern Quantum Chemistry* (McGraw-Hill, New York, 1989).

[58] S. F. Boys and F. Bernardi, The calculation of small molecular interactions by the differences of separate total energies. Some procedures with reduced errors, *Mol. Phys.* **19**, 553–566 (1970).

[59] P.-O. Löwdin, On the non-orthogonality problem, *Adv. Quantum Chem.* **5**, 185–199 (1970).

[60] M. Uhlmann, T. Kunert, and R. Schmidt, Error of finite basis expansions in time-dependent calculations of atom-laser interaction, *Phys. Rev. E* **72**, 036704 (2005).

[61] T. L. Beck, Real-space mesh techniques in density-funcitonal theory, *Rev. Mod. Phys.* **72**, 1041–1080 (2000).

[62] T. Kato, On the eigenfunctions of many-particle systems in quantum mechanics, *Commun. Pure Appl. Math.* **10**, 151–177 (1957).

[63] J. Zhang and T. Nakajima, Coulomb effects in photoionization of H atoms irradiated by intense laser fields, *Phys. Rev. A* **75**, 043403 (2007).

[64] A. Gordon, R. Santra, and F. X. Kärtner, Role of the Coulomb singularity in high-order harmonic generation, *Phys. Rev. A* **72**, 063411 (2005).

[65] M. F. Ciappina, C. C. Chirilă, and M. Lein, Influence of coulomb continuum wave functions in the description of high-order harmonic generation with H_2^+, *Phys. Rev. A* **75**, 043405 (2007).

[66] X. Chu and S. I. Chu, Time-dependent density-functional theory for molecular processes in strong fields: Study of multiphoton processes and dynamical response of individual valence electrons of N_2 in intense laser fields, *Phys. Rev. A* **64**, 063404 (2001).

[67] D. A. Telnov and S. I. Chu, *Ab initio* study of the orientation effects in multiphoton ionization and high-order harmonic generation from the ground and excited electronic states of H_2^+, *Phys. Rev. A* **76**, 043412 (2007).

[68] J. F. Thompson, B. K. Soni, and N. P. Weatherill, *Handbook of Grid Generation* (CRC Press, 1999).

[69] A. D. Becke, Basis-set-free density-functional quantum-chemistry, *Int. J. Quant. Chem. Quant. Chem. Symp.* **23**, 599–609 (1989).

[70] R. M. Dickson and A. D. Becke, Basis-set-free local density-functional calculations of geometries of polyatomic molecules, *J. Chem. Phys.* **99**, 3898–3905 (1993).

[71] A. D. Becke, A multicenter numerical integration scheme for polyatomic molecules, *J. Chem. Phys.* **88**, 2547–2553 (1988).

[72] J. M. Pérez-Jordá, A. D. Becke, and E. San-Fabián, Automatic numerical integration techniques for polyatomic molecules, *J. Chem. Phys.* **100**, 6520–6534 (1994).

[73] A. D. Becke and R. M. Dickson, Numerical solution of Schrödinger's equation in polyatomic molecules, *J. Chem. Phys.* **92**, 3610–3612 (1990).

[74] G. Voronoï, Nouvelles applications des paramètres continus à la théorie des formes quadratiques, *J. Reine Angew. Math.* **133**, 97–178 (1907).

[75] G. Voronoï, Nouvelles applications des paramètres continus à la théorie des formes quadratiques. deuxième mémoire: Recherches sur les parallélloèdres primitifs, *J. Reine Angew. Math.* **134**, 198–287 (1908).

[76] G. Voronoï, Nouvelles applications des paramètres continus à la théorie des formes quadratiques. deuxième mémoire: Recherches sur les parallélloèdres primitifs. second partie. domaines de formes quadratiques correspondant aux différent types de paralléloèdres primitifs, *J. Reine Angew. Math.* **136**, 67–181 (1909).

[77] F. Aurenhammer, Voronoi diagrams – a survey of a fundamental geometric data structure, *ACM Comput. Surv.* **23**, 345–405 (1991).

[78] A. Okabe, B. Boots, K. Sugihara, and S. N. Chiu, *Spatial Tessellations: Concepts and Applications of Voronoi Diagrams* (John Wiley & Sons, Chichester, 2000), 2nd ed.

[79] J. Braun and M. Sambridge, A numerical method for solving partial differential equations on highly irregular evolving grids, *Nature* **376**, 655–660 (1995).

[80] N. Sukumar, B. Moran, A. Y. Semenov, and V. V. Belikov, Natural neighbour Galerkin methods, *Int. J. Numer. Meth. Engng* **50**, 1–27 (2001).

[81] E. Cueto, N. Sukumar, B. Calvo, M. A. Martínez, J. Cegoñino, and M. Doblaré, Overview and recent advances in natural neighbour Galerkin methods, *Arch. Comput. Meth. Engng.* **10**, 307–384 (2003).

[82] N. Sukumar, Voronoi cell finite difference method for the diffusion operator on arbitrary unstructured grids, *Int. J. Numer. Meth. Engng* **57**, 1–34 (2003).

[83] N. Sukumar and J. E. Bolander, Numerical computation of discrete differential operators on non-uniform grids, *CMES Comput. Model. Eng. Sci.* **4**, 691–705 (2003).

[84] N. Sukumar and R. W. Wright, Overview and construction of meshfree basis functions: From moving least squares to entropy approximants, *Int. J. Numer. Meth. Engng* **70**, 181–205 (2007).

[85] M. Griebel and M. A. Schweitzer, eds., *Meshfree Methods for Partial Differential Equations*, vol. 26 of *Lecture notes in computational science and engineering* (Springer, Berlin, 2003).

[86] G. de Fabritiis, S. Succi, and P. V. Coveney, Electronic structure calculations using self-adaptive multiscale Voronoi basis functions, *J. Stat. Phys.* **107**, 159–171 (2002).

[87] J. Ackermann, B. Erdmann, and R. Roitzsch, A self-adaptive multilevel finite element method for the stationary Schrödinger equation in three space dimensions, *J. Chem. Phys.* **101**, 7643–7650 (1994).

[88] J. E. Pask, B. M. Klein, C. Y. Fong, and P. A. Sterne, Real-space local polynomial basis for solid-state electronic-structure calculations: A finite-element approach, *Phys. Rev. B* **59**, 12532–12358 (1999).

[89] S. Tonzani and C. H. Greene, Low-energy electron scattering from DNA and RNA bases: Shape resonances and radiation damage, *J. Chem. Phys.* **124**, 054312 (2006).

[90] P. F. Batcho, Computational method for general multicenter electronic structure calculations, *Phys. Rev. E* **61**, 7169–7183 (2000).

[91] F. Gygi, Electronic-structure calculations in adaptive coordinates, *Phys. Rev. B* **48**, 11692–11700 (1993).

[92] N. A. Modine, G. Zumbach, and E. Kaxiras, Adaptive-coordinate real-space electronic-structure calculations for atoms, molecules, and solids, *Phys. Rev. B* **55**, 10289–10301 (1997).

[93] M. Heiskanen, T. Torsti, M. J. Puska, and R. M. Nieminen, Multigrid method for electronic structure calculations, *Phys. Rev. B* **63**, 245106 (2001).

[94] T. Torsti, M. Heiskanen, M. J. Puska, and R. M. Nieminen, MIKA: Multigrid-based program package for electronic structure calculations, *Int. J. Quant. Chem.* **91**, 171–176 (2003).

[95] J. Wang and T. L. Beck, Efficient real-space solution of the Kohn–Sham equations with multiscale techniques, *J. Chem. Phys.* **112**, 9223–9228 (2000).

[96] T. A. Arias, Multiresolution analysis of electronic structure: semicardinal and wavelet bases, *Rev. Mod. Phys.* **71**, 267–311 (1999).

[97] R. J. Harrison, G. I. Fann, T. Yanai, Z. Gan, and G. Beylkin, Multiresolution quantum chemistry: Basic theory and initial applications, *J. Chem. Phys.* **121**, 11587–11598 (2004).

[98] T. Yanai, G. I. Fann, Z. Gan, R. J. Harrison, and G. Beylkin, Multiresolution quantum chemistry in multiwavelet bases: Hartree–Fock exchange, *J. Chem. Phys.* **121**, 6680–6688 (2004).

[99] D. Toffoli, M. Stener, G. Fronzoni, and P. Decleva, Convergence of the multicenter B-spline DFT approach for the continuum, *Chem. Phys.* **276**, 25–43 (2002).

[100] T. N. Rescigno, D. A. Horner, F. L. Yip, and C. W. McCurdy, Hybrid approach to molecular continuum processes combining Gaussian basis functions and the discrete variable representation, *Phys. Rev. A* **72**, 052709 (2005).

[101] J. R. Chelikowsky, N. Troullier, and Y. Saad, Finite-difference-pseudopotential method: Electronic structure calculations without a basis, *Phys. Rev. Lett.* **72**, 1240–1243 (1994).

[102] J. R. Chelikowsky, N. Troullier, K. Wu, and Y. Saad, Higher-order finite-difference pseudopotential method: An application to diatomic molecules, *Phys. Rev. B* **50**, 11355–11364 (1994).

[103] R. Sibson, A vector identity for the Dirichlet tessellation, *Math. Proc. Cambridge Philos. Soc.* **87**, 151–155 (1980).

[104] C. B. Barber, D. P. Dobkin, and H. Huhdanpaa, The quickhull algorithm for convex hulls, *ACM Trans. Math. Software* **22**, 469–483 (1996), URL http://www.qhull.org/.

[105] G. B. Arfken and H. J. Weber, *Mathematical Methods for Physicists* (Harcourt/Academic Press, San Diego, 2001), 5th ed.

[106] P. S. Jensen, Finite difference techniques for variable grids, *Comput. & Structures* **2**, 17–29 (1972).

[107] T. Liszka and J. Orkisz, The finite difference method at arbitrary irregular grids and its application in applied mechanics, *Comput. & Structures* **11**, 83–95 (1980).

[108] M. Vinokur, An analysis of finite-difference and finite-volume formulations of conservation laws, *J. Comput. Phys.* **81**, 1–52 (1989).

[109] J. M. Hyman, R. J. Knapp, and J. C. Scovel, High order finite volume approximations of differential operators on nonuniform grids, *Physica D* **60**, 112–138 (1992).

[110] R. J. LeVeque, *Finite volume methods for hyperbolic problems* (Cambridge University Press, New York, 2002).

[111] R. B. Lehoucq, D. C. Sorensen, and C. Yang, *ARPACK Users' Guide: Solution of Large-Scale Eigenvalue Problems with Implicitly Restarted Arnoldi Methods* (SIAM, Philadelphia, 1998), URL http://www.caam.rice.edu/software/ARPACK/.

[112] O. Schenk and K. Gärtner, On fast factorization pivoting methods for symmetric indefinite systems, *Elec. Trans. Numer. Anal.* **23**, 158–179 (2006), URL http://www.pardiso-project.org/.

[113] D. González, E. Cueto, M. A. Martínez, and M. Doblaré, Numerical integration in natural neighbour Galerkin methods, *Int. J. Numer. Meth. Engng* **60**, 2077–2104 (2004).

[114] J. Lu, J. Qian, and W. Han, Discrete gradient method in solid mechanics, *Int. J. Numer. Meth. Engng* **74**, 619–641 (2008).

[115] C. Canuto, M. Y. Hussaini, A. Quarteroni, and T. A. Zang, *Spectral Methods in Fluid Dynamics* (Springer-Verlag, New York, 1988).

[116] V. I. Lebedev, Values of the nodes and weights of ninth to seventeenth order Gauss-Markov quadrature formulae invariant under the octahedron group with inversion, *Comput. Math. Math. Phys.* **15**, 44–51 (1975).

[117] V. I. Lebedev, Quadratures on a sphere, *Comput. Math. Math. Phys.* **16**, 10–24 (1976).

[118] V. I. Lebedev and D. N. Laikov, A quadrature formula for the sphere of the 131st algebraic order of accuracy, *Dokl. Math.* **59**, 477–481 (1999).

[119] R. S. Womersley and I. H. Sloan, How good can polynomial interpolation on the sphere be?, *Adv. Comput. Math.* **14**, 195–226 (2001).

[120] I. H. Sloan and R. S. Womersley, Extremal systems of points and numerical integration on the sphere, *Adv. Comput. Math.* **21**, 102–125 (2004).

[121] R. G. Parr and W. Yang, *Density-Functional Theory of Atoms and Molecules*, vol. 16 of *International series of monographs on chemistry* (Oxford University Press, New York, 1989).

[122] P. Hohenberg and W. Kohn, Inhomogeneous electron gas, *Phys. Rev.* **136**, B864–B871 (1964).

[123] W. Kohn and L. J. Sham, Self-consistent equations including exchange and correlation effects, *Phys. Rev.* **140**, A1133–A1138 (1965).

[124] J. C. Slater, A simplification of the Hartree–Fock method, *Phys. Rev.* **81**, 385–390 (1951).

[125] S. H. Vosko, L. Wilk, and M. Nusair, Accurate spin-dependent electron liquid correlation energies for local spin density calculations: a critical analysis, *Can. J. Phys.* **58**, 1200–1211 (1980).

[126] B. G. Johnson, P. M. W. Gill, and J. A. Pople, The performance of a family of density functional methods, *J. Chem. Phys.* **98**, 5612–5626 (1993).

[127] R. van Leeuwen and E. J. Baerends, Exchange-correlation potential with correct asymptotic behavior, *Phys. Rev. A* **49**, 2421–2431 (1994).

[128] P. R. T. Schipper, O. V. Gritsenko, S. J. A. van Gisbergen, and E. J. Baerends, Molecular calculations of excitation energies and (hyper)polarizabilities with a statistical average of orbital model exchange-correlation potentials, *J. Chem. Phys.* **112**, 1344–1352 (2000).

[129] J. P. Perdew and Y. Wang, Accurate and simple analytic representation of the electron-gas correlation energy, *Phys. Rev. B* **45**, 13244–13249 (1992).

[130] S. Liu and R. G. Parr, Consequences for exchange energy density functional of exponentially decaying nature of atomic electron densities, *J. Comput. Chem.* **20**, 2–11 (1999).

[131] M. M. Madsen and J. M. Peek, Eigenparameters for the lowest twenty electronic states of the hydrogen molecule ion, *At. Data* **2**, 171–204 (1971).

[132] M. W. Schmidt, K. K. Baldridge, J. A. Boatz, S. T. Elbert, M. S. Gordon, J. H. Jensen, S. Koseki, N. Matsunaga, K. A. Nguyen, S. Su, et al., General atomic and molecular electronic structure system, *J. Comput. Chem.* **14**, 1347–1363 (1993), URL http://www.msg.chem.iastate.edu/gamess/.

[133] K. A. Peterson, D. E. Woon, and J. Thom H. Dunning, Benchmark calculations with correlated molecular wave functions. IV. The classical barrier height of the H+H_2 $\rightarrow$ H_2+H reaction, *J. Chem. Phys.* **100**, 7410–7415 (1994).

[134] D. Feller, The role of databases in support of computational chemistry calculations, *J. Comput. Chem.* **17**, 1571–1586 (1996), URL https://bse.pnl.gov/bse/portal.

[135] J. C. L. Vieyra and A. V. Turbiner, H_3^{2+} molecular ion in a strong magnetic field: Triangular configuration, *Phys. Rev. A* **66**, 023409 (2002).

[136] T. H. Dunning, Jr., Gaussian basis sets for use in correlated molecular calculations. I. The atoms boron through neon and hydrogen, *J. Chem. Phys.* **90**, 1007–1023 (1989).

[137] D. A. Telnov, private communication.

[138] K. P. Huber and G. Herzberg, *Molecular Spectra and Molecular Structure*, IV. Constants of Diatomic Molecules (Van Nostrand, New York, 1979).

[139] G. Herzberg, *Molecular Spectra and Molecular Structure*, III. Electronic Spectra and Electronic Structure of Polyatomic Molecules (Van Nostrand, New York, 1966).

[140] A. R. Hoy and P. R. Bunker, A precise solution of the rotation bending schrödinger equation for a triatomic molecule with application to the water molecule, *J. Mol. Spectrosc.* **74**, 1–8 (1979).

[141] E. Hirota, Anharmonic potential function and equilibrium structure of methane, *J. Mol. Spectrosc.* **77**, 213–221 (1979).

[142] A. Castro, H. Appel, M. Oliveira, C. A. Rozzi, X. Andrade, F. Lorenzen, M. A. L. Marques, E. K. U. Gross, and A. Rubio, `octopus`: a tool for the application of time-dependent density functional theory, *Phys. Status Solidi B* **243**, 2465–2488 (2006).

[143] R. Krishnan, J. S. Binkley, R. Seeger, and J. A. Pople, Self-consistent molecular orbital methods. XX. A basis set for correlated wave functions, *J. Chem. Phys.* **72**, 650–654 (1980).

[144] T. Koopmans, Über die zuordnung von wellenfunktionen und eigenwerten zu den einzelnen elektronen eines atoms, *Physica* **1**, 104–113 (1934).

[145] D. P. Chong, O. V. Gritsenko, and E. J. Baerends, Interpretation of the Kohn–Sham orbital energies as approximate vertical ionization potentials, *J. Chem. Phys.* **116**, 1760–1772 (2002).

[146] O. V. Gritsenko and E. J. Baerends, The analog of Koopmans' theorem in spin-density functional theory, *J. Chem. Phys.* **117**, 9154–9159 (2002).

[147] D. A. Telnov and S. I. Chu, Effects of electron structure and multielectron dynamical response on strong-field multiphoton ionization of diatomic molecules with arbitrary orientation: An all-electron time-dependent density-functional-theory approach, *Phys. Rev. A* **79**, 041401(R) (2009).

[148] K. Siegbahn, C. Nordling, G. Johansson, J. Hedman, P. F. Heden, K. Hamrin, U. Gelius, T. Bergmark, L. O. Werme, R. Manne, et al., *ESCA Applied to Free Molecules* (North-Holland Pub. Co., Amsterdam, 1969).

[149] G. Bieri, L. Åsbrink, and W. von Niessen, 30.4-nm He(II) photoelectron spectra of organic molecules: Part IV. Fluoro-compounds (C, H, F), *J. Electron Spectrosc. Relat. Phenom.* **23**, 281–322 (1981).

[150] D. W. Turner, C. Baker, A. D. Baker, and C. R. Brundle, *Molecular Photoelectron Spectroscopy* (Wiley-interscience, London, 1970).

[151] H.-J. Freund, H. Kossmann, and V. Schmidt, Photoionization of inner valence electrons of CO_2 in the gas phase: a synchrotron radiation study using photon energies between 40 and 100 eV, *Chem. Phys. Lett.* **123**, 463–470 (1986).

[152] C. G. Ning, B. Hajgató, Y. R. Huang, S. F. Zhang, K. Liu, Z. H. Luo, S. Knippenberg, J. K. Deng, and M. S. Deleuze, High resolution electron momentum spectroscopy of the valence orbitals of water, *Chem. Phys.* **343**, 19–30 (2008).

[153] G. Bieri, L. Åsbrink, and W. von Niessen, 30.4-nm He(II) photoelectron spectra of organic molecules: Part VII. Miscellaneous compounds, *J. Electron Spectrosc. Relat. Phenom.* **27**, 129–178 (1982).

[154] G. Bieri and L. Åsbrink, 30.4-nm He(II) photoelectron spectra of organic molecules: Part I. Hydrocarbons, *J. Electron Spectrosc. Relat. Phenom.* **20**, 149–167 (1980).

[155] P. Baltzer, L. Karlsson, B. Wannberg, G. Öhrwall, D. M. P. Holland, M. A. MacDonald, M. A. Hayes, and W. von Niessen, An experimental and theoretical study of the valence shell photoelectron spectrum of the benzene molecule, *Chem. Phys.* **224**, 95–119 (1997).

[156] D. T. Clark, D. Kilcast, D. B. Adams, and W. K. R. Musgrave, An ESCA study of the molecular core binding energies of the fluorobenzenes, *J. Electron Spectrosc. Relat. Phenom.* **1**, 227–250 (1972).

[157] B. Fornberg and D. M. Sloan, A review of pseudospectral methods for solving partial differential equations, *Acta Numerica* **3**, 203–267 (1994).

[158] B. Fornberg, *A Practical Guide to Pseudospectral Methods* (Cambridge University Press, New York, 1996).

[159] F. Rosca-Pruna and M. J. J. Vrakking, Experimental observation of revival structures in picosecond laser-induced alignment of I_2, *Phys. Rev. Lett.* **87**, 153902 (2001).

[160] H. Stapelfeldt and T. Seideman, Colloquium: Aligning molecules with strong laser pulses, *Rev. Mod. Phys.* **75**, 543–557 (2003).

[161] T. Kanai, S. Minemoto, and H. Sakai, Quantum interference during high-order harmonic generation from aligned molecules, *Nature* **435**, 470–474 (2005).

[162] B. K. McFarland, J. P. Farrell, P. H. Bucksbaum, and M. Gühr, High harmonic generation from multiple orbitals in N_2, *Science* **322**, 1232–1235 (2008).

[163] C. Z. Bisgaard, O. J. Clarkin, G. Wu, A. M. D. Lee, O. Geßner, C. C. Hayden, and A. Stolow, Time-resolved molecular frame dynamics of fixed-in-space CS_2 molecules, *Science* **323**, 1464–1468 (2009).

[164] D. Pavičić, K. F. Lee, D. M. Rayner, P. B. Corkum, and D. M. Villeneuve, Direct measurement of the angular dependence of ionization for N_2, O_2, and CO_2 in intense laser fields, *Phys. Rev. Lett.* **98**, 243001 (2007).

[165] I. Thomann, R. Lock, V. Sharma, E. Gagnon, S. T. Pratt, H. C. Kapteyn, M. M. Murnane, and W. Li, Direct measurement of the angular dependence of the single-photon ionization of aligned N_2 and CO_2, *J. Phys. Chem. A* **112**, 9382–9386 (2008).

[166] R. de Nalda, E. Heesel, M. Lein, N. Hay, R. Velotta, E. Springate, M. Castillejo, and J. P. Marangos, Role of orbital symmetry in high-order harmonic generation from aligned molecules, *Phys. Rev. A* **69**, 031804(R) (2004).

[167] V. Kumarappan, L. Holmegaard, C. Martiny, C. B. Madsen, T. K. Kjeldsen, S. S. Viftrup, L. B. Madsen, and H. Stapelfeldt, Multiphoton electron angular distributions from laser-aligned CS_2 molecules, *Phys. Rev. Lett.* **100**, 093006 (2008).

[168] X. M. Tong, Z. X. Zhao, and C. D. Lin, Theory of molecular tunneling ionization, *Phys. Rev. A* **66**, 033402 (2002).

[169] J. Muth-Böhm, A. Becker, and F. H. M. Faisal, Suppressed molecular ionization for a class of diatomics in intense femtosecond laser fields, *Phys. Rev. Lett.* **85**, 2280–2283 (2000).

[170] M. J. DeWitt, E. Wells, and R. R. Jones, Ratiometric comparison of intense field ionization of atoms and diatomic molecules, *Phys. Rev. Lett.* **87**, 153001 (2001).

[171] E. Wells, M. J. DeWitt, and R. R. Jones, Comparison of intense-field ionization of diatomic molecules and rare-gas atoms, *Phys. Rev. A* **66**, 013409 (2002).

[172] W. Li, X. Zhou, R. Lock, S. Patchkovskii, A. Stolow, H. C. Kapteyn, and M. M. Murnane, Time-resolved dynamics in N_2O_4 probed using high harmonic generation, *Science* **322**, 1207–1211 (2008).

[173] O. Smirnova, Y. Mairesse, S. Patchkovskii, N. Dudovich, D. Villeneuve, P. Corkum, and M. Y. Ivanov, High harmonic interferometry of multi-electron dynamics in molecules, *Nature* **460**, 972–977 (2009). doi: 10.1038/nature08253.

[174] X. M. Tong and S. I. Chu, Time-dependent density-functional theory for strong-field multiphoton processes: Application to the study of the role of dynamical electron correlation in multiple high-order harmonic generation, *Phys. Rev. A* **57**, 452–461 (1998).

[175] X. Chu and S. I. Chu, Role of the electronic structure and multielectron responses in ionization mechanisms of diatomic molecules in intense short-pulse lasers: An all-electron *ab initio* study, *Phys. Rev. A* **70**, 061402(R) (2004).

[176] J. Heslar, J. J. Carrera, D. A. Telnov, and S. I. Chu, High-order harmonic generation of heteronuclear diatomic molecules in intense ultrashort laser fields: An all-electron TDDFT study, *Int. J. Quant. Chem.* **107**, 3159–3168 (2007).

[177] L. S. Blackford, J. Demmel, J. Dongarra, I. Duff, S. Hammarling, G. Henry, M. Heroux, L. Kaufman, A. Lumsdaine, A. Petitet, et al., An updated set of basic linear algebra subprograms (BLAS), *ACM Trans. Math. Software* **28**, 135–151 (2002).

[178] M. R. Hermann and J. A. Fleck, Jr., Split-operator spectral method for solving the time-dependent Schrödinger equation in spherical coordinates, *Phys. Rev. A* **38**, 6000–6012 (1988).

[179] M. D. Feit, J. A. Fleck, Jr., and A. Steiger, Solution of the Schrödinger equation by a spectral method, *J. Comput. Phys.* **47**, 412–433 (1982).

[180] E. Runge and E. K. U. Gross, Density-functional theory for time-dependent systems, *Phys. Rev. Lett.* **52**, 997–1000 (1984).

[181] L. D. Landau and E. M. Lifshitz, *The Classical Theory of Fields* (Pergamon Press, Oxford; New York, 1975).

[182] B. M. Bode and M. S. Gordon, Macmolplt: a graphical user interface for GAMESS, *J. Mol. Graphics Mod.* **16**, 133–138 (1998), URL http://www.scl.ameslab.gov/MacMolPlt/.

[183] G. L. Kamta and A. D. Bandrauk, Imaging electron molecular orbitals via ionization by intense femtosecond pulses, *Phys. Rev. A* **74**, 033415 (2006).

[184] D. A. Telnov and S. I. Chu, Effects of multiple electronic shells on strong-field multiphoton ionization and high-order harmonic generation of diatomic molecules with arbitrary orientation: An all-electron time-dependent density-functional approach, *Phys. Rev. A* **80**, 043412 (2009).

[185] I. N. Levine, *Quantum Chemistry* (Prentice-Hall, Inc., Englewood Cliffs, New Jersey, 1991), 4th ed.

[186] A.-T. Le, X.-M. Tong, and C. D. Lin, Alignment dependence of high-order harmonic generation from CO_2, *J. Mod. Opt.* **54**, 967–980 (2007).

[187] V.-H. Le, N.-T. Nguyen, C. Jin, A.-T. Le, and C. D. Lin, Retrieval of interatomic separations of molecules from laser-induced high-order harmonic spectra, *J. Phys. B: At. Mol. Opt. Phys.* **41**, 085603 (2008).

[188] M. Abu-samha and L. B. Madsen, Theory of strong-field ionization of aligned CO_2, *Phys. Rev. A* **80**, 023401 (2009).

[189] A. S. Alnaser, C. M. Maharjan, X. M. Tong, B. Ulrich, P. Ranitovic, B. Shan, Z. Chang, C. D. Lin, C. L. Cocke, and I. V. Litvinyuk, Effects of orbital symmetries in dissociative ionization of molecules by few-cycle laser pulses, *Phys. Rev. A* **71**, 031403(R) (2005).

[190] A. Jaroń-Becker, A. Becker, and F. H. M. Faisal, Dependence of strong-field photoelectron angular distributions on molecular orientation, *J. Phys. B: At. Mol. Opt. Phys.* **36**, L375–L380 (2003).

[191] P. B. Corkum, Plasma perspective on strong field multiphoton ionization, *Phys. Rev. Lett.* **71**, 1994–1997 (1993).

[192] J. L. Krause, K. J. Schafer, and K. C. Kulander, High-order harmonic generation from atoms and ions in the high intensity regime, *Phys. Rev. Lett.* **68**, 3535–3538 (1992).

[193] M. Lewenstein, P. Balcou, M. Y. Ivanov, A. L'Huillier, and P. B. Corkum, Theory of high-harmonic generation by low-frequency laser fields, *Phys. Rev. A* **49**, 2117–2132 (1994).

[194] M. Lein, N. Hay, R. Velotta, J. P. Marangos, and P. L. Knight, Interference effects in high-order harmonic generation with molecules, *Phys. Rev. A* **66**, 023805 (2002).

[195] M. Lein, P. P. Corso, J. P. Marangos, and P. L. Knight, Orientation dependence of high-order harmonic generation in molecules, *Phys. Rev. A* **67**, 023819 (2003).

[196] C. Vozzi, F. Calegari, E. Benedetti, J.-P. Caumes, G. Sansone, S. Stagira, M. Nisoli, R. Torres, E. Heesel, N. Kajumba, et al., Controlling two-center interference in molecular high harmonic generation, *Phys. Rev. Lett.* **95**, 153902 (2005).

[197] W. Boutu, S. Haessler, H. Merdji, P. Breger, G. Waters, M. Stankiewicz, L. J. Frasinski, R. Taieb, J. Caillat, A. Maquet, et al., Coherent control of attosecond emission from aligned molecules, *Nature Phys.* **4**, 545–549 (2008).

[198] T. Udem, R. Holzwarth, and T. W. Hänsch, Optical frequency metrology, *Nature* **416**, 233–237 (2002).

[199] S. T. Cundiff and J. Ye, Colloquium: Femtosecond optical frequency combs, *Rev. Mod. Phys.* **75**, 325–342 (2003).

[200] D. J. Jones, S. A. Diddams, J. K. Ranka, A. Stentz, R. S. Windeler, J. L. Hall, and S. T. Cundiff, Carrier-envelope phase control of femtosecond mode-locked lasers and direct optical frequency synthesis, *Science* **288**, 635–639 (2000).

[201] S. T. Cundiff, J. Ye, and J. L. Hall, Optical frequency synthesis based on mode-locked lasers, *Rev. Sci. Instrum.* **72**, 3749–3771 (2001).

[202] T. R. Schibli, I. Hartl, D. C. Yost, M. J. Martin, A. Marcinkevičius, M. E. Fermann, and J. Ye, Optical frequency comb with submillihertz linewidth and more than 10 W average power, *Nature Photon.* **2**, 355–359 (2008).

[203] M. Fischer, N. Kolachevsky, M. Zimmermann, R. Holzwarth, T. Udem, T. W. Hänsch, M. Abgrall, J. Grünert, I. Maksimovic, S. Bize, et al., New limits on the drift of fundamental constants from laboratory measurements, *Phys. Rev. Lett.* **92**, 230802 (2004).

[204] H. S. Margolis, G. P. Barwood, G. Huang, H. A. Klein, S. N. Lea, K. Szymaniec, and P. Gill, Hertz-level measurement of the optical clock frequency in a single $^{88}Sr^{+}$ ion, *Science* **306**, 1355–1358 (2004).

[205] S. Witte, R. T. Zinkstok, W. Ubachs, W. Hogervorst, and K. S. E. Eikema, Deep-ultraviolet quantum interference metrology with ultrashort laser pulses, *Science* **307**, 400–403 (2005).

[206] P. Del'Haye, A. Schliesser, O. Arcizet, T. Wilken, R. Holzwarth, and T. J. Kippenberg, Optical frequency comb generation from a monolithic microresonator, *Nature* **450**, 1214–1217 (2007).

[207] S. A. Diddams, T. Udem, J. C. Bergquist, E. A. Curtis, R. E. Drullinger, L. Hollberg, W. M. Itano, W. D. Lee, C. W. Oates, K. R. Vogel, et al., An optical clock based on a single trapped $^{199}Hg^{+}$ ion, *Science* **293**, 825–828 (2001).

[208] M. Takamoto, F.-L. Hong, R. Higashi, and H. Katori, An optical lattice clock, *Nature* **435**, 321–324 (2005).

[209] M. J. Thorpe, K. D. Moll, R. J. Jones, B. Safdi, and J. Ye, Broadband cavity ringdown spectroscopy for sensitive and rapid molecular detection, *Science* **311**, 1595–1599 (2006).

[210] S. A. Diddams, L. Hollberg, and V. Mbele, Molecular fingerprinting with the resolved modes of a femtosecond laser frequency comb, *Nature* **445**, 627–630 (2007).

[211] C. Gohle, T. Udem, M. Herrmann, J. Rauschenberger, R. Holzwarth, H. A. Schuessler, F. Krausz, and T. W. Hänsch, A frequency comb in the extreme ultraviolet, *Nature* **436**, 234–237 (2005).

[212] R. J. Jones, K. D. Moll, M. J. Thorpe, and J. Ye, Phase-coherent frequency combs in the vacuum ultraviolet via high-harmonic generation inside a femtosecond enhancement cavity, *Phys. Rev. Lett.* **94**, 193201 (2005).

[213] D. C. Yost, T. R. Schibli, and J. Ye, Efficient output coupling of intracavity high-harmonic generation, *Opt. Lett.* **33**, 1099–1101 (2008).

[214] A. Ozawa, J. Rauschenberger, C. Gohle, M. Herrmann, D. R. Walker, V. Pervak, A. Fernandez, R. Graf, A. Apolonski, R. Holzwarth, et al., High harmonic frequency combs for high resolution spectroscopy, *Phys. Rev. Lett.* **100**, 253901 (2008).

[215] D. C. Yost, T. R. Schibli, J. Ye, J. L. Tate, J. Hostetter, M. B. Gaarde, and K. J. Schafer, Vacuum-ultraviolet frequency combs from below-threshold harmonics, *Nature Phys.* **5**, 815–820 (2009).

[216] J. J. Carrera and S. I. Chu, *Ab initio* time-dependent density-functional-theory study of the frequency comb structure, coherence, and dephasing of multielectron systems in the vuv-xuv regimes via high-order harmonic generation, *Phys. Rev. A* **79**, 063410 (2009).

[217] T. S. Ho, S. I. Chu, and J. V. Tietz, Semiclassical many-mode Floquet theory, *Chem. Phys. Lett.* **96**, 464–471 (1983).

[218] T. S. Ho and S. I. Chu, Semiclassical many-mode Floquet theory. II. Nonlinear multiphoton dynamics of a 2-level system in a strong bichromatic field, *J. Phys. B: At. Mol. Phys.* **17**, 2101–2128 (1984).

[219] T. S. Ho and S. I. Chu, Semiclassical many-mode Floquet theory. III. SU(3) dynamical evolution of three-level systems in intense bichromatic fields, *Phys. Rev. A* **31**, 659–676 (1985).

[220] T. S. Ho and S. I. Chu, Semiclassical many-mode Floquet theory. IV. Coherent population trapping and SU(3) dynamical evolution of dissipative three-level systems in intense bichromatic fields, *Phys. Rev. A* **32**, 377–395 (1985).

[221] J. H. Shirley, Solution of the Schrödinger equation with a Hamiltonian periodic in time, *Phys. Rev.* **138**, B979–B987 (1965).

[222] J. R. Friedman, V. Patel, W. Chen, S. K. Tolpygo, and J. E. Lukens, Quantum superposition of distinct macroscopic states, *Nature* **406**, 43–46 (2000).

[223] D. Vion, A. Aassime, A. Cottet, P. Joyez, H. Pothier, C. Urbina, D. Esteve, and M. H. Devoret, Manipulating the quantum state of an electrical circuit, *Science* **296**, 886–889 (2002).

[224] Y. Yu, S. Han, X. Chu, S. I. Chu, and Z. Wang, Coherent temporal oscillations of macroscopic quantum states in a Josephson junction, *Science* **296**, 889–892 (2002).

[225] I. Chiorescu, Y. Nakamura, C. J. P. M. Harmans, and J. E. Mooij, Coherent quantum dynamics of a superconducting flux qubit, *Science* **299**, 1869–1871 (2003).

[226] W. D. Oliver, Y. Yu, J. C. Lee, K. K. Berggren, L. S. Levitov, and T. P. Orlando, Mach-Zehnder interferometry in a strongly driven superconducting qubit, *Science* **310**, 1653–1657 (2005).

[227] D. M. Berns, W. D. Oliver, S. O. Valenzuela, A. V. Shytov, K. K. Berggren, L. S. Levitov, and T. P. Orlando, Coherent quasiclassical dynamics of a persistent current qubit, *Phys. Rev. Lett.* **97**, 150502 (2006).

[228] P. K. Aravind and J. O. Hirschfelder, Two-state systems in semiclassical and quantized fields, *J. Chem. Phys.* **88**, 4788–4801 (1984).

[229] Y. Nakamura, Y. A. Pashkin, and J. S. Tsai, Rabi oscillations in a Josephson-junction charge two-level system, *Phys. Rev. Lett.* **87**, 246601 (2001).

[230] J. H. Van Vleck, On σ-type doubling and electron spin in the spectra of diatomic molecules, *Phys. Rev.* **33**, 467–506 (1929).

[231] P. R. Certain and J. O. Hirschfelder, New partitioning perturbation theory. I. General formalism, *J. Chem. Phys.* **52**, 5977–5987 (1970).

[232] J. O. Hirschfelder, Almost degenerate perturbation theory, *Chem. Phys. Lett.* **54**, 1–3 (1978).

[233] S. Ashhab, J. R. Johansson, A. M. Zagoskin, and F. Nori, Two-level systems driven by large-amplitude fields, *Phys. Rev. A* **75**, 063414 (2007).

[234] Y. S. Greenberg, Low-frequency Rabi spectroscopy of dissipative two-level systems: Dressed-state approach, *Phys. Rev. B* **76**, 104520 (2007).

[235] C. M. Wilson, T. Duty, F. Persson, M. Sandberg, G. Johansson, and P. Delsing, Coherence times of dressed states of a superconducting qubit under extreme driving, *Phys. Rev. Lett.* **98**, 257003 (2007).

[236] S. Han, J. Lapointe, and J. E. Lukens, Thermal activation in a two-dimensional potential, *Phys. Rev. Lett.* **63**, 1712–1715 (1989).

[237] A. J. Leggett, S. Chakravarty, A. T. Dorsey, M. P. A. Fisher, A. Garg, and W. Zwerger, Dynamics of the dissipative two-state system, *Rev. Mod. Phys.* **59**, 1–85 (1987).

[238] X. Chu and S. I. Chu, Complex-scaling generalized pseudospectral method for quasienergy resonance states in two-center systems: Application to the Floquet study of charge resonance enhanced multiphoton ionization of molecular ions in intense low-frequency laser fields, *Phys. Rev. A* **63**, 013414 (2001).

[239] D. A. Telnov and S. I. Chu, *Ab initio* study of high-order harmonic generation of H_2^+ in intense laser fields: Time-dependent non-Hermitian Floquet approach, *Phys. Rev. A* **71**, 013408 (2005).

[240] T.-S. Ho, S.-H. Hung, H.-T. Chen, and S. I. Chu, Memory effect on the multiphoton coherent destruction of tunneling in the electron transport of nanoscale systems driven by a periodic field: A generalized Floquet approach, *Phys. Rev. B* **79**, 235323 (2009).

[241] G. Floquet, Sur les équations différentielles linéaires à coefficients périodiques, *Ann. Sci. Ec. Norm. Sup.* **12**, 47–88 (1883).

[242] M. Abramowitz and I. A. Stegun, eds., *Handbook of Mathematical Functions* (Dover, New York, 1972), 10th ed.

[243] F. Grossmann, T. Dittrich, P. Jung, and P. Hänggi, Coherent destruction of tunneling, *Phys. Rev. Lett.* **67**, 516–519 (1991).

Index